UNIVERSITÉ DE GENÈVE — FACULTÉ DES SCIENCES

Département de physique nucléaire et corpusculaire

Professeur Allan Clark et
Professeur Alain Blondel

Evaluation of Silicon sensors for the ATLAS Silicon Tracker, and TPC reconstruction in the HARP Experiment

THÈSE

présentée à la Faculté des sciences

de l'Université de Genève

pour l'obtention du grade de Docteur ès sciences,

mention physique

par

Maria Cristina MORONE

d'Italie

Thèse No 3418

GENÈVE

Atelier de reproduction de la Section de Physique

2003

Contents

Résumé

Évaluation de détecteurs en Silicium pour le traqueur de ATLAS

L'expérience ATLAS étudiera des collisions entre protons pour une énergie dans le centre masse de 14 TeV, au collisionneur LHC au CERN. Étant donné que les sections efficaces des processus recherchés sont très petites, le LHC a été conçu pour avoir une luminosité elevée (10^{34} particules/cm^{2}s), avec des croisement des faisceaux toutes les 25 ns. D'autre part, la grande section efficace pour les interactions hadroniques de "*minimum bias*" amène à une moyenne de 10^9 évènements par seconde, dont seulement une petite partie doit être selectionnée et reconstruite.

Le traqueur de ATLAS a été conçu pour accomplir les mesures de leptons de grande impulsion transverse, pour identifier les électrons, les taus et les photons à haute luminosité, et pour la reconstruction complète des évènements dans le premier run à basse luminosité (10^{33} particules/cm^{2}s) du LHC. À la luminosité prévue, environ 1000 particules traverseront le traqueur toutes les 25 ns. Ce flux très elevé exige des détecteurs de traces qui soient rapides et qui aient une grande granularité.

Le traqueur de ATLAS est constitué par trois différents systèmes. Le plus proche de la région d'interaction est un système de détecteurs à "*pixel*"; il est entouré par le traqueur composé de détecteurs à micro-pistes en silicium. Le système le plus à l'extérieur est constitué par des détecteurs de radiation de transition. Tout le traqueur se trouve dans un aimant solenoïdale qui engendre un champ magnétique de 2 T.

Les détecteurs à micro-pistes ont une très bonne résolution spatiale et seront fondamentals pour la reconstruction des traces. Ils contribueront aussi à la mesure de l'impulsion, du paramètre d'impact et des vertex secondaires.

Étants très proches des faisceaux de protons, les détecteurs seront exposés à un énorme taux de radiation qui va en dégrader les caractéristiques intrinsèques et de fonctionnement. De même, leur performance doit rester satisfaisante pendant au moins dix ans de fonctionnement du LHC. Un grand travail de développement, simulation, évaluation des détecteurs a été accompli pendant des années par les physiciens et par les usines productrices. Il a conduit à un schéma de détecteurs qui, même en étant affectés par les radiations, assureront une performance satisfaisante en terme de résolution spatiale et de rapport entre signal et bruit grâce à des choix appropriés de matériels et charactéristiques intrinsèques. Pour cela, la collaboration SCT a défini des spécifications techniques que les détecteur doivent satisfaire pour être utilisés dans ATLAS.

La première partie de ce travail de thèse a été consacrée à l'étude de détecteurs à micro-pistes produits par l'usine suisse CSEM pour en évaluer les performances avant et après l'irradiation sur la base des spécifications. Les mesures faites ont constitué la base pour l'éventuelle qualification de CSEM pour produire les détecteurs au silicium pour l'expérience ATLAS.

Les détecteurs à micro-pistes d'ATLAS ont des diodes de type p implantées dans une sous-couche de type n avec un contact n^+. Leur épaisseur est de $300\,\mu$m et les dimensions sont d'environ 6 cm par 6 cm. Ces dernières sont legèrement variables en raison de leur position dans le traqueur. Chaque détecteur a 768 micropistes, dont chacune est lue. Les micropistes sont alimentées à travers des resistances en poly-silicium, distentes de 80μm, pour atteindre une résolution spatiale d'environ $20\,\mu$m. Les détecteurs sont arrangés en modules dans lequels quatre détecteurs trouvent place, deux par côté, ensemble avec l'électronique d'acquisition. Les détecteurs des deux

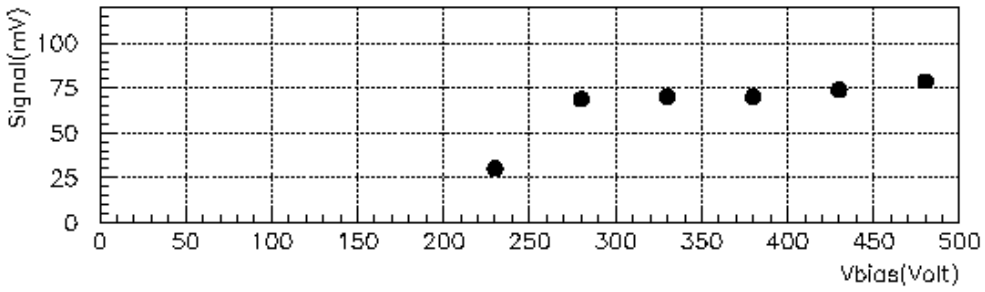

Figure 1: Signal collecté en fonction de la tension d'alimentation avec un prototype de détecteur à micro-piste en silicium irradié.

faces ont un petit angle stéreo entre eux, permettant de mesurer la coordonnée z.
Les caractéristiques intrinsèques et de fonctionnement faisant l'objet des spécifications ont été mesurées au cours de ce travail de thèse sur différents prototypes de détecteurs à micropistes produits par l'usine CSEM et ont été comparées avec le même ensemble de mesure effectué sur des détecteurs irradiés pour simuler la dose qu'il recevront pendant dix ans d'opération du LHC.

La radiation change le dopage initial en transformant la sous-couche de type n à type p après quelques années de fonctionnement. Elle va aussi créer des niveaux de "trappes" dans le silicium. Ces deux effets exigent une considérable sur-dépletion des détecteurs pour obtenir une collection de la charge adéquate. La sur-dépletion va aussi rendre minime le bruit, à travers la minimisation de la capacité inter-pistes qui augmente à cause des charges qui vont s'accumuler dans la couche d' oxyde entre les pistes. Les mesure effectuées pour cette thèse montrent qu' il est necessaire d'alimenter les détecteurs irradiés avec environ 350 V pour que la collection de charge soit complète, comme montré dans la figure 1.
La radiation, en créant des niveaux énergétiques au milieu de la bande de "*gap*", est aussi responsable de la forte augmentation (deux ordres de grandeur environ) du courant de fuite. La figure 2 montre le courant mesuré en fonction de la ten-

sion d'alimentation avant et après l'irradiation d'un détecteur . Les micro-pistes sont

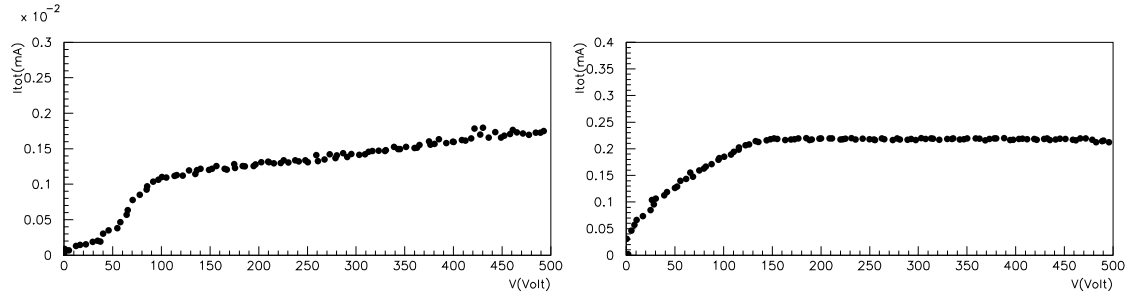

Figure 2: Caractéristique tension-courant pour le même détecteur avant et après irradiation. Les mesures ont été faites aux température de 20°C et de -18°C, respectivement. On observe une difference de courant de deux ordres de grandeur.

couplées capacitivement pour proteger l'électronique d'acquisition par ce courant. Le courant de fuite depends fortemment de la temperature.

Les dommages dus aux radiations ne sont pas tous stables et, soit la tension de dépletion, soit le courant montrent un "*annealing*". La tension de dépletion a deux périodes differentes d'*annealing*, dont la première, à court terme, est bénéfique et comporte une diminution exponentielle de la tension de dépletion, tandis que la deuxième amène à une nouvelle augmentation. Cette augmentation, peut être relentie en gardant les détecteurs à très basse temperature. Dans le LHC ils fonctionneront à $-7°$, mais des périodes de rechauffement dues à l'entretien du détecteur seront inévitables. Ils est prévu d'avoir deux jour à 20° et deux semaines à 17° chaque année.

L'effet de ces périodes "chaudes" est étudié pour comprendre leurs implications sur le fonctionnement des détecteurs . Ce genre d'étude est fait sur une courte période en irradiant les détecteurs et en simulant l'effet du réchauffement en utilisant des modèles pour l'endommagement dû à la radiation. Il a été calculé que la quantité d'*annealing* que les détecteurs recevront pendant 10 ans de LHC est équivalente à une période d'*annealing* plus bref, mais à plus haute temperature, par exemple pour 21 jours à 25°.

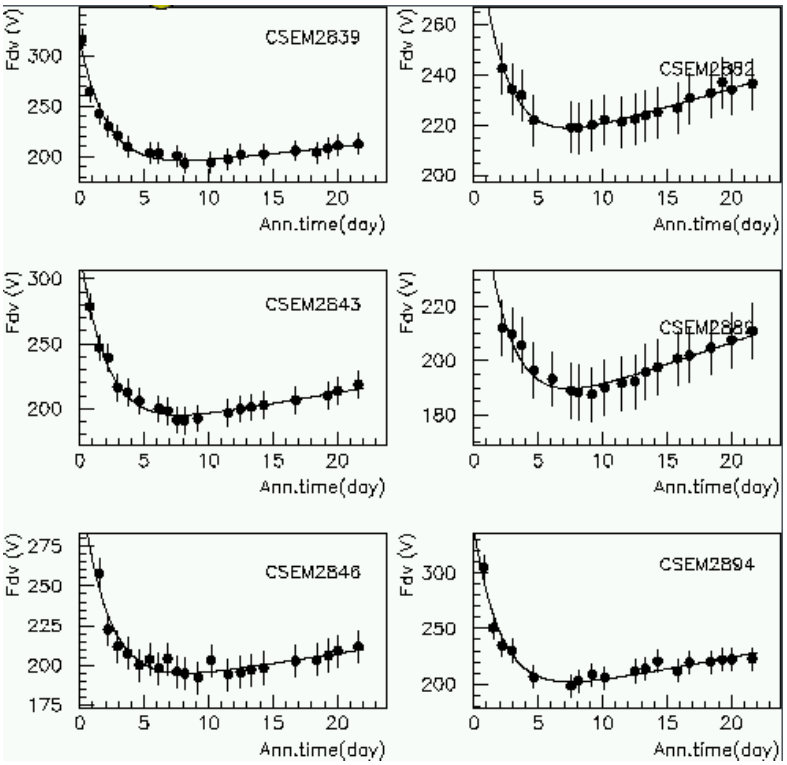

Figure 3: Tension de dépletion en fonction du temps d'*annealing* à 25°C. Les deux differentes périodes (bénéfique et inverse) sont bien visibles.

Differents cycles d'"*annealing*" ont été suivis sur beaucoup de prototypes fabriqués par CSEM; la figure 3 montre par exemple l'"*annealing*" de la tension de dépletion de quelques détecteurs irradiés.

Les paramètres de fonctionnement établis par les spécifications ont été mesurés après l'*annealing*. Les résultats de ces mesures, avec les équivalents obtenus avant l'irradiation, ont été la base pour évaluer la performance des détecteurs fabriqués par l'usine suisse. Cette performance n'a pas été jugée acceptable par la collaboration SCT, qui a choisi d'autres usines pour la fabrication de détecteurs à micro-pistes qui seront utilisés dans ATLAS. Une comparaison entre les performances des differents prototypes est exposée dans la dernière section de la première partie de cette thèse.

Reconstruction des traces de la TPC dans l'expérience HARP

Le but de l'expérience HARP est de produire l'information nécessaire pour maximiser la section efficace de production de pions, en étudiant différentes cibles et projectiles d'impulsions variant entre 1.5 et 15 GeV/c. La précision demandée sur les sections efficaces est de quelques pour cents.

Cette mesure est importante, soit pour la détermination soignée de la production de particules secondaires avec les rayons cosmiques primaires, soit pour la production de pions dans les Usines à Neutrinos qui sont en projet. Ces deux informations permettront de comprendre davantage les oscillations des neutrinos atmosphériques et de procéder à des études systématiques de la matrice de mélange des leptons.

L'expérience utilise le faisceau de l'accélérateur PS au CERN. Le détecteur couvre tout l'angle solide et est construit de façon à avoir le plus de redondance possible pour une précision de mesure élevée.

Le système comprends des détecteurs de faisceau (temps de vol, compteurs Cherenkov, chambres à fils) pour identifier les particules qui vont atteindre la cible et pouvoir estimer leur flux. La cible se trouve dans une "Chambre à Projection Temporelle" (TPC), entourée par des "Chambres à Plaques Résistives" (RPC) et par un aimant qui engendre un champ magnétique aligné avec le faisceau. Le système constitué par la TPC et les RPC permet l'identification des particules dans la région "à grand angle": l'impulsion est mesurée par la courbure des traces dans la TPC, tandis que la mesure de vitesse est accomplie grâce à celle du temps de vol avec les RPCs.

Le spectromètre continue vers l'avant avec des chambres à fils situées avant et après un aimant dipolaire. Ces chambres permettent de reconstruire les traces des particules et d'en mesurer l'impulsion. Le compteur Cherenkov à seuil qui suit, distingue les protons des pions à partir d'une impulsion de 3 GeV/c tandis que pour des impulsions au dessous de 3.5 GeV/c cette distinction est accomplie par la mesure du

temps de vol sur une distance de dix mètres environ entre une paroi de scintillateurs ("TOF wall") et un des Cherenkov de faisceau. En plus, les calorimètres permettent d'identifier les hadrons, les électrons, les photons et les muons.

Le système de déclanchement utilise soit des scintillateurs entourants la cible, pour sélectionner des intéractions à grand angle, soit une paroi de scintillateurs située après la TPC pour les intéractions à l'avant. L'information qui provient de ces deux détecteurs est complétée par les détecteurs se trouvant le long du faisceau qui permettent de sélectionner les particules ayant une trajectoire leur permettant d'atteindre la cible.

HARP a été construite dans un très court délai et a pris des données pendant deux années, en 2001 et en 2002. Pendant la prise de données, les logiciels de reconstruction ont été en grand partie dévéloppés, mais il restent encore a perfectionner, et la calibration des détecteurs a commencé. En particulier, un problème de "*cross talk* entre les pads de la TPC a été mis en évidence. Cet effet, qui implique une résolution spatiale (environ 2 mm dans la direction $r - \phi$ et 3 mm en z) très mauvaise par rapport à celle de projet, est à present étudié et sera corrigé par *software* dans le futur.

La deuxième partie de ce travail de thèse concerne le développement du logiciel de "fit" des traces dans la TPC et de reconstruction de la charge et de l'impulsion des particules. Ce logiciel est le dernier de toute une série qui sert à convertir les données brutes dans un format permettant d'en extraire l'information physique.

Les particules chargées ont des trajectoires hélicoidales dans la TPC. Le fit doit déterminer les cinq paramètres décrivant l'hélice qui s'adapte le mieux aux données. Cela est accompli en deux étapes: dans la première, en déterminant les paramètres géométriques relatifs à la projection de l'hélice dans le plan orthogonal au faisceau, et dans la deuxième en déterminant l'angle de la trace par rapport au faisceau et son point d'impact. Après avoir determiné les paramètres géométriques de la trace, la charge de la particule est reconstruite en utilisant la connaissance du sens de rotation

dans le champ magnétique, ainsi que l'impulsion transverse, liée à l' estimation de la flêche, et l'impulsion longitudinale, liée à l'angle entre la trace et le faisceau.

L'efficacité du fit a été évaluée en utilisant des échantillons de données Monte Carlo reproduisantes des événements avec un seul muon, d'impulsion fixe. Des traces parfaites, et avec 2 mm de décalage dans l'espace tridimensionnel (reproduisants la résolution qu'on mesure à présent), ont été utilisées. Avec les traces parfaites la charge est correctement reconstruite pour la totalité des événements et l'impulsion est reconstruite à moins d'effets dus à la perte d'énergie par ionisation et à la diffusion multiple, qui ne sont pas pris en compte dans le logiciel.

Pour les traces avec les points distribués avec 2 mm de largeur par rapport à leur position sur l'hélice, la résolution sur la coordonnée radiale du point d'impact est de 2.3 mm tandis que celle sur la coordonnée z est de 3.2 mm. La charge est correctement reconstruite au niveau du per mille. L'impulsion transverse est reconstruite avec une résolution de 20% à 500 MeV/c. (L'inefficacité de la TPC n'est pas prise en compte).

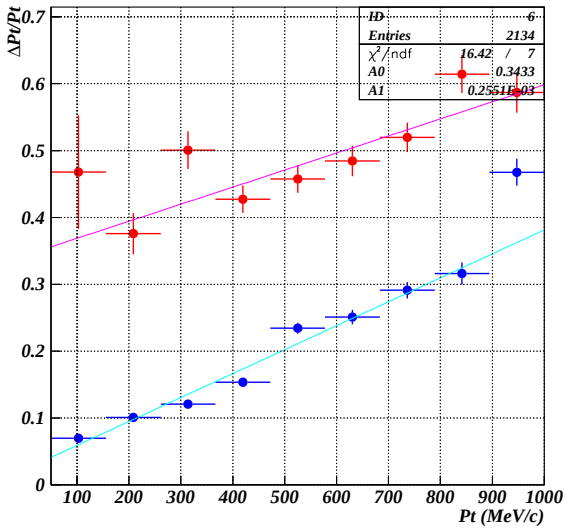

Figure 4: Résolution en impulsion transverse pour des événements Monte Carlo avec 2 mm de dispersion des points (en bleu) et pour des cosmiques (en rouge).

L'efficacité de toute la chaîne de reconstruction des traces de la TPC peut aussi être évaluée avec les rayons cosmiques: les trajectoires des muons sont en fait coupées en deux branches par le logiciel de recherche des traces. Ces deux branches, en appartenant à la même particule, doivent être reconstruites avec des paramètres géométriques corrélés et doivent donner la même impulsion. L'analyse des données amène à des résultats compatibles avec une résolution sur l'impulsion d'environ 45% à 500 MeV/c. Ce résultat va s'améliorer avec une calibration du détecteur plus efficace que celle disponible à présent et une fois que le problème du *cross-talk* sera corrigé.
La figure 4 montre le $\Delta p_t/p_t$ en fonction de p_t pour les traces simulées et pour les cosmiques.

Une analyse préliminaire des données concernants deux cibles différentes, en Tantalium et en Aluminium, à des impulsions de faisceau de 3 GeV/c et 12.9 GeV/c respectivement, a été accomplie en considérant la zone à "grand angle" de HARP, c'est à dire la zone qui n'est couverte que par la TPC et les RPC.

Les données relatives aux Tantalium, analysées avec une ancienne version des logiciels de reconstruction, montrent un problème de reconstruction de la charge pour une fraction considérable d'événements. En effectuant une coupure sur les données affectées on obtient des distributions d'impulsions transverses et longitudinales qui sont raisonnablement en accord avec les limites imposées par la cinématique. Le nombre de particules positives produites dans les interactions est environ six fois plus grand que celui des négatives, en intégrant sur tous les impulsions.

Les données relatives à la cible d'aluminium ont été analysées avec une version plus récente et améliorée de la reconstruction. On voit que le problème dans la reconstruction de la charge ne concerne qu'un petit nombre d'événements. En sélectionnant des traces de la TPC qui continuent dans les RPC, on reconstruit bien les dimensions des cibles (elles ont un diamètre de 30 mm tandis que leurs dimensions en z sont de 8 mm et de 395 mm), comme montré dans la figure 5.

Les distributions d'impulsions transverses et longitudinales sont bien en accord avec

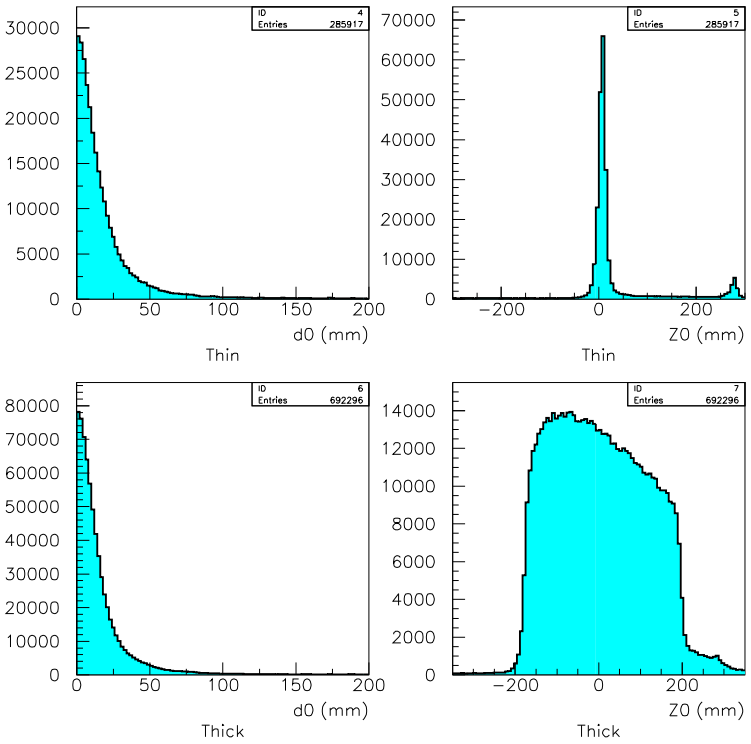

Figure 5: Valeur absolue du paramètre d'impact et coordonnée z du point d'impact pour des collisions entre des protons d'impulsion de 12.9 GeV/c et des cibles d'aluminium.

les limites cinématiques qui imposent $p_t < 2\,\mathrm{GeV/c}$ et $-0.5 < p_z < 4.5\,\mathrm{GeV/c}$ et sont montrées dans la figure 6.

Le rapport entre le nombre de particules positives et négatives vaut cette fois 2.7. À présent l'identification des particules par temps de vol et par dE/dx n'est pas encore possible et l'analyse des données ne peut pas aller plus loin.

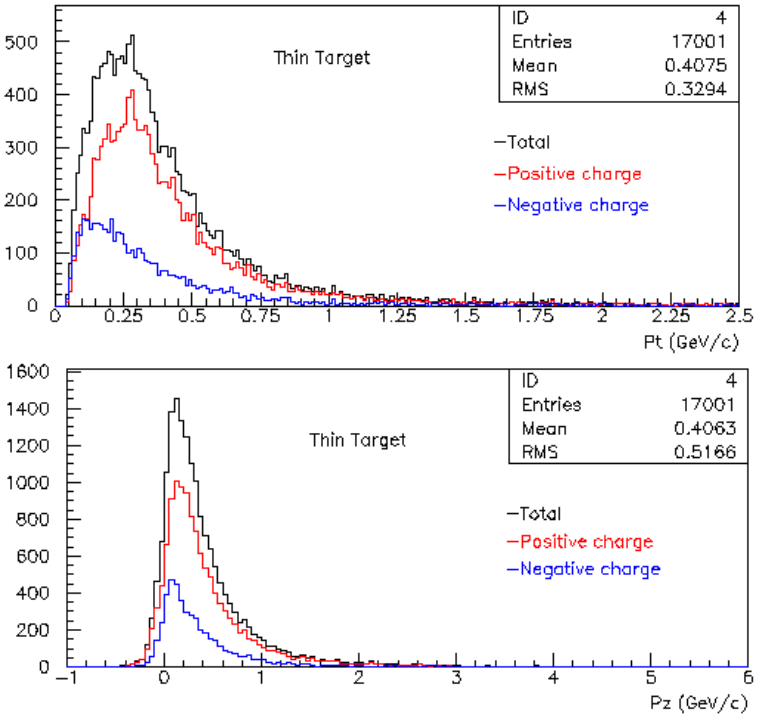

Figure 6: Distributions d'impulsion transverse (en haut) et longitudinale (en bas) obtenues dans les collisions de protons de 12.9 GeV/c avec une cible d'aluminium.

Part I

Evaluation of Silicon sensors for the ATLAS Silicon Tracker

Chapter 1

The Atlas detector at LHC

1.1 The LHC physics motivation

The main subject of investigation at the Large Hadron Collider is the origin of the electroweak scale, of the fermion masses and of their mixing when coupled to charged weak currents.

The centre of mass energy of the collider of 14 TeV reflects an average parton energy of about 300 GeV appropriate to analyse the electroweak symmetry breaking characterised by the value of about 170 GeV of the Higgs potential at its minimum, on which is founded the mass generation in the Standard model. The search for the elusive Higgs particle actually may lead to the discovery of signals of extensions of the standard model that is commonly believed to offer only an effective description of the mass generation. Within the model itself, the lack of protection against radiative corrections at very high energies, presumably at the Planck scale, of the value of the Higgs mass, the so called hierarchy problem, and the inconsistent behaviour at high energies of the running coupling of the non asymptotically free scalar sector of the theory, the so called triviality problem, strongly suggest the effective character of the Higgs sector.

The quark mixing matrix is strictly related to the Higgs mass generation and the severe tests of its unitarity offer a possible clue to new physics, in particular a pre-

cise determination of the small mixing angles of the third generation quarks with the lighter ones and of the CP violating phase as extracted from B meson decays.

The LHC will also extend the predictions of perturbative QCD at very high energies and lead to novel determinations of the strong coupling constant that will further constraint the coupling unification scheme at energies just below the Planck energy, providing new inputs to Grand Unified Theories.

Actually, QCD physics and in particular jet physics and direct heavy flavour production will be the background of possible signals for new physics and the precision of its predictivity will be crucial for potential discoveries.

The exploration of the TeV Scale will be rewarding in any case: either the Higgs particle will be found, or new physics will emerge according to the triviality bound that fixes the maximum Higgs mass around 0.8 TeV.

Supersymmetry is the best candidate for the new physics at the TeV scale. The main motivations, besides the realisation of a new symmetry in nature, are the resolution of the hierarchy and triviality problems of the Higgs sector and its role in adding new matter fields around 1 TeV that drive the gauge couplings to a common unified value at high energies. The first feature comes from the relation that the symmetry states between bosonic and fermionic degrees of freedom, linking the Higgs self-coupling to the weak gauge coupling and to its asymptotic freedom behaviour at high energies. Supersymmetry also protects the minimum of the Higgs potential and therefore provides a natural solution to the hyrarchy problem by translating it into the one of supersymmetry breaking, a necessary condition for the standard electroweak breaking. The supersymmetry and the e-w breaking scales are therefore intimately correlated and accessible to LHC.

The doubling of the observed matter fields by their supersymmetric partners, provides, as already mentioned, novel matter field contributions around 1 TeV, crucial for couplings running to their unification. The Higgs spectrum predicted by the min-

imal supersymmetric standard model is richer than the one of the standard model, and depending upon the value of tanβ parameter that regulates the ratio of the vacuum expectation values responsible for up and down quark masses, may have distinctive decay modes with respect to the standard model case. A promising insight into the supersymmetric-electroweak breaking phenomenon will be provided by accurate searches of flavour changing neutral currents, highly suppressed in the standard model.

The ATLAS detector has been designed to best exploit the LHC energy and luminosity opportunities for the investigation of the physics issues discussed above by a complementarity and, in some cases, redundancy of particle/signal identifications.

1.2 The ATLAS detector

The broad spectrum of detailed physics studies, and in particular the likelihood to either identify the Higgs particle and/or to access extensions of the Standard Model, led to the design of the ATLAS detector. The basic design criteria included the following [1].

- Very good electro-magnetic calorimetry for electron and photon identification and measurements, complemented by full-coverage hadronic calorimetry for accurate jet and missing transverse energy (E_T^{miss}) measurements. This requirement is of paramount importance for the discovery of a light Higgs boson. If its mass is below 160 GeV, the golden detection channel is indeed H$\rightarrow \gamma\gamma$.

- High-precision muon momentum measurements, with the capability to guarantee accurate measurements at the highest luminosity using the external muon spectrometer alone. If the mass of the Higgs boson exceeds twice the Z mass, the cleanest channel to discover the Higgs boson and measure its mass will be H$\rightarrow ZZ \rightarrow \mu^+\mu^-\mu^+\mu^-$. This justifies the need for outstanding performances of

the muon spectrometer.

- Efficient tracking at high luminosity for high-p_T lepton-momentum measurements, electron and photon identification, τ-lepton and heavy-flavour identification, and full event reconstruction capability at lower luminosity. Many signatures of new physics like heavy sequential leptons or supersymmetry, indeed, imply such high p_T particle. Top-notch tracking is hence crucial for a general purpose detector for the LHC.

- Large acceptance in pseudo-rapidity (η) with almost full azimuthal angle (ϕ) coverage everywhere. The azimuthal angle is measured around the beam axis, whereas pseudo-rapidity relates to the polar angle (θ) where θ is the angle from the z direction. Supersymmetry, if exist, is expected to manifest itself through events with large missing energy. Therefore hermeticity is a basic requirement in the search for new physics at LHC.

- Triggering and measurements of particles at low-p_T thresholds, providing high efficiencies for most physics processes of interest at LHC.

The overall detector layout is shown in figure 1.1.

The magnet configuration is based on an inner thin superconducting solenoid surrounding the inner detector cavity, and large superconducting air-core toroids consisting of independent coils arranged with an eight-fold symmetry outside the calorimeters.

The Inner Detector is contained within a cylinder of length 7 m and a radius of 1.15 m, in a solenoidal magnetic field of 2 T. Pattern recognition, momentum and vertex measurements, and electron identification are achieved with a combination of discrete high-resolution semiconductor pixel and strip detectors in the inner part of the tracking volume, and continuous straw-tube tracking detectors with transition radiation capability in its outer part.

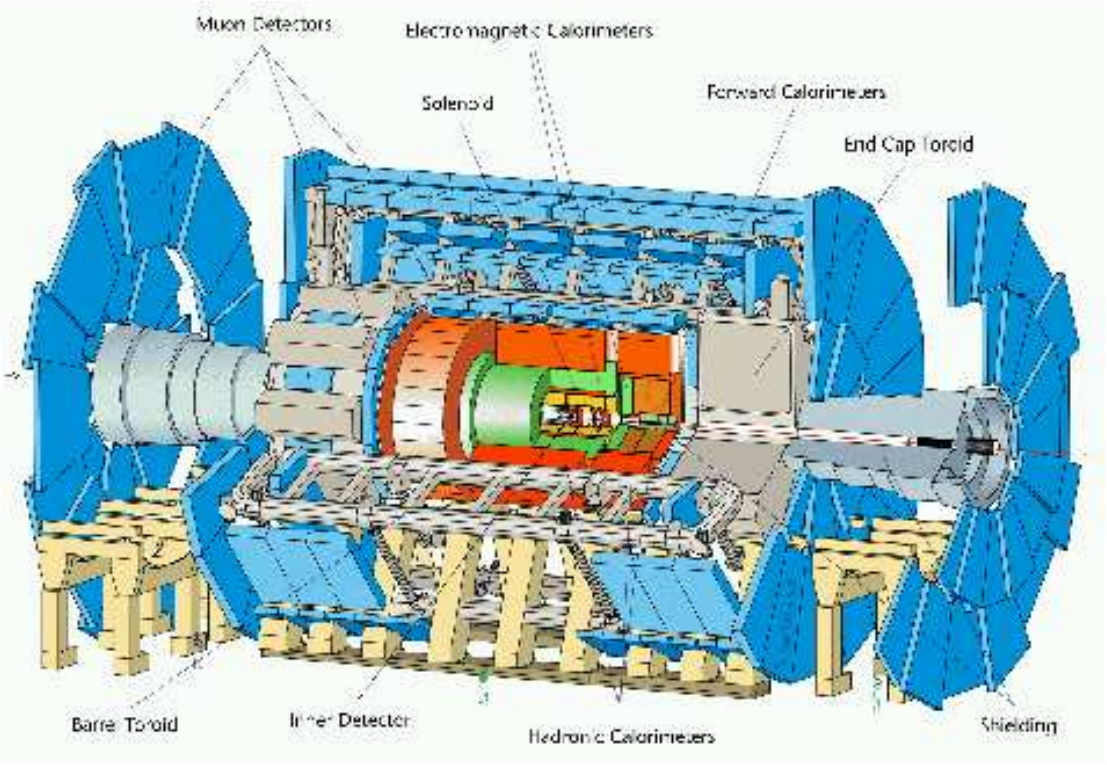

Figure 1.1: Overall layout of the ATLAS detector.

The calorimeter, designed to be capable of reconstructing the energy of electrons, photons and jets, as well as measuring missing transverse energy, consists of an electromagnetic calorimeter, a hadronic barrel calorimeter, hadronic end-cap calorimeters and forward calorimeters.

The barrel electro-magnetic calorimeter is contained in a barrel cryostat, which surrounds the Inner Detector cavity. Two end-cap cryostats house the end-cap electromagnetic and hadronic calorimeters, as well as the integrated forward calorimeter. The barrel and extended barrel tile calorimeters support the Liquid Argon cryostats and also act as the main solenoid flux return.

The electro-magnetic calorimeter is a lead/liquid-argon detector with accordion geometry and it is preceded by a presampler detector, installed immediately behind the

cryostat cold wall, and used to correct for the energy lost in the material (Inner Detector, cryostats, coil) upstream of the calorimeter. The hadronic barrel calorimeter is a cylinder divided into three sections: the central barrel and two identical extended barrels. It is based on a sampling technique with plastic scintillator plates (tiles) embedded in an iron absorber. At larger pseudorapidities, where higher radiation resistance is needed, the intrinsically radiation-hard LAr technology is used for all the calorimeters: the hadronic end-cap calorimeter, a copper LAr detector with parallel-plate geometry, and the forward calorimeter, a dense Liquid Argon calorimeter with rod-shaped electrodes in a tungsten matrix.

The calorimeter is surrounded by the muon spectrometer. The air-core toroid system, with a long barrel and two inserted end-cap magnets, generates a large magnetic field volume with strong bending power within a light and open structure. Multiple-scattering effects are thereby minimised, and the necessary muon momentum resolution is achieved with three stations of tracking chambers. The muon instrumentation also includes the trigger chambers with very fast time response.

The muon spectrometer defines the overall dimensions of the ATLAS detector. The outer chambers of the barrel are at a radius of about 11 m. The half-length of the barrel toroid coils is 12.5 m, and the third layer of the forward muon chambers, mounted on the cavern wall, is located about 23 m from the interaction point. The overall weight of the ATLAS detector is about 7000 Tons.

The general detector performance goals are summarised in table 1.1.

1.3 The ATLAS inner detector

As the main subject of this thesis work is the study of the Silicon Microstrip sensors, used in the ATLAS Inner Detector, in the following will be given a more detailed description of this system, and in particular of the Semiconductor Tracker.

The layout of the Inner Detector is shown in figure 1.2.

Detector component	Minimally required resol.,characteristics	η coverage Measurem.	η coverage Trigger	Physics examples
e.m. calorimetry	$10\%/\sqrt{E} \oplus 0.7\%$	± 3	± 2.5	H$\rightarrow \gamma\gamma$
Preshower detection	$\gamma - \pi^0$ and γ-jet separation, direction measurement and b-tagging with electrons	± 2.4		H$\rightarrow \gamma\gamma$
Jet and missing E_T calorimetry barrel and end-cap forward	$50\%/\sqrt{E} \oplus 3\%$ $100\%/\sqrt{E} \oplus 10\%$	± 3 $3 < \lvert\eta\rvert < 5$	± 3 $3 < \lvert\eta\rvert < 5$	Susy
Inner Detector	30% at p_T=500 GeV Enhanced electron ID τ- and b-tagging Secondary vertex detection at initial luminosities	± 2.5 ± 2.5 ± 2.5 ± 2.5		CP violation, B_s oscillation
Muon detection	10% at p_T=1 TeV in stand-alone mode at highest luminosity	± 3	± 2.2	H$\rightarrow ZZ \rightarrow \gamma\gamma$

Table 1.1: General detector performance goals.

It combines high-resolution detectors at the inner radii with continuous tracking elements at the outer radii, all contained in the central solenoid which provides a nominal magnetic field of 2 T [2].

The momentum and vertex resolution requirements from physics call for high-precision measurements to be made with fine-granularity detectors, given the very large track density expected at the LHC. Semiconductor tracking detectors, using silicon microstrip (SCT) and pixel technologies offer these features. The highest granularity is achieved around the vertex region using semi-conductor pixel detectors. The total number of precision layers must be limited because of the material they introduce, and because of their high cost. Typically, three pixel layers and eight strip layers (four space points) will be crossed by each track. A large number of tracking points (typically 36 per track) is provided by the straw tube tracker, which provides continuous

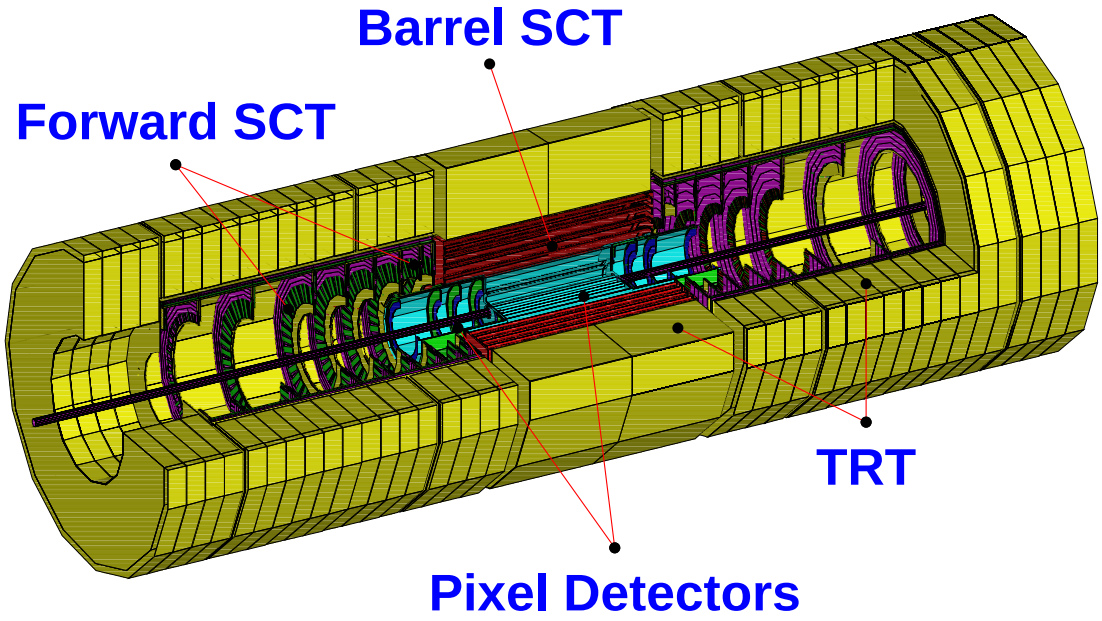

Figure 1.2: Layout of the ATLAS Inner Detector.

track-following with much less material per point and a lower cost. The combination of the two techniques gives very robust pattern recognition and high precision in both ϕ and z coordinates.

The high density of measurements in the outer part of the tracker is also valuable for the detection of photon conversions and of V^0 decays. The latter are an important element in the signature of CP violation in the B system. In addition, the electron identification capabilities of the whole experiment are enhanced by the detection of transition-radiation photons in the xenon-based gas mixture of the straw tubes.

The outer radius of the Inner Detector cavity is 115 cm and the total length is 7 m. Mechanically, it consists of three units: a barrel part extending over ± 80 cm, and two identical end-caps covering the rest of the cylindrical cavity.

In the barrel region, the high-precision detector layers are arranged on concentric cylinders around the beam axis, while the end-cap detectors are mounted on disks perpendicular to the beam axis. The pixel layers are segmented in $R\phi$ and z, while

System	Position	Resolution $\sigma(\mu\text{m})$	η coverage
Pixels	1 removable barrel layer	$r\phi$=12,z=66	$\pm$2.5
	2 barrel layers	$r\phi$=12,z=66	$\pm$1.7
	4 end-cap disks on each side	$r\phi$=12,R=77	1.7-2.5
Silicon strips	4 barrel layers	$r\phi$=16,z=580	$\pm$1.4
	9 end-cap wheels on each side	$r\phi$=12,R=580	1.4-2.5
TRT	Axial barrel straws	170 (per straw)	$\pm$0.7
	Radial end-cap straws	170 (per straw)	0.7-2.5
	36 straw per track		

Table 1.2: Parameters of the Inner Detector as from [2].

the SCT detector uses small angle (40 mrad) stereo strips to measure both coordinates, with one set of strips in each layer measuring ϕ. The barrel TRT straws are parallel to the beam direction. All the end-cap tracking elements are located in planes perpendicular to the beam axis. The strip detectors have one set of strips running radially and a set of stereo strips at an angle of 40 mrad. The continuous tracking consists of radial straws arranged into wheels.

The expected measurement resolutions are summarised in table 1.2 The layout provides full tracking coverage over $|\eta| \leq 2.5$, including impact parameter measurements and vertexing for heavy-flavour and τ tagging.

The secondary vertex measurement performance is enhanced by the innermost layer of pixels, at a radius of about 4 cm, as close as is practical to the beam pipe.

1.3.1 The Semiconductor Tracker

The Semiconductor Tracker system, (SCT), is designed to provide eight precision measurements per track in the intermediate radial range, contributing to the measurement of momentum, impact parameter and vertex position, as well as providing good pattern recognition by the use of high granularity.

The barrel SCT uses eight layers of silicon microstrip detectors to provide four precision points in each of the $R\phi$ and z coordinates, using small angle stereo to obtain the z measurement. The detector has been designed to have a spatial resolution of 16 μm in $R\phi$ and 580 μm in z, per module containing one $R\phi$ and one stereo measurement. The value of the $R\phi$ resolution is justified by the requirement of having a $\Delta p_T/p_T$ <0.3 at P_T=500 GeV/c, while the z resolution value is imposed by the requirement to separate multiple vertices within a bunch crossing and by the necessity to reconstruct the K^0.

Each silicon detector is 6.36*6.40 cm^2 with 768 readout strips of 80 μm pitch. Each module consists of four single-sided p-on-n silicon detectors. On each side of the module, two detectors are wire-bonded together to form 12.8 cm long strips. Two such detector pairs are then glued together back-to-back at a 40 mrad angle, separated by a heat transport plate, and the electronics is mounted above the detectors on a hybrid. The readout chain consists of a front-end amplifier and discriminator, followed by a binary pipeline which stores the hits above threshold until the level-1 trigger decision. The end-cap modules are very similar in construction but use tapered strips, with one set aligned radially. Forward modules consist of strips of either 12 cm length (at the outer radii) or 6-7 cm length (at the innermost radius). The full detector contains 61 m^2 of silicon detectors, with 6.2 million readout channels.

1.4 Physics potential of the Inner Detector

The existence of a high granularity region made of pixels and microstrips in the Inner Detector provides a unique opportunity for the detection of b-mesons whose decay pattern can be resolved with high efficiency. The overall expected yield of b production due to the large cross section of about 0.5 mbarn is of 10^{10} b in the first year of operation, the so called low luminosity run, with $10^{33}\,cm^{-2}s^{-1}$.

B physics is a crucial part of standard and non standard models in many respects.

- Concerning QCD, the correct measurement of b quark jet production allows to subtract, when associated to a prompt photon, one of the main backgrounds to the photon charm production at large p_t, related to the extimate of the intrinsic charm content of the proton and provides by itself, when associated with W production, and accurate estimate of the strange quark parton density.

- The Y production, detectable even at very low p_T where the cross section increases, allows to discriminate among the color singlet production models and the study of $b\bar{b}$ production correlations and asymmetries allows to subtract a source of background to CP violation effects in b-decays.

- Top decays are dominated by the W^+b channel and, in supersymmetric extensions, possibly by the H^+b channel,if allowed by kinematics. Again, a good b detection will lead to a good estimate of the top mass and to stringent limits, if not evidence, for charged Higgs masses.

- CP violation and rare B decays are a central aspect of the ATLAS experimental programme, largely depending on the performance of the inner detector. The "gold plated" decay $B_d \rightarrow J/\Psi K_s^0$ brings a clean signal of CP violation and a mesurement of the β angle of the unitarity triangle: in particular, the reconstruction of the J/Ψ decay into an electron positron pair allows to use the information of the trigger muon for a correct flavour tagging of the B meson. Systematic uncertainties can be estimated by monitoring the "control" decays $B^+ \rightarrow J/\Psi(\mu\mu)K^+$ and $B_d^0 \rightarrow J/\Psi(\mu\mu)K^{*0}$. The overall precision attainable is of 0.012 against the target value of the BaBar collaboration of 0.05. It can further decrease using level two trigger of the inner detector to lower the tagging P_T from 6 Gev to 3 GeV. The $B_d^0 \rightarrow \pi^+\pi^-$ decay represents a rich source of information on CP violations parameters and on the α angle, with challenging problems of background rejection. Together with the B_s^0 oscillation parameter

determination will overconstraint the unitarity relation with three quark generations and represents a severe test of the SM. The $B_s^0 \to J/\Psi\Phi$ decay is not expected to offer a big signal of CP violation and can be used as a test reaction for additional and tiny sources of violation due to non-standard physics.

- The same applies to $B^0 \to \mu^+\mu^-$ decays that would reveal the existence of flavour changing neutral currents largely suppressed in the SM, but present in its supersymmetric extensions without the flavour alignement of quark and squark mass matrices.

- Higgs decay modes into b-$\bar{\text{b}}$ pairs and its associated production are relevant to light Higgs searches, where most of the attention will be focused after the limits/hints from the late LEP runs. Moreover, the Higgs coupling to b quarks in supersymmetric extensions grows with the tanβ parameter and adds interest to the b driven decays/production modes, reinforced by the expectation in the MSSM of a lightest Higgs in the W mass range, below roughly 120 GeV.

The inner detector, besides its central role in B physics, will also be essential for searches for leptonic decays of new massive particles, characterized by large p_T isolated electrons. The lepton tag effectively rejects the QCD hadronic background and allows a full recontruction, for example, of large mass Higgs decay modes into Z pairs. In general, multilepton cascades are taken as signatures of new heavy particle production and, together with missing energy measurements, are an important tool for catching the signals of the production of supersymmetric particles.

Chapter 2

Silicon microstrip detectors

2.1 Introduction

Radiation can be detected via its interaction with the matter that constitutes suitable detectors. Charged particles and photons ionise the constituent atoms of the sensor producing free charges that can either be directly measured or converted into some detectable signal.

Silicon detectors have been used for energy measurements in nuclear physics since 1951 [3] and in particle physics since the 1970s.

After the discovery of charmed particles in 1976, particle physicists started to develop position sensitive semiconductor detectors in order to measure points along tracks with the precision of $\sim 10\,\mu m$. In 1980, Kemmer [4] introduced the planar technique for the production of silicon detectors which allowed the segmentation of the sensor and hence a position measurement of any charged track .

The segmentation of a silicon microstrip detector consists of narrow strips on one side of a *pn* junction. This kind of device allows a simultaneous measurement of the energy deposition in the silicon and of the position of the particles with great accuracy, as will be discussed.

In Chapter 2, the basic properties of silicon detectors are exposed, and the particular technical choices made for the ATLAS detectors are discussed.

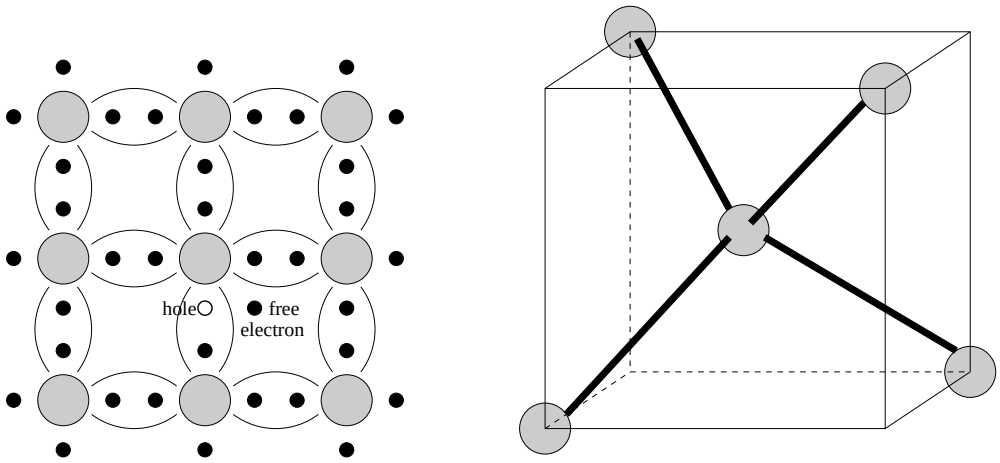

Figure 2.1: Covalent bonds between Si atoms and a cell of silicon lattice.

2.2 Intrinsic and doped Silicon

Silicon is an element of the IV-th group, being characterised by four electrons in its outermost shell. Atoms are bounded by covalent bonds in a lattice crystal of tetrahed structure [fig.2.1]. At low temperature all the electrons participate in the bonds and no free conductors are present in the crystal. At room temperature (300°K) some bonds are broken by the thermal energy acquired by the crystal, and hence some electrons will escape the bonds leaving holes in their place. Any hole can be filled by an electron from a neighbour atom, thus resulting in the net displacement of the hole. Holes can therefore be regarded as positive charges [5], and can be described with a "positive charge mobility". Thermal motion produces new electron-hole pairs while others pairs recombine.

2.2.1 Intrinsic silicon

The number n of energy levels in the conduction band occupied by electrons is given by:

$$n = \int_{E_C}^{E_{top}} N(E)F(E)dE \tag{2.1}$$

where E_C and E_{top} are respectively the energy values at the bottom and at the top of the conduction band, and $N(E)$ is the density of states per unit volume. The probability that a state of energy E is occupied by an electron is described by the Fermi-Dirac distribution $F(E)$ given by:

$$F(E) = \frac{1}{1 + \exp(\frac{E-E_F}{kT})}, \tag{2.2}$$

where k is the Boltzmann constant and T the absolute temperature. The Fermi energy E_F for intrinsic silicon is approximately the halfpoint of the band gap. The density of states $N(E)$ is obtained considering standing waves in an unit volume for which the number of states in a spherical layer of momentum space corresponds to a range of kinetic energy:

$$n = N_C exp\left(-\frac{E_C - E_F}{kT}\right) \tag{2.3}$$

Similarly, the density p of the holes in the valence band reads:

$$p = N_V \exp\left(-\frac{E_V - E_F}{kT}\right), \tag{2.4}$$

N_C and N_V are the effective densities of states in the conduction. In in the valence band, these are proportional to $T^{3/2}$ [12]. E_V is the energy at the top of the valence band.

In an intrinsic semiconductor, the excitation of one electron from the valence band to the conduction band leaves a hole in the valence band, thus the concentration of holes is equal to the concentration of free electrons and the "intrinsic concentration" n_i is introduced as:

$$n = p = n_i = \sqrt{N_C N_V}\exp(-E_G/2kT) \propto T^{3/2}\exp(-E_G/2kT), \tag{2.5}$$

where $E_G = E_C - E_V$ denotes the gap energy. This decreases with the temperature, and for silicon at room temperature E_G=1.12 eV [6].

2.2.2 Doped silicon

The intrinsic concentration of carriers in silicon at 300 °K is $1.45 \times 10^{10}\,\mathrm{cm}^{-3}$ [7]. Taking into account the density of the material, this implies that one out of 10^{12} atoms is ionised. To increase the concentration of carriers, silicon can be doped with impurity atoms. Such impurities must be atoms of the III_{rd} or of the V_{th} group. These will replace some silicon lattice atoms and form covalent bonds with the neighbouring atoms.

The elements of the V_{th} groups, called "donors", have five electrons in the valence shell; four of them form covalent bonds with silicon atoms and the fifth one is only weakly bound (the donor atoms create energy levels near to the top of the band gap) so that the thermal energy is enough to bring it into the conduction band. At 300 °K, all the donors are ionised, hence the concentration of free carriers is equal to the concentration N_d of impurities. A crystal doped with donors is called *n*-type owing to the excess of negative charge carriers. The conductivity in the crystal is mainly determined by the flow of these electrons, called majority carriers while the holes are denoted as minority carriers.

Another type of doping is due to the so called "acceptors", elements of the III_{rd} group. These create electron deficiencies replacing silicon atoms in the lattice. These holes are easly filled by thermal excited electrons coming from silicon atoms. Hence the impurity atoms are ionised and holes are created in the silicon. A crystal doped with acceptors is denoted as *p*-type, and the conduction is mainly due to the holes, its majority carriers.

Before going to the pn junction which is the base of a silicon detector is useful to introduce the concepts of carrier mobility and material resistivity.

The drift velocity v_d of carriers in a semiconductor subject to an electric field E is proportional to the field, for a given temperature:

$$v_d = \mu E.$$

The mobility μ is independent of E as long as $E < 10^3$ V/cm, and in silicon at $100^o\text{K} \leq T \leq 400^o\text{K}$ it varies as T^{-m} where m=2.5 for electrons and m=2.7 for holes [6].

The resistivity ρ is definable as the proportionality constant between the electric field E and the current density J:

$$E = \rho J$$

while it depends on the concentration of free carriers and on their mobilities μ_e and μ_h:

$$\rho = \frac{1}{q(\mu_e n + \mu_h p)}.$$

For intrinsic silicon $\rho \simeq 235\text{k}\Omega\text{cm}$.

When the net impurity concentration $\mid N_d - N_a \mid$ is much larger than the intrinsic carrier concentration n_i, then $n = N_d - N_a$ and $p = N_a - N_d$. So, for p-type silicon it is,

$$\rho \simeq \frac{1}{q\mu_h N_a}, \tag{2.6}$$

and analogously for n-type silicon,

$$\rho \simeq \frac{1}{q\mu_e N_d}. \tag{2.7}$$

2.3 The *pn* junction

If the dopant concentration in a semiconductor changes abruptly from donor to acceptors, the region is called an abrupt *pn* junction.

The gradient of the charge carriers density results in a diffusion of majority carriers across the junction. This diffusion create a space charge region on both sides of the

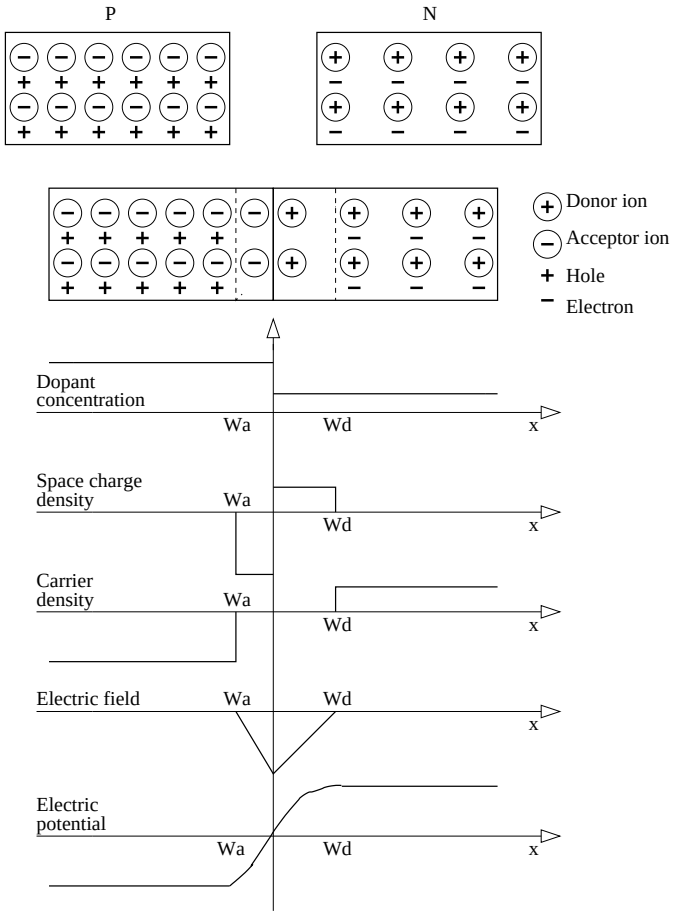

Figure 2.2: Effects of carrier diffusion across a p-n junction.

junction due to unneutralised acceptor and donor ions. This region is called the depletion zone, it has no carriers and is parametrised by W_a and W_d, the widths of the depletion layer in the p and n sides.

The electric field created by the initial migration halts the diffusion process and gives rise to the contact potential [fig.2.2]. The level of this potential barrier depends on the concentration of impurities:

$$V_d = \frac{KT}{q} \ln \frac{N_a N_d}{n_i^2}. \tag{2.8}$$

For the standard concentrations used for silicon detectors the contact potential is a few hundred mV. To enlarge the surface usable as a particle detector, as will be discussed in the following, it is desirable to extend the depletion region to the whole thickness of the detector. This is achieved by reversely polarising the junction, with the application of an external bias tension of the same sign of V_d, the reverse bias. The height of the barrier will become $V = V_d + V_{bias}$.

The behaviour of the potential in the region across the junction is determined by solving the Poisson equation:

$$\frac{d^2V}{d^2x} = \frac{-qN_a}{\epsilon} \quad \text{for} - W_a \leq x \leq 0 \tag{2.9}$$

$$\frac{d^2V}{d^2x} = \frac{-qN_d}{\epsilon} \quad \text{for} \, 0 \leq x \leq W_d \tag{2.10}$$

where ϵ is the dielectric constant.

Fixing both the potential and the electric field to zero for $x = -W_a$, the solution of the Poisson equation reads:

$$V = \frac{qN_a}{\epsilon}\left(\frac{x^2}{2} + W_a x + \frac{W_a^2}{2}\right) \tag{2.11}$$

Since the crystal is neutral, $N_a W_a = N_d W_d$ and the total potential barrier across the junction is then:

$$V = \frac{q}{2\epsilon}(N_a W_a^2 + N_d W_d^2). \tag{2.12}$$

It is of interest to study the depletion thicknesses as a function of the height of the junction barrier potential:

$$W_a = \sqrt{\frac{2\epsilon V}{qN_a(1 + N_a/N_d)}} \tag{2.13}$$

$$W_d = \sqrt{\frac{2\epsilon V}{qN_d(1 + N_d/N_a)}} \tag{2.14}$$

The depletion width varies with the square root of the reverse bias potential, thus it is possible to deplete the whole thickness of the detector provided that a sufficient

external potential is applied.

From equations (2.13) and (2.14) it follows that the width of the depletion regions is inversely proportional to the dopant concentrations. For $N_a \gg N_d$, as it is the case in particle detectors, the depleted zone will then be wide on the n-side and thin on the p-side.

The depletion width in terms of the resistivity from the equations (2.6) and (2.7) reads:

$$W = \sqrt{2\epsilon\rho\mu V}, \tag{2.15}$$

where μ indicates the majority carriers mobility.

It is worth to note that the higher the resistivity of the material, the lower bias voltage is necessary to fully deplete a given thickness.

2.3.1 The junction capacity

Since a reverse biased pn junction consists of an insulating layer between two conducting regions, it acts as a capacitor. The junction capacitance, $C_j(V)$, is defined as the capacitance due to a small change in the bias tension dV divided by the resulting difference in charge dQ,

$$C_j(V) = \frac{dQ}{dV} = \frac{dQ}{dW}\frac{dW}{dV}, \tag{2.16}$$

where $W = W_a + W_d$ is the total thickness of the depletion region.

In the case of an heavily doped (p^+n) junction, $W \approx W_d$ and $Q = qN_d - N_aW_dA$, where A is the area of the junction. It then holds,

$$\frac{dQ}{dW} = \frac{dQ}{dW_n} = q(N_d - N_a)A \tag{2.17}$$

and from the equation (2.10) for $W_d \gg W_a$ it follows:

$$\frac{dW}{dV} = \frac{\epsilon}{q(N_d - N_a)W_d}. \tag{2.18}$$

Substituting equations (2.17) and (2.18) in (2.16) yields:

$$C_j(V) = \frac{A\epsilon}{W_d}. \tag{2.19}$$

The capacity of the junction is exactly that of a parallel plate capacitor with spacing W_d filled by a material of dielectric constant ϵ. Using again equation (2.10), this capacity is written in terms of the bias tension as

$$C_j(V) = A\sqrt{\frac{q\epsilon(N_d - N_a)}{2V}}, \tag{2.20}$$

from which it follows that when the reverse bias is increased, the depletion depth increases linearly and the capacity decreases like $V^{-1/2}$. The capacity is of course minimal once the substrate is fully depleted.

2.3.2 The leakage current

Even though an ideal junction reversely biased can not conduct current, a small current can be observed. This is called "leakage current" and has origins in both the surface and the bulk of the silicon.

The bulk current is generated into the volume of the detector by two sources. The first is the drift of minority carriers across the junction, under the effect of the applied electric field, while the second and dominating effect is the thermal generation of electron-hole pairs in the depletion zone. The behaviour of this generation current I_g is derived in the "Shockley-Read-Hall" theory [5] as:

$$I_g = \frac{qAWn_i}{2\tau}, \tag{2.21}$$

where τ is the effective charge lifetime, inversely proportional to the density of recombination and trapping centres in the depletion region. These centres are levels in the band gap due to impurity atoms (other than the dopant) that catalyze the thermal excitation of electrons from the valence to the conduction band by serving as intermediate states. Electrons from the conduction band and holes from the valence

band can annihilate into these "deep levels".

The generation current strongly depend on the temperature via the carrier concentration n_i, as from the equation (2.5),

$$I_g \propto T^{3/2} \exp(-E_g/2kT). \tag{2.22}$$

At constant temperature the current, being proportional to W also depends on the applied voltage via the relations (2.13) and (2.14)

$$I_g \propto \sqrt{V}. \tag{2.23}$$

The leakage current generated in the bulk increases with the size of the depletion region, finally saturating once the detector is fully depleted.

The surface currents can be due to surface contamination, or the depletion region extending too close to the edge of the semiconductor. These currents are difficult to parametrise and construction methods are devised to limit them, as discussed in the following sections.

Another deviation from the ideal behaviour of the reverse polarised junction is the so called *breakdown*: the passage through the junction of a large reverse current which takes place if a sufficiently high voltage is applied. An avalanche breakdown occurs at the doping concentration of silicon detectors: in the process, the free charges acquire enough energy from the high electric field, and moving through the medium produce new electron-hole pairs by ionization. These can in turn gain enough energy to create further charges. The breakdown voltage can be controlled by the doping level of the bulk. Detectors are manufactured so that breakdown occurs at bias voltages much higher then the expected operating value.

Breakdown should be avoided as it can produce the destruction of the device due to a local melting.

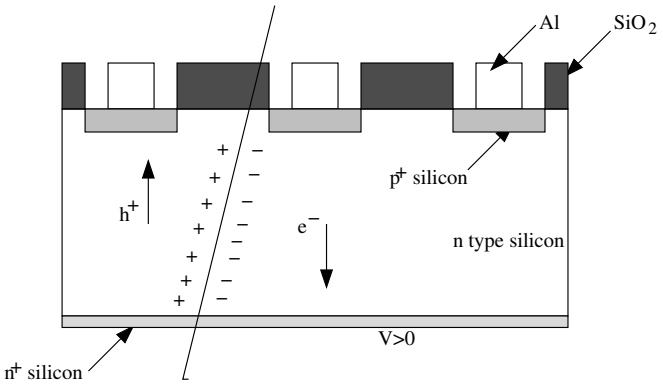

Figure 2.3: Schematic of a silicon detector.

2.4 The silicon micro-strip detector

A *pn* junction is the core of a silicon detector. This is based on the creation of electron-hole pairs by a ionising particle passing through the depletion region of a reverse biased junction. Those carriers are then collected by two electrodes, that also generate the electric field [fig.2.3].

A silicon sensor has good energy resolution. Given the small energy gap, a large number of charge carriers are produced for unit energy loss of a ionising particle traversing the detector. The average energy for creating an electron-hole pair (3.6eV) in semiconductor devices is in fact 10 times lower than the one needed for a ion-electron pair from the ionization of gases and $\sim$ 100 times lower than the one needed for the emission of a photon in a plastic scintillator. This feature is relevant for measurements involving low energy particles when silicon detectors are the main devices for the energy measurements.

Silicon sensors are characterised by a fast response time as the great mobility of electrons and holes in the crystal allows the charge to be rapidly collected ($\sim$10ns). Hence Si detectors can be used in high rate environments.

To achieve a precise position measurement, a fundamental requirement in experimental high energy physics, the p side of the junction is divided into many parallel strips. Each strip acts as an individual silicon detector, as sketched in figure 2.3.

The high density ($2.3\,\mathrm{g/cm^3}$) of silicon reduces the range of secondary electrons preventing large shifts of the centre of gravity of the primary ionization cluster from the track of the particle, allowing an excellent spatial resolution, of the order of μm. The high density of the material also leads to a large energy loss of about $390\,\mathrm{eV}/\mu\mathrm{m}$, corresponding to 108 electron-hole pairs/μm[32]. Therefore thin detectors still produce signals large enough to be detected and satisfy a basic requirement in the construction of high energy physics detectors: a relatively low material tracker. This is a necessary aim both to reduce the multiple scattering, that is pernicious to any tracking procedure, and the energy loss that degradates the subsequent calorimetric energy measurements.

In the following, the basics characteristics of a silicon microstrip detector are described, from the industrial manufacturing process, through its electrical characteristics, to the particle detection and the spatial resolution.

2.4.1 Processing

Silicon microstrip detectors are normally fabricated using the planar technology introduced by J. Kemmer. As shown in figure 2.3, a silicon detector is made by a plate of high purity n-type silicon with strips of p^+ silicon on one side and a layer of n^+ silicon on the other. The p^+ reversely polarises the junction and the n^+ prevents the depletion region from reaching the backplane and ensures a good ohmic contact to the external world. Every p^+ strip is metalised to allow the bonding of strips to thin wires connecting to the readout electronics. High resistivity materials are used in order to fully deplete the detector with the lowest possible bias voltage, as from equation 2.15.

Silicon wafers of thickness of around 300μm and with $< 1, 1, 1 >$ lattice orientation to maximise the energy loss, are used (for the ATLAS experiment).

The production process starts from the cleaning of the n-type wafer and its following oxidation via heating in an oxygen atmosphere at around 1000°C. After a dioxide layer is grown on the crystal surface, it is fully passivated and so protected against moisture and impurities.

The crystal is then covered by a thin layer of photo-resist, which is illuminated through a mask allowing the removal of Si-dioxide in selected areas after its chemical etching. The remaining SiO_2 acts as a mask for implantation of the doping [9].

Boron is used to form the p^+ strips on the top face, these strips are usually between 10μm and 20μm wide, with a pitch of 50/80μm. Arsenic creates an electrical contact on the backplane: the ions are normally implanted after a selection by a mass spectrometer, and are accelerated and guided to the wafer. The chosen energy of the ions determines the depth at which they penetrate the lattice; typical such depths are around 0.5μm [11].

The implantation technique allows an high doping uniformity and a good control of the process but it causes severe damage to the Si crystal surface turning it into an amorphous layer. In addition, mostly of the implanted ions are electrically inactive because they tend to occupy interstitial positions in the lattice, while in order to be active they should sit into vertex positions of the crystal replacing the original silicon atoms. Both these issues are addressed by a heat treatment, that implies the annealing of the detectors between 600 and 800°C.

Aluminaization by evaporation on both surfaces of the wafer provides the ohmic contacts for the detector to ensure that the metal contact exist only over the implanted regions, the same technique of photo-lithography and etching as for the oxide is used. A bonding pad is formed at the end of each strip to allow the ultrasonic soldering of one bonds to the readout electronics. Once the detector is complete and operational,

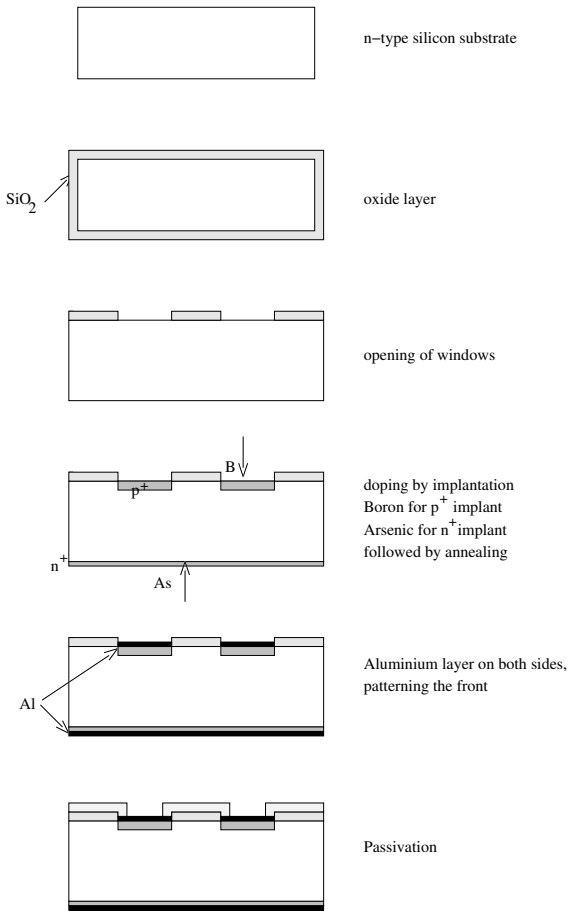

Figure 2.4: The planar process for detector fabrication.

the junction region is further protected from mechanical and atmospheric degradation by passivating its top side with an additional Si-dioxide layer $0.5 \div 3 \mu$m thick and then is cut. Figure 2.4 schematically shows the different phases of the fabrication process.

The capacitance between a strip and its neighbours is a very important parameter as it dominates the single strip capacitance seen by the amplifier, a fundamental component in the noise performance of the system. This capacity depends linearly on the ratio of the strip width to the strip pitch [10].

The coupling of the strips to the readout electronics, the biasing scheme and the

guard rings structure have an impact on the final performance of the detectors and are discussed in detail in the following subsections.

2.4.2 Strip coupling

If the aluminium is placed directly on top of the p^+ implantation, the resulting strips are referred as *dc coupled*. This technique has the disadvantage of allowing the leakage current to flow directly into the attached amplifier, possibly driving the electronics into saturation. Moreover, as the reverse current can vary from strip to strip and with time, *dc* coupled strips are likely to result in large base line shifts between different channels of the readout chip, requiring a considerable dynamic range of the subsequent ADCs. The solution is either the use of a current sink in the amplifier, or a modification to the coupling of the strips. A thin insulating layer separating implantation and metallisation can act as a capacitor between the strip and the readout electronics preventing the flow of current: strips are now told to be *ac coupled*. The capacitor value can be tailored by varying the thickness of the insulator, usually silicon oxide or nitride. The coupling capacitance must be sufficiently high in comparison with both the capacitance between the strip and the backplane and the inter-strip capacitance.

2.4.3 Detector biasing

Strips are biased via a common bias line in order to achieve an homogeneous potential for all of them, avoiding field distortions. The bias line is a p^+ implant running across all the strips and connected to each one via a bias resistor that is usually made of an extra polycrystalline film on top of the SiO_2 [fig.2.5]. The value of the polysilicon resistor is optimised to be a good compromise between a good strip insulation and a low source of noise, as discussed in the following. It can be changed varying the

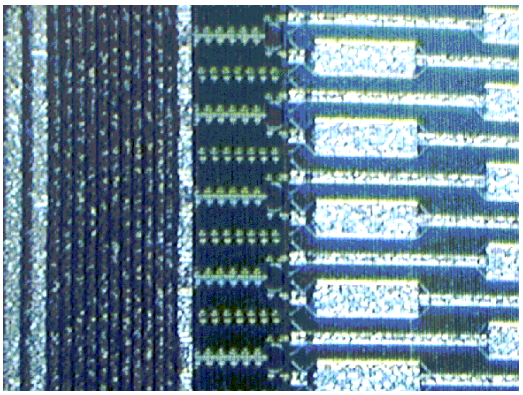

Figure 2.5: Bias line, polysilicon resistors and strip pads of an ATLAS prototype detector.

polysilicon length and width.

2.4.4 The guard rings

The guard ring structure is a feature specially made to minimise the surface leakage current and avoid possible electrical breakdown. The surface leakage current is due to charge accumulation at the interface between Si and Si-oxide. In fact the always present positive charge in the SiO_2[12] causes electrons to accumulate at the top edge of the n-bulk [fig.2.6]. This charge influences the width of the depletion region,

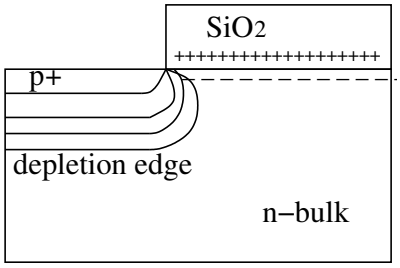

Figure 2.6: Field curvature enhanced by positive oxide charge.

that would be narrower along the surface should this charge be absent. Moreover,

a constant potential difference across the junction, and a reduction of the depletion width determine the increase of the field in the silicon close to the interface with the SiO_2 [13], increasing the probability of avalanche breakdown occurrence.

The field near the cut edge of the detector, a region of high pair recombination and generation, also favours high leakage current.

The probability of current breakdown can be reduced by the presence of floating guard rings all around the strips [fig.2.7]. These are a p^+ implantation and act in the

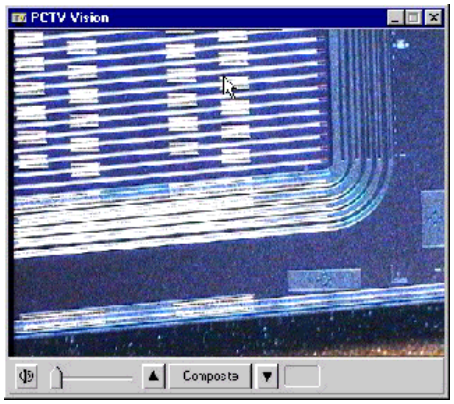

Figure 2.7: The corner of a silicon microstrip detector . The guard rings structure surrounds the strips region.

following way: as the bias voltage is increased, the depletion regions surrounding the central implant and the first guard ring meet, reducing the crowding of carriers at the implant edge. As the bias increases further, the depletion region punches through more guard rings [14]. If the potential is distributed as evenly as possible among the guard rings, the surface depletion region is prevented from reaching the cut edge of the device. In this way the detector can be biased to a higher voltage before the breakdown occurs.

2.5 Particle detection

The characteristics of silicon detectors make them the ideal device to be used for tracking purposes in High Energy Physics.

Moderately relativistic particles that traverse a silicon sensor lose energy mainly via ionization. The mean energy loss dE per unit length dx, or "stopping power", is given by the Bethe-Bloch formula:

$$\frac{dE}{dx} = 2\pi N_a r_e^2 m_e c^2 \rho \frac{Z}{A}\frac{z^2}{\beta^2}\left[ln\left(\frac{2m_e\gamma^2 v^2 W_{max}}{I^2}\right) - 2\beta^2 - \delta - 2\frac{C}{Z}\right] \tag{2.24}$$

where N_a is the Avogadro number, r_e and m_e are respectively the electron radius and mass, c is the speed of light in the vacuum, ρ, Z and A are the density, the atomic number and the atomic weight of the absorbing material, z is the charge of the incident particle and I the mean excitation energy. For the incident particle, $\beta = v/c$ and $\gamma = 1/\sqrt{1-\beta^2}$ and W_{max} is the maximum energy transfer. The last two terms are the density and shell corrections [7].

Figure 10.2 shows that for particle momenta above 10GeV/c the energy loss falls to a broad minimum. Particles with this momentum are generally referred to as minimum ionising particles, or MIPs.

The energy loss of electrons with energies above a few MeV is a combination of ionization and bremsstrahlung, depending on the atomic number of the absorber material. To a good approximation, the energy loss in silicon detectors of electrons in this energy range is the same as that of MIPs.

The Bethe-Block formula describes the mean energy loss and for thick absorbers statistical fluctuations have to be taken into account resulting into a gaussian distribution of the stopping power. For thin absorbers the distribution is asymmetric, with a long tail in the high energy loss region (fig. 2.9). A silicon detector with a thickness of around 300 μm is considered as a thin absorber and the energy loss is described by the Landau theory, that takes into account the probability for large energy transfers

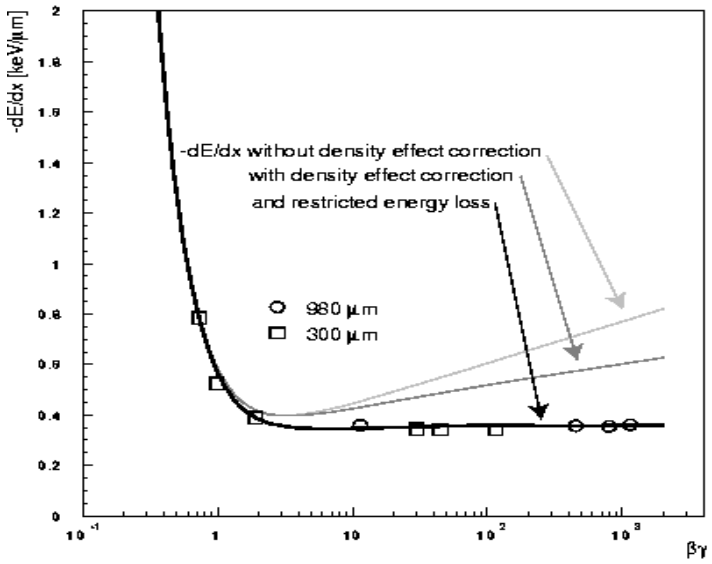

Figure 2.8: Mean energy deposition in silicon as a function of the particle energy as from reference [8] .

in a single collision. Nevertheless, this theory assumes a free electron cross section neglecting the atomic bonds [15] resulting in a measured distribution that is broader than the predicted one. A Gaussian distribution convoluted with a Landau curve reproduces well the experimental data.

For a MIP traversing a 300 μm thick silicon detector, the most probable energy loss is 81 keV [16]. An energy of 3.6 eV is required to create an electron-hole pair in Silicon, hence the charge most likely deposited by a MIP amounts to 22500 pairs, corresponding to 3.6 fC.

2.5.1 Charge collection

After creation, electron-hole pairs are separated by the electric field (the detector is reverse biased) and drift inducing signals on the electrodes. Holes drift toward the p^+ strips while the electrons drift toward the backplane. This process is referred as

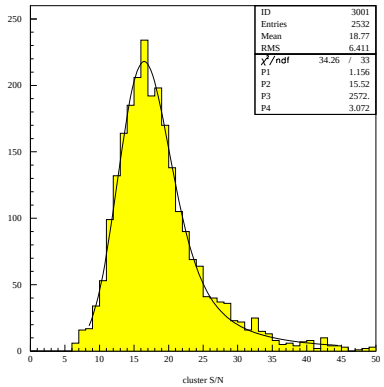

Figure 2.9: Typical signal to noise ratio distribution, measured in a silicon detector $300\,\mu m$ thick. This quantity is proportional to the energy loss.

"charge collection".

During the drift, the carriers also diffuse by multiple collisions, and this effect will be discussed in the next section.

The charge collection time at the electrodes decreases with increasing bias voltage and is also a function of the position in which the charges are created [16].

More in detail, for a reverse polarised p^+n junction with a bias voltage greater then the full depletion voltage V_{fd}, the total current as a function of time depends on the over-depletion voltage $V_{od} = V - V_{fd}$. It reads [17]:

$$\begin{aligned} I(t) \;=\; & \left[E_{max}\left(1+\frac{V_{od}}{E_{max}d}\right)^2 \exp\left(-\frac{\mu_e E_{max} t}{d}\right) - \frac{V_{od}^2}{E_{max}d^2}\,\exp\left(\frac{\mu_e E_{max} t}{d}\right)\right] \\ & \left[Q_g \frac{\mu_e}{2}\sigma(t^e_{max})\right] + \\ & \left[E_{max}\left(1+\frac{V_{od}}{E_{max}d}\right)^2 exp\left(-\frac{\mu_h E_{max} t}{d}\right) - \frac{V_{od}^2}{E_{max}d^2}\,\exp\left(\frac{\mu_h E_{max} t}{d}\right)\right] \\ & \left[Q_g \frac{\mu_h}{2}\sigma(t^h_{max})\right] \end{aligned} \tag{2.25}$$

where E_{max} is the maximum electric field (at depletion), d the detector thickness, $\mu_{e,h}$ the carriers mobility, Q_g the generated charge per unit length, and $t^{e,h}_{max}$ are the maximum collection times for electrons and holes. This equation is obtained

neglecting the diffusion of carriers and taking into account only the drifting due to the electric field. The two terms contribute to the total current only if free carriers are present, which is accounted for by the function:

$$\sigma(t_{max}^{e,h}) = \begin{cases} 1 & \text{if } 0 \leq t \leq t_{max}^{e,h} \\ 0 & \text{otherwise} \end{cases}$$

Figure 2.10 shows the evolution of $I(t)$ and of its integral with respect to the time (i.e. the charge collected at the electrodes) for a 300 μm detector overdepleted of 20 V. After their creation, the charge carriers drift towards the electrodes where they are absorbed at the arrival. As holes have a lower mobility (480cm^2/Vs [32]) than electrons (1350cm^2/Vs [32]), the falling edge of the current is divided into two parts. When the last carrier arrives, the current becomes zero and the collected charge reaches a "plateau". The lenght of the falling edge of the current or, equivalently of the rising edge of the charge, is approximately 25 ns.

For bias voltages higher than the full depletion voltage, the maximum charge collection time can be expressed as:

$$t_{max}^{e,h} = \frac{d}{v_{e,h}} \ln\left(1 + \frac{E_{max} d}{V_o d}\right) \qquad \text{for } V_{od} > 0 \tag{2.26}$$

with $v_{e,d}$ representing the carriers drift velocities. As already anticipated, the charge collection time decreases with the over-depletion. For $V_{od} = 0$ this time diverges

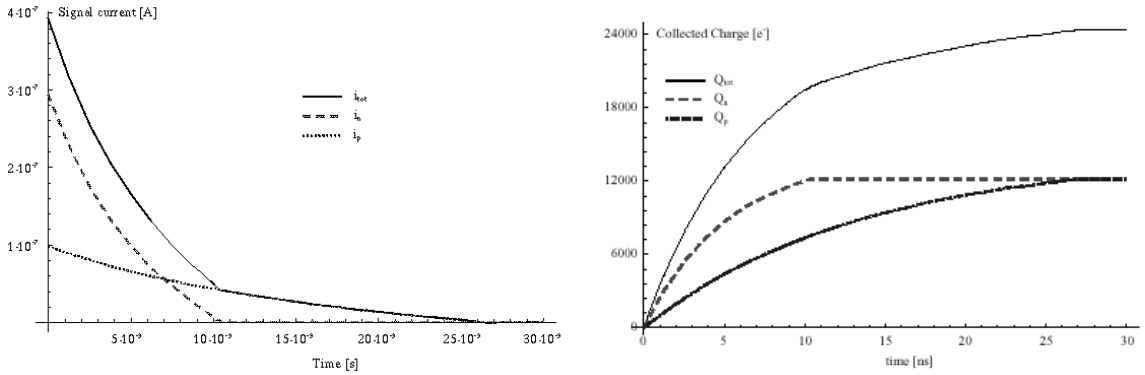

Figure 2.10: Current as a function of time (left) and its integral (right) for a 300μm thick detector, doped at 10^{12}/cm^3, and overdepleted of 20 V.

as consequence of having neglected the charge diffusion. Figure 2.11 presents the dependence of $t_{max}^{e,h}$ on V_{od}.

The current pulse at the strip appears on the top of the leakage current and is then

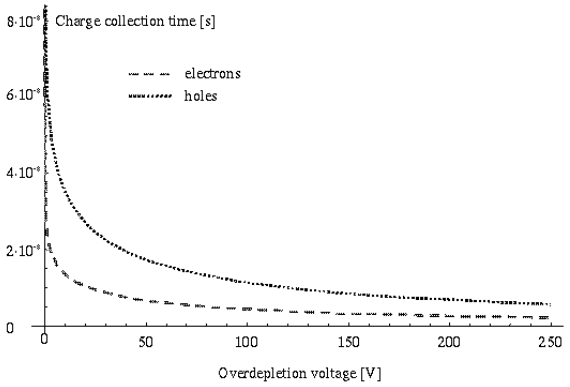

Figure 2.11: Charge collection time as a function of the over-depletion voltage for a 300μm thick detector, doped at $10^{12}/\text{cm}^3$.

amplified and integrated by the read-out chip to measure the total charge deposited into the detector. Since all the strips are readout, the strip to which the signal arrives gives information on one coordinate of position of the traversing particle. The resolution of the position measurement will be discussed in the next section.

2.6 Spatial resolution and noise

The spatial resolution of microstrip detectors depends on both physical and external parameters. The physical parameters are the statistical fluctuations of the energy loss and the diffusion of carriers during the drift. External parameters include the strip pitch and the noise of the readout electronics.

As mentioned in the previous section, high energy electrons make the distribution of the energy loss asymmetric. These electrons, due to their long range, produce secondary ionisation a few μm away from the particle track hence degrading the

energy resolution.

Electrons and holes diffuse during the drift towards the electrodes due to the multiple scattering and the distribution of the charge carriers around the track is described by a Gaussian function:

$$\frac{dN}{N} = \frac{1}{\sqrt{4\pi Dt}} \exp(-\frac{x^2}{4Dt})dx. \tag{2.27}$$

In the above formula, dN/N indicates the fraction of carriers that can be found in a length element dx at distance x from the track after a time t. D is the diffusion coefficient, proportional to the mobility and hence different for electrons and holes. The root mean squares of the distribution, is

$$\sigma = \sqrt{2Dt} \tag{2.28}$$

and is equal for both carriers since the drift time is inversely proportional to the mobility.

The spread of the charge can causes its collection on more adjacent strips. The standard deviation of the charge distribution of a MIP in a 300 μm thick silicon detector is of the order of 10 μm [32] and with readout pitchs larger than the diffusion width, as it will be in ATLAS, the effect of the diffusion on the spatial resolution is small.

In a detector characterised by a strip pitch larger than the diffusion width, the coordinate of the particle is simply given by the hit strip and the final resolution, dominated by the strip pitch, is given by the sigma of a binary distribution:

$$\sigma = \frac{pitch}{\sqrt{12}}. \tag{2.29}$$

Inserting in the above formula the ATLAS strip pitch of 80 μm, the σ corresponds to 23 μm.

For particles crossing the detector at large angles, the produced charge is shared between more strips. The position is determined by the charge center of gravity what allows to achieve a more precise localisation .

The spatial resolution also depends on the signal to noise ratio (S/N). The noise determines the minimum measurable signal on a strip and so particular care must be devoted in keeping it as low as possible. This becomes crucial for multiple strip events because silicon presents no charge multiplication and the spread of the primary ionisation on several strip leads to very small signals that can be lost.
The S/N contribution to the resolution can be approximated by

$$\sigma = K\frac{N}{S}pitch \tag{2.30}$$

where the constant K depends on the detector geometry [18].

2.6.1 Sources of noise

The electronics and the detector itself contribute to the noise in different ways. The electronic noise is a sum of a constant, that depends on the particular readout chip, and of a part which is a function of the detector parameters. The main contribution comes from the inter-strip capacitance and from the bulk capacitance that acts as a capacitive load for the chip preamplifier. In the latter, the charge coming from the detector is integrated on a feedback capacitor C_f and the output voltage is proportional to the input charge. This occurs into a charge sensitive amplifier, whose scheme is presented in figure 2.12. The second stage of the amplifier is a shaper circuit and its time constant plays an important role in the noise performance of the system.
The input signal from the detector is a charge signal, and it is convenient to express the preamplifier noise in terms of the electrical charge. The equivalent noise charge (ENC) is the charge which would generate an event producing a signal of the same amplitude of the mean noise of the system.
For charge sensitive amplifiers built with bipolar transistors, the main contribution to the ENC is given by the Johnson noise in the base spreading resistance and by the

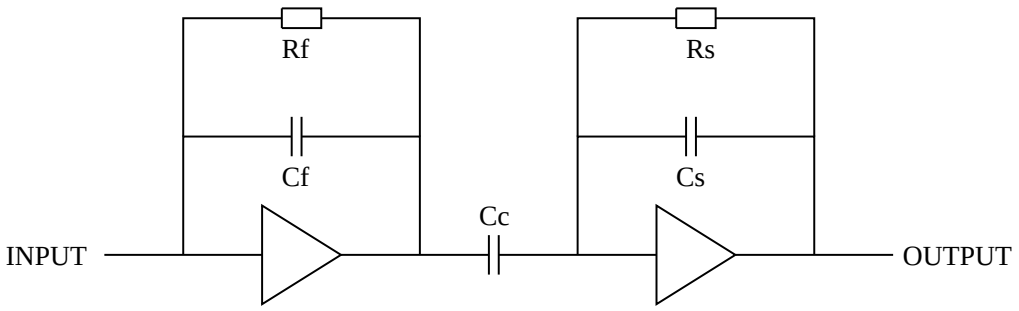

Figure 2.12: Diagram of a charge sensitive preamplifier and "CR-RC" shaper.

collector shot noise [33]. The total can be expressed by:

$$ENC_c = \frac{e}{q}\sqrt{\frac{4kT(R_{bb} + \frac{1}{2g_m})}{T_p}}\, C_d, \tag{2.31}$$

where e indicates the Neper number, q the electron charge, k the Boltzmann constant, T the absolute temperature and R_{bb} the base spreading resistance. For a bipolar transistor, the transconductance $g_m = qI_c/kT$, with I_c representing the collector current. Finally, T_p is the peaking time of the shaper circuit and C_d is the detector capacitance seen by the preamplifier.

Other contributions to the noise arise from the detector leakage current and from the bias resistor [19]. The equivalent noise charge due to the detector leakage current is given by :

$$ENC_I = \frac{e}{q}\sqrt{\frac{qIT_p}{4}} \tag{2.32}$$

where I is the leakage current of a single strip, while the contribution of the bias resistor R to the noise is:

$$ENC_R = \frac{e}{q}\sqrt{\frac{T_p kT}{2R}}. \tag{2.33}$$

The total equivalent noise charge is expressed as

$$ENC = ENC_c \oplus ENC_I \oplus ENC_R. \tag{2.34}$$

In order to keep the noise at reasonable levels, special care must be exercised in the detector design, in particular in the choice of the inter-strip capacitance and bias resistor values. In chapter 4, the particular choices made for the ATLAS microstrip detectors will be discussed.

Chapter 3

Radiation damage on silicon detectors

The silicon detectors used in the LHC experiments will be exposed to an unprecedent radiation environment. The fluence expected in ten years of LHC operation have been estimated to be $3 \times 10^{14}\,\mathrm{p/cm^2}$ [2]. This enormous flux of radiation, due to the particles that one wants to detect, will cause severe damage to the silicon sensors and to the electronics. The study of this damage and the consequent degradation of the electric performance is of utmost importance to design the apparatus and to understand its performance after the start of the data taking.

3.1 Radiation damage in silicon

When silicon sensors are exposed to radiation, this latter interacts both with the silicon atomic electron cloud and with the nuclei in the lattice. While the interaction with the electron cloud in silicon is a transient effect that is indeed used for the detection of this radiation, the interaction with the lattice may lead to permanent material changes, which often are of detrimental nature.

The dominant mechanism of primary defect formation in silicon exposed to radiation is the elastic collision of an incoming high-energy particle with an atom of the crystal lattice [20]. The primary knocked atom (PKA), that has obtained an excess

momentum, starts moving but is exposed to the stopping influence of neighbouring atoms. If the momentum is low, the atom oscillates around the site, otherwise it may depart from its site over a distance of several lattice constants. In this case a Frenkel pair [21] is created, corresponding to an interstitial, an atom between regular lattice sites, and a vacancy, at the empty lattice site.

The diffusion gives rise to an interstitial and vacancy migration process. This may lead to two opposite effects: pair annihilation, namely the repositioning an interstitial inside the empty lattice site, or the formation of a complex defect between vacancies, interstitials and atom impurities already present in the semiconductor bulk.

A defect that has a great probability to be created is a combination of a vacancy plus a shallow impurity and a divacancy V_2, a complex formed by two neighbouring vacancies [22]. These traps, spatially well localised inside the semiconductor lattice, are called "point defects".

In the case of heavy incident particles, like neutrons or protons, sufficient energy can be transferred to the PKA so that a multiplicity of secondary displacements occurs in a region with a radius of a few hundred angstrom. Isolated interstitial atoms and vacancies are then formed along the PKA trajectory. As the kinetic energy of the individuals atoms decreases during the collisions, the distance between the collisions also decreases until it becomes comparable with the inter-atomic distance. A considerable amount of energy is concentrated in the final part of the PKA path over a short time (10^{-13}-10^{-12}s) and in a small volume (10^4 atoms). This leads to collective atomic rearrangement in this region and to the formation of random and irregular clusters of vacancies, surrounded by an envelope of interstitial atoms escaping from the centre of the disturbed region, called the depleted zone [21]. For high energy of the incident particles, these cascades exhibit a tendency to separate into sub-cascades, as shown in figure 3.1.

Due to termal motion, point defects and clusters interact during and after irradi-

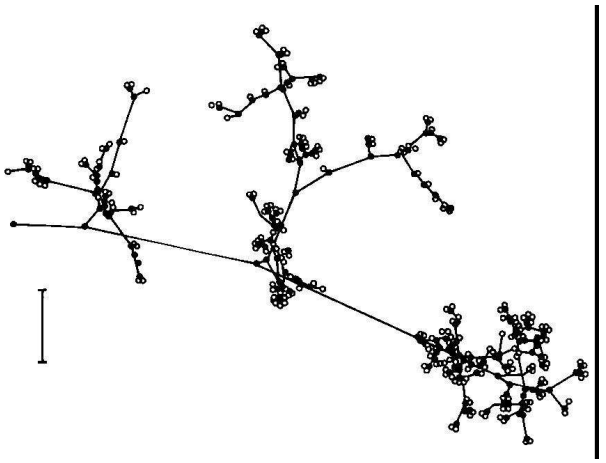

Figure 3.1: Computer simulated cascade in a semiconductor (the marker corresponds to 20 atomic distances).

ation. In this process it is possible for some of them to annihilate, or become even more complex.

3.2 Damage dependence on the type of radiation

For two reasons the probability for the creation of a PKA and its energy distribution depend on the type and energy of the incident radiation: first, the elastic cross section for scattering on silicon atoms depends on the type of radiation, and, second, the kinematics and the energy transferred to the silicon atom is strongly dependent on the mass of the incident particles.

These dependencies, moreover, are to a large extent smoothed out by the secondary interaction of the PKA.

It is therefore customary to scale measurements on radiation damage from one type of radiation and energy to another. As the interaction of radiation with electrons produces ionization but no crystal defects, the quantity used for scaling is the non ionising energy loss (NIEL). The dependence of this variable on the energy and type

of radiation (normalised to 1 MeV neutrons) is shown in figure 3.2.

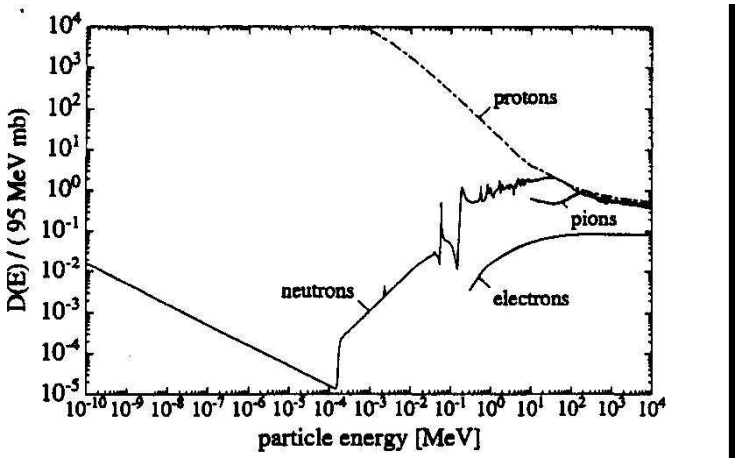

Figure 3.2: Energy dependence of non ionising energy loss in silicon for various types of radiation. The displacement damage cross section D(E) is directly proportional to the NIEL.

3.3 Radiation damage in the surface region

Another effect observed in silicon detectors after irradiation is the occurrence of surface damage in the devices. As already pointed out in the second chapter, the Si-SiO_2 interface in silicon detectors is in fact characterised by the presence of a net density of positive charges in the SiO_2 as well as by the existence of interface traps. The oxide charge consists of fixed-charge, mobile positive impurity ions and trapped holes. While the first two components depend on processing conditions, the last one is created by irradiation [23].

Electron-hole pairs are generated in the oxide as a result of energy absorption: the recombination rate is higher in case of heavy charged particles, for which the trapped hole production is then lower. This type of damage is therefore mainly caused by electrons and photons.

Electrons and holes which escape from recombination move in the electric field: electrons are swept out from the oxide, while holes, less mobile than the electrons, move slowly in the opposite direction and are eventually captured at the oxide-silicon interface in deep traps. The accumulation of positive charge due to hole trapping saturates at high radiation doses [24].
The surface damage effects are very sensitive to the quality of the oxide covering the surface of the detector.

3.4 Changes to the detector properties

The radiation gives rise to a distortion of lattice symmetry introduced by point defects, clusters and impurity complexes. This in turn reflects in a multiplicity of discrete energy levels inside the silicon energy gap. These energy levels may act as generation-recombination centres or as trapping ones, affecting the electrical operation of the device. In particular, the centres have three main characteristics:

- they are able to capture and emit electrons and holes. In the depletion region, alternate emission of carriers leads to an increase of the leakage current with a consequent decrease of the signal to noise ratio and increase of power consumption.

- they can capture and re-emit electrons and holes with some time delay. When signal charge is trapped in the depletion zone, it may be released too late for an efficient detection, causing a reduction of the signal.

- they can change the charge density in the space-charge region, thus requiring an increased bias voltage to make the detector fully sensitive.

In the following, the effect of radiation on the intrinsic properties of the silicon detectors and on their operating conditions will be discussed in detail.

3.4.1 Reverse current

The reverse current of an irradiated detector increases mainly because of the rise of the generation current, that is caused by the creation of traps in concentrations proportional to the fluence. The energy levels of those traps are situated in the middle of the forbidden gap.

Another small effect contributing to the increase of the total leakage current is the appearance of a surface current caused by the formation of states in the SiO_2/Si interface which become active for carrier generation [20].

Measurements of the leakage current have been carried out as a function of the radiation fluence [25], [26]. The result, presented in figure 3.3 clearly shows the pro-

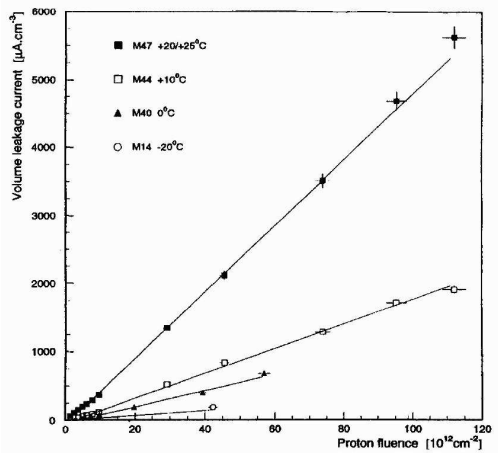

Figure 3.3: Volume leakage current as a function of protons fluence for detectors irradiated and always kept to the indicated temperature from reference [26].

portionality of the volume leakage current (defined as $I_{leak}/volume$) to the fluence Φ.

$$I_{vol} = \alpha\Phi \tag{3.1}$$

The proportionality constant α is strongly temperature dependent because of the dependence of the current on the carrier density which is in turn temperature dependent

(Boltzmann relation, 2.22).

In chapter 6, measurements performed in the framework of this thesis work and carried out on ATLAS prototype detectors will further quantify the effect of irradiation, on the current, as well as on all the relevant detector characteristics.

3.4.2 Effective doping and depletion voltage

In a non irradiated detector, the effective doping concentration N_{eff} is determined by shallow dopants in the material. Further energy levels are created in the middle of the band gap by radiation. These levels are, as experimentally shown, mainly of the acceptor type. Due to these acceptor deep levels, negative charges accumulate in the depletion region and cause n-type silicon to become less n-type with increasing fluence. At this point, the negative charges compensate the positive charge of the donor impurities. With further increasing fluence the material behaves more and more as p-type. This inversion is not the physical removal of the donors in the n silicon, but rather an increase of acceptors.

The plot of figure 3.4 shows that the effective doping concentration for n-type silicon

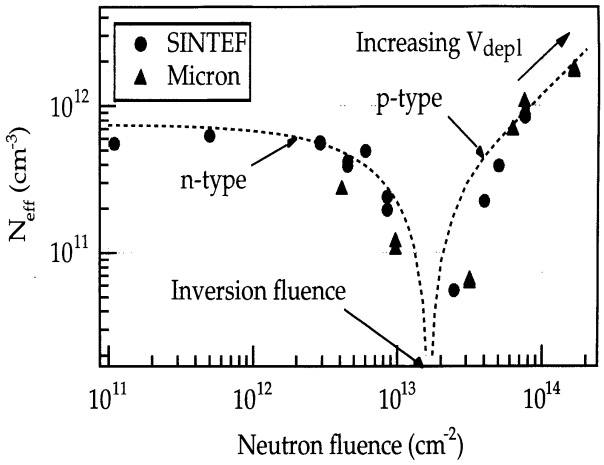

Figure 3.4: N_{eff} as a function of neutron fluence for two high resistive n-type diodes [27].

wafers decreases with irradiation and that the materials become intrinsic at an irradiation fluence of a few times 10^{13}. Above this value, the doping becomes effectively p-type and eventually rises with the fluence.

A parametrisation of the effective doping is:

$$N_{eff}(\Phi) = N_{eff}(0)\exp(-c\Phi) - \beta\Phi \tag{3.2}$$

where the first term takes into account the donor compensation, while the second refers to acceptors creation. The value of β gives the number of activated acceptor sites created by one incident particle while passing through a unit thickness of material (1 cm).

As a result of the inversion, the junction of a p^+n detector moves to the backside (n^+) from where the detector now starts to deplete. It is worth to note that the sensor remains operational even after inversion. A consequence is that, if the detector is not fully depleted, the signal charges produced by a traversing particle will have to move through a layer of non depleted silicon before being collected at the strips. This can lead to a lower registered signal. So, special care must be devoted in keeping the detectors always fully depleted.

The change of doping concentration reflects in a change of the depletion voltage V_{fd} [28]:

$$V_{fd} = \frac{qW_{fd}^2 N_{eff}}{2\epsilon}, \tag{3.3}$$

where q is the electron charge, W the detector's full depletion depth and ϵ the silicon permettivity.

The behaviour of the depletion voltage with fluence is therefore similar to that of N_{eff}: decreases until the type inversion point and then rises again with increasing fluence.

3.5 Annealing effects and their parametrisation

The performance of the detectors after irradiation is strongly dependent on time. There is in fact a long term evolution of the reverse current and of the full depletion voltage after the end of the irradiation. In particular, the damage decreases with time with a rate strongly dependent on the temperature.

As this observation can be interpreted as a partial disappearance of radiation-generated crystal defects, this effect has been dubbed *"annealing"*. The annealing of silicon detectors has been extensively studied leading to parametrisations of the observed effects. It has been found that after irradiation the leakage current of a sensor, annealed at a certain temperature, decreases exponentially with time and then tends to stabilise after several months.

The behaviour of the reverse current can be parametrised as a function of the time t as:

$$\frac{I(t)}{I(0)} = \sum_{i=1}^{n} A_i \exp -\frac{t}{\tau_i} \tag{3.4}$$

The numerical values for relative amplitudes and corresponding time constants τ_i are given in the table 3.1, as from reference [12].

The behaviour of the depletion voltage, and of the carrier concentration of a detector after irradiation is found to be more complicate: it has been in fact observed that, after an initial decrease of doping charge during the first week of room temperature annealing (beneficial annealing), there is a new increase of N_{eff}, it means a "reverse annealing" period. An explanation for such behaviour is the transformation of radiation induced electrically inactive defect complexes into electrically active defects.

In addition, the data exhibit a strong temperature dependence: the beneficial annealing period is of the order of one week for detectors annealed at room temperature while it become longer if the sensors are annealed at lower temperature [29].

The Ziock parametrisation [30] is based on experimental results from irradiation of silicon sensors and describes the annealing of the depletion voltage in terms of two

Time constant τ_i(min)	Relative fraction A_i
Before type inversion	
$(1.78 \pm 0.17) \times 10^1$	0.156 ± 0.038
$(1.19 \pm 0.03) \times 10^2$	0.116 ± 0.003
$(1.09 \pm 0.01) \times 10^3$	0.131 ± 0.002
∞	0.303 ± 0.006
After type inversion	
$(1.35 \pm 0.03) \times 10^1$	0.197 ± 0.010
$(8.43 \pm 0.02) \times 10^1$	0.300 ± 0.002
$(1.55 \pm 0.40) \times 10^3$	0.121 ± 0.002
∞	0.243 ± 0.003

Table 3.1: Relative fractions and annealing time constants for volume-generated leakage currents of n type silicon before and after type inversion.

annealing time constants which depend exponentially on the temperature.

The short-term beneficial annealing period is dominated by the time constant τ_s which describes the exponential decay of the active acceptor sites created during the irradiation period back to neutral inactive sites. That region, at the time t after the end of the irradiation, is described by:

$$V_{fd}(t) = V_z + V_s \exp -\frac{t}{\tau_s} \tag{3.5}$$

where V_s is related to the meta-stable acceptor concentration directly produced during the irradiation process and V_z is due to the fraction of the acceptor concentration produced by radiation, which is stable. Therefore V_z is the minimum value of the depletion voltage between the beneficial and the reverse annealing regions.

Extracting τ_s from a series of measurements at various temperatures between -10°C and 21°C yields an exponential expression as a function of the temperature T (in°C):

$$\tau_s(T) = 70 \exp -0.175\, T \text{ days.}$$

V_z and V_s depend on the fluence ϕ and can be expressed as:

$$V_z = \nu_z \, \phi V_s = \nu_s \, \phi$$

where the constants $\nu_z = 1.06 \times 10^{-12}\,\mathrm{Vcm}^2$ and $\nu_s = 1.34 \times 10^{-12}\,\mathrm{Vcm}^2$ have been determined from measurements at different fluences.

The reverse annealing part (long term annealing) is described by the following expression:

$$V_{fd}(t) = V_z + V_A(1 - \exp -\frac{t}{\tau_l}) \qquad t \gg \tau_s. \tag{3.6}$$

V_A is related to the concentration of defects that become active acceptor sites and is defined as $V_A = \nu_A \, \phi$, where $\nu_A = 3.80 \times 10^{-12}\,\mathrm{Vcm}^2$. τ_l is the long term annealing constant and it is defined as:

$$\tau_l(T) = 9140 \exp -0.152\,T \text{ days } (\mathrm{Tin^\circ C}).$$

It is worth to emphasise that in the Ziock parametrisation V_A, V_s and V_z are independent of the temperature and only linearly dependent on the fluence while the time constants only depend on the temperature.

In chapter 6, experimental results on irradiated detectors will be shown and will be compared to the models described above.

Chapter 4

Quality evaluation of prototypes of the ATLAS silicon detectors

4.1 Specifications for ATLAS Silicon Microstrip detectors

The active inner part of the ATLAS detector will be constructed using silicon sensors. They will operate in an un-precedent radiation environment that will deteriorate their performance. Nevertheless, this performance has to remain satisfactory for at least 10 years of LHC operation.

The design, simulation, prototyping and evaluation of microstrip detectors capable of matching these challenging requirements have been in progress for several years. The result of the joint work of laboratories and commercial suppliers is the design of a "radiation hard detector". These detectors will of course be affected by radiation: their operation point will be altered either with very high depletion voltage due to radiation damages in the bulk, and with a rise of the charge density at the Si-SiO_2 interface with related high field problems caused by surface damages. An appropriate choice of materials and electrical characteristics can nonetheless still ensure an acceptable performance of the detectors, namely their signal to noise ratio and a satisfactory spatial resolution. For that reason a list of technical specifications which must be satisfied by the ATLAS silicon microstrip detectors has been established by

the SCT Collaboration.

The ATLAS tracker requires different geometries for the silicon wafers, according to their position with respect to the interaction point (forward or barrel)[2] . Each detector has an active area of approximately $6{\times}6\,\mathrm{cm}^2$ containing 768 strips, all read out.

Some of the pre-irradiation specifications for the ATLAS Silicon microstrip detector are reported in the following. Other details as the geometrical specifications, can be found in reference [31].

Mask and mechanical requirements

- Read-out strips: aluminium, capacitively coupled over $18-20\mu$m p-implant wide strips with $80\,\mu$m pitch.
- Passivation: Detectors to be passivated on the strip side
- Thickness: $285\pm15\mu$m or $260\pm10\mu$m according to the detector position in the tracker.

Electrical properties

- Strip resistivity: $\leq 200\,\mathrm{K}\Omega/\mathrm{cm}$
- Al Read-out strip resistivity: $\leq 15\Omega/\mathrm{cm}$
- Bias resistor (polysilicon): $1.25\pm0.75\,\mathrm{M}\Omega$
- Coupling capacitance: $\geq 20\,\mathrm{pF/cm}$
- Inter-Strip Capacitance: Capacitance between a strip and its 2 nearest neighbours on both sides $\leq 1.3\,\mathrm{pF/cm}$ at a bias of $150\,\mathrm{V}$
- Depletion Voltage : $\leq 150\,\mathrm{V}$

- Total leakage current (including guard ring), normalised to 20°C: $\leq 6\,\mu$A at 150 V and $\leq 20\,\mu$A at 350 V
- Leakage current stability: current to increase by no more than $2\,\mu$A during 24 hours in dry air at 150 V
- Percentage of good strips: at least 98% per detector and >99% per delivery batch

The motivations of these technical choices are the following.
The strip are capacitively coupled to prevent the flow of the leakage current into the electronics. The strip pitch is dictated by the required spatial resolution of $\approx 20\,\mu$m at the SCT radius. The passivation is intended to protect the detectors from humidity and surface mechanical damage. The sensors should be as thin as possible, in order to minimise the multiple scattering that affects the final track resolution, yet thick enough to present a good signal to noise ratio and a sufficient mechanical robustness. The detector design aims for the lowest possible noise in the readout electronics, which translate into a small inter-strip capacitance (eq. 2.31), a low leakage current (eq. 2.32) and the highest possible value of the bias resistor (eq. 2.33) in order to avoid voltage variations due to the leakage current, still high enough to keep voltage drops to a minimum at the final leakage current values.
The thickness of the capacitive dielectric is chosen to have a coupling capacitance significantly larger than the interstrip capacitance. The implant and aluminium strip dimensions have been chosen experimentally to have a sufficiently low field strenght within the detector to operate without breakdown at 300 V bias after irradiation.
The sensors must have high resistivity to enable full detector depletion.

4.2 "Qualification" of ATLAS prototype detectors

The large part of this doctoral work was performed prior to the order to the manufacturers of the Si detectors for the ATLAS experiment. The aim of this work was to identify which companies were able to produce detectors satisfying the ATLAS specifications.

For this reason, many different tests, agreed within the SCT detector community, were carried out on prototype detectors, in order to evaluate their behaviour in static and dynamic conditions. To simulate the 10 years of LHC operation many prototypes were irradiated using a proton beam provided by the CERN PS. Then, by a special annealing program, the radiation damage of detectors was studied as a function of time and temperature.

The measurements of all the intrinsic and electric parameters part of the specifications that will be presented were explicitly performed for this PhD thesis. A large wealth of data was recorded and only one example for each measurement will be shown. These measurements reproduce the well known behaviour of silicon detectors, and constituted the base to qualify for tendering a Swiss manufacturer, the CSEM company.

In the rest of this chapter, the different measurements performed on non-irradiated detectors will be described and examples of results will be discussed and compared with the theoretical behaviour of the sensor. The same will be done in chapter six for the measurements on irradiated detectors. A final report on the CSEM detectors, taking in consideration all the tests performed to qualify the company, will be given in chapter seven.

4.3 Static Measurements

The quality of silicon detectors is assessed by static measurements that yield information on intrinsic characteristics such as the inter-strip capacitance, the coupling capacitance the strip resistivity and so on.

All the pre-irradiation static measurements were carried out in a probe-station installed inside a metal box that provided electrical shielding and that was equipped with connectors for cabling and a light control. The temperature inside the box was monitored via a PT100 probe. The detector sat onto a metallic chuck in the box and was held in place by vacuum (fig. 4.1). The chuck provided an electrical contact to

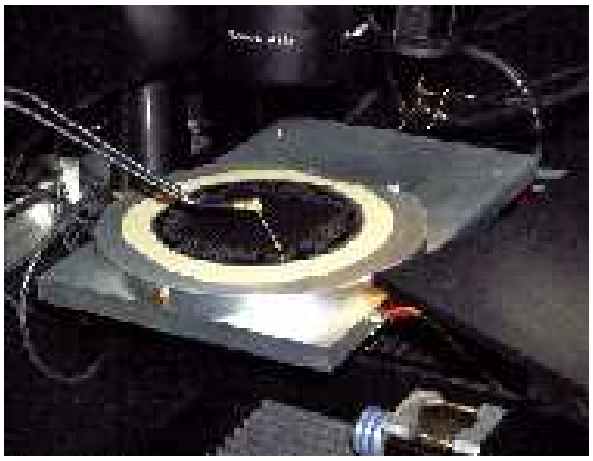

Figure 4.1: A detector on the probe-station chuck.

the backplane of the sensor, while probe needles allowed the contact with the different detector pads. The probing was viewed by a microscope placed over the detector.

A small motor, controlled either manually via a joystick or remotely via software, allowed the movement of the chuck.

Many of the static measurements were automatized: devices such as Keithley 487 Picoammeter/Voltage Source, Keithley 617 electro-meters, Hewlett-Packard 4263B LCR meter, were connected to a computer via a GPIB bus. Dedicated Labview

programs were developed to carry out the measurements and store the data.

4.3.1 Intrinsic characteristics

The intrinsic characteristics of the detectors are measured to check that their value is within specifications, and to monitor the self-consistency of the factory processing.

Aluminium resistivity

This test allows to check whether the aluminium deposited on the p implant is sufficiently thick. Its resistance is measured by placing the probe needles on the pads at the two ends of the metal strip connected with an ohmmeter.

The test was performed on many different detectors yielding results within specifications and varying between 10 and 12 Ω/cm according to the detector production batch.

Bias resistor

The value of the bias resistor is determined by applying a potential difference across the polysilicon and then measuring the current flowing in it.

This test is performed with a voltage source and a volt source/picoammeter as additional equipment to the probe-station. The detector is biased from the backplane and grounded via a needle connected to the bias line. The bias line and one strip implant are then connected to the high and low outputs of the picoammeter in order to measure the current as a function of the voltage. The measurement is repeated on a tenth of the strips, spread on all the detector to check the uniformity of the bias resistor value.

Figure 4.2 shows the results of the measurements of the bias resistor performed on some prototype detectors. The value is almost constant over all the detectors surface and is around 1.5 MΩ. This is whithin the acceptance criteria.

Coupling capacitance

To perform this test the probe needles, connected with the "high" and "low" outputs

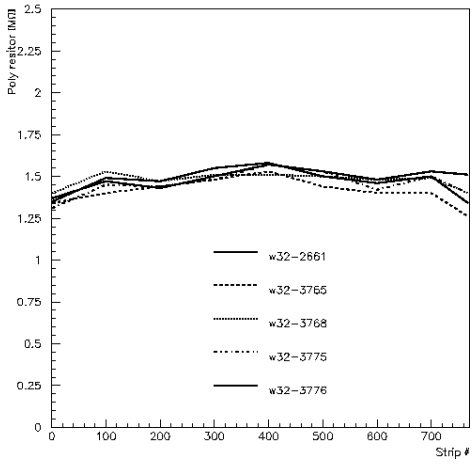

Figure 4.2: Polysilicon resistor value versus strip number.

of a CV meter, have to get in contact with the metal and the implant of a strip.
All measurements performed on different batchs of detectors yielded the value of 22 pF/cm, within specifications.

Inter-Strip capacitance

With this test the capacitance between a strip and its two neigbours is measured. In order to do that, the central strip is connected to the "high" of a CV meter and the two neighbours to the "low" and the detector is biased from the backplane.
The capacity measurement is monitored making use of a dedicated Labview program, that varies the detector bias voltage from 0 V to 500 V and stores the data.
Figure 4.3 shows the typical behavior of the inter-strip capacity as a function of the detector bias voltage: it decreases up to the full depletion of the detector. The value at 150 V for that particular detector is 0.6pF/cm, within the ATLAS specifications.

4.3.2 Current-Voltage Measurements

The total leakage current of a detector can be measured by introducing an ammeter in the bias path of the sensor. Further information on the origin of the measured

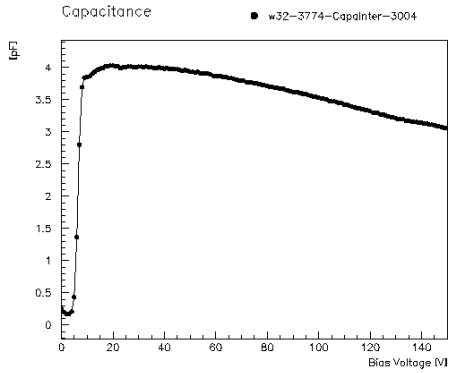

Figure 4.3: Inter-Strip capacity versus bias voltage. Measurement done at 100Hz frequency.

current can be retrieved by measuring at the same time the surface current (guard current).

To determine the dependence of the current on the reverse bias, the voltage is slowly ramped up while measuring the current.

As the leakage current strongly depends on the temperature, this must be kept constant during the test.

Figure 4.4, shows an IV curve for a detector with optimal behaviour. The bulk cur-

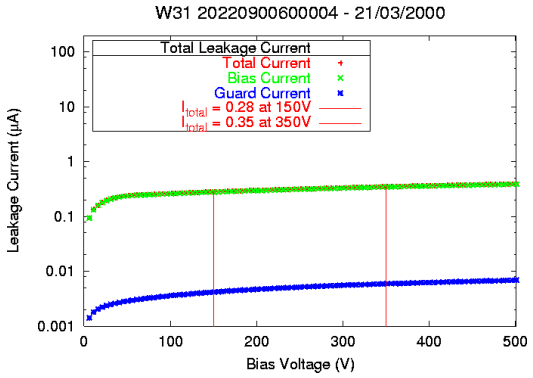

Figure 4.4: Bulk and surface currents in log scale.

rent increases as $\sqrt{V}$ up to the depletion voltage, and then saturates, as expected. The bulk current constitutes the dominant part of the leakage current.

An example of breakdown is shown in Fig 4.5, where the guard current increases

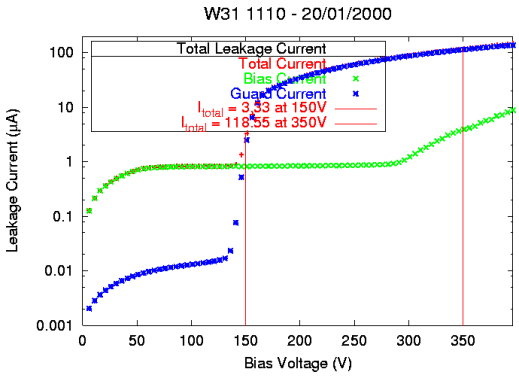

Figure 4.5: Current breakdown.

suddenly from 10 nA to $\sim$20 μA, situating this particular detector outside the ATLAS specifications, given the value of the leakage current at 350 V. This breakdown can be due to high field effects near to surface and it surely does not depend on the substrate, because of the normal shape of the bulk current.

A problem that can occur for some detector, is so called "soft-breakdown". This is a slight increase of the bulk current with a deviation from the $\sqrt{V}$ behaviour (fig. 4.6) and can be due to punctual defect in the n-type substrate.

Current Normalization

Since the generation current is temperature dependent, results of its measurements are normalised to 20°C. The normalisation method relies on the assumption that the leakage current is only composed of the generation current, and that the thermal generation centres are located in the middle of the energy gap [34]. This assumption leads to the equation 2.22 that specify the temperature dependence of the leakage current. From that relation the normalisation of the current I_t measured at t°C to

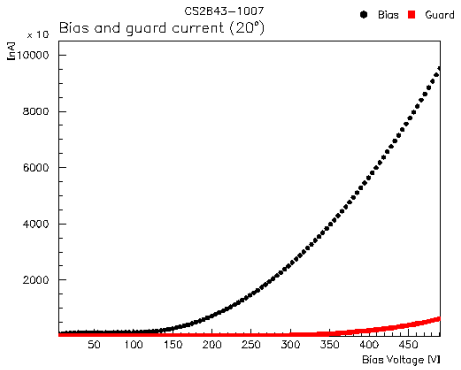

Figure 4.6: Soft breakdown in the bulk current.

the current I_{20} measured at 20^{o}C is:

$$\frac{I_{20}}{I_t} = \left(\frac{293.2}{273.2+t}\right)^{3/2} exp\left[\frac{E}{K}\left(\frac{1}{273.2+t} - \frac{1}{293.2}\right)\right]. \tag{4.1}$$

The accuracy of the temperature measurement is ± 2°C and leads to an uncertainty on the normalisation of $\pm 2\%$.

Current stability

This test is performed with a dedicated Labview program. The detector is biased to the operating voltage while the computer stores the value of current every few minutes allowing the monitoring of the time evolution of the leakage current.

4.3.3 Capacitance-Voltage Measurements

The measurement of the bulk capacitance of a detector allows a determination of its depletion voltage, and is hence of great importance.

The impedance of the detector is measured applying a small AC signal superimposed on the bias voltage. The signal frequency does not influence the CV curve of non-irradiated sensors.

Assuming the detector can be modelled as a capacitor with a resistor in series, the LCR meter calculates internally the capacitance of the device. To couple the bias

source to the "high" path and to protect the LCR meter from the high voltage a bias box is used. It essentially consists of decoupling capacitors and protection diodes. The capacity introduced by cables and by the whole setup is measured and automatically subtracted by the LCR meter, yielding a very high precision on the final value. After correction the device accuracy is ~ 0.5pF at 100Hz.

Figure 4.7 presents the measured value of the inverse square of the capacity $1/C^2$, as

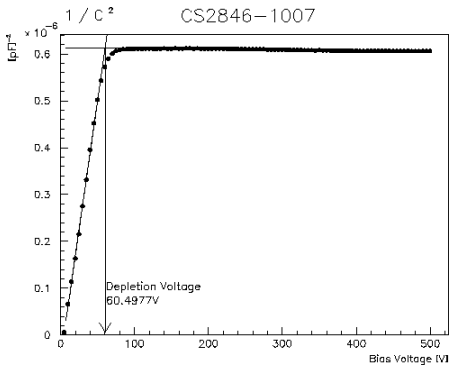

Figure 4.7: $1/C^2$ curve and the fitting procedure to obtain the full depletion voltage.

a function of the bias voltage of the detector. The capacity decreases (or equivalently $1/C^2$ increases) up to the full depletion and then becomes constant as expected from equation 2.20.

The full depletion voltage is determined in our case by the intersection between the line obtained by fitting the rising slope and the extrapolation of the asyntotic capacity. Typical values of depletion voltage for not irradiated detectors are $50 - 70$ V.

4.3.4 Strip integrity

This test allows to identify the presence in a detector of defective strips. These defects are shorts through the dielectric, an interruption of the metal, or shorts to neighbour strips.

The test proceeds by measuring the current and the coupling capacitance on every strip of a sensor. A series resistor is used to limit the current, in the case that a short is found. The detector is automatically moved in order to have contact with the probe needle, held still, with all the strip pads, one strip after the other.
A strip can be defined "defective" due to different reasons:

- A current exceeding 50nA is measured when either 10 V or 100 V are applied between the strip metal and backplane with a 10MΩ series resistance. The defect is defined as a "Pinhole" if observed at 10 V, and an "Oxide-punch-through" if observed at 100 V.

- The measured capacitance indicates a strip metal short to a neighbour or a discontinuity in the strip metal, with the defect defined as a "Short" or "Open", respectively.

Special care is used in operating detectors with defective strips: if a strip with a punch-through is connected to the amplifier to be read out, the potential of this strip is brought down to the level of the electronics, usually few volts. It distorts the field in silicon and makes a region of several strips inactive. One has to disconnect the defective strip from the readout electronics, leaving it at a floating potential.
Figure 4.8 shows the presence of an Oxide-punch-through at strip n^{o}253 of a given detector. The electrical contact between metal and backplane is revealed by the very high current ($\sim \mu$A) in that strip and also by a low value of the coupling capacitance that is the effect of a hole in the dielectric.
To avoid pinholes, manufacturers often use a double layer of dielectric: silicon-nitride over silicon-oxide. The probability that a pinhole in the nitride falls exactly in front of a a pinhole in the oxide is very small.
In the figure 4.9 there is an example of shorts on several strips as shown by the value of the coupling capacitance.

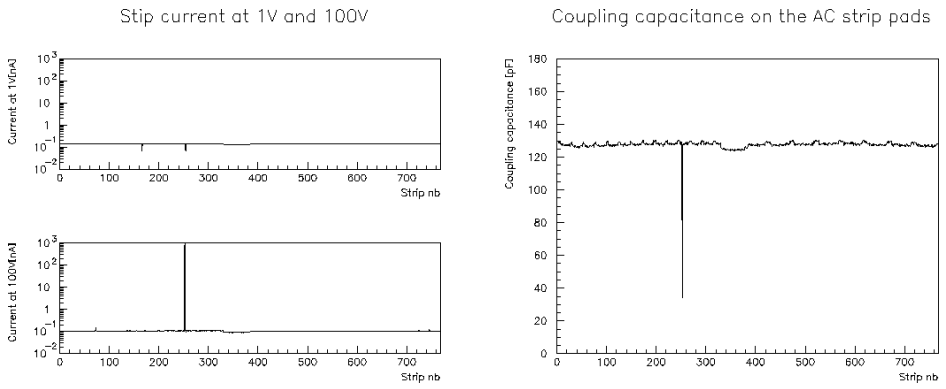

Figure 4.8: Strip integrity test: there is one Oxide punchtroug.

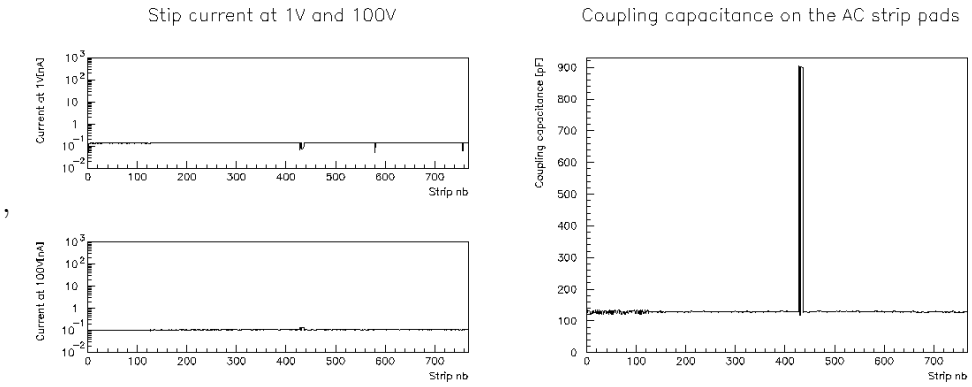

Figure 4.9: Strip integrity test: 7 shorts are present.

Chapter 5

Detector read-out with dedicated electronics

The dynamic behaviour of a prototype silicon detector, *i.e.* its response to traversing particles, is tested connecting it to the readout electronics. In the following sections, a general overview of the challenges and the requirement imposed by the LHC environment to the front-end electronics chips are discussed. The particular analogue chip, the SCT128A, used to perform the readout measurements on silicon detectors is presented. Finally, the last type of measurement foreseen by the detector qualification program *i.e.* the readout, is described.

5.1 Read-out electronics for the ATLAS experiment

The SCT readout electronics is responsible for supplying the hit information coming from 6.5 million strips of silicon detectors to the ATLAS second level trigger and to the data acquisition system [2]. The nature of silicon micro-strip detectors imposes that the front-end electronics must be located very close to the silicon strip electrodes to ensure a low noise operation. The electronics, therefore, must be mounted on the modules themselves. This dictates to the front-end electronics to be of low mass and also of low power consumption to reduce the heating of the detectors.

The LHC operating conditions also present several challenges to the SCT electronics. The LHC bunch-crossing rate will be of 40MHz, and an enormous amount of data will be produced. At this rate, data can not be transmitted nor stored. From the physics point of view, not all the data are interesting and the level 1 trigger will reduce the event rate to ≈100kHz [2]. The time between the bunch-crossing and the level 1 trigger decision will be of 2 μs [35], so the electronics needs to store all the data, produced at 40MHz, for at least the time of the level 1 trigger latency. A crucial part of the read-out chip will therefore be a data storage memory structure (pipeline). After that, the events selected by the level 1 trigger have to be transmitted off-detector. The transmission time is longer than the minimum distance between two "level 1" events (50 ns) and for that reason the electronics chip needs a second storage facility which has to hold the selected events (FIFO). The event transmission will rely on optical links. To reduce the amount of fibers, channels will be multiplexed in time and put out in series. The time slot per channel will be of 25 ns, meeting the transmission speed requirements of the second level trigger which will use the SCT data.
Another important requirement to the electronics imposed by the LHC environment is the radiation hardness. Electronic components have to survive to radiation effects without signicant degradation in performance.
To satisfy all these characteristic, both digital and analog Application Specific Integrated Circuits (ASICs) were designed. The binary readout scheme was chosen as the baseline, while the analog scheme is developed in parallel as a fall-back solution.

5.1.1 The binary readout option

Binary chips do not record the pulse hight information. They consist of a preamplifier-shaper circuit followed by a discriminator which only provides a hit/no-hit information from the strip. Data are then stored in a digital pipeline until the decision of the level 1 trigger. Only the selected events are then optcally transmitted off-detector

(fig. 5.1). Data from non-hit strips are discarded.

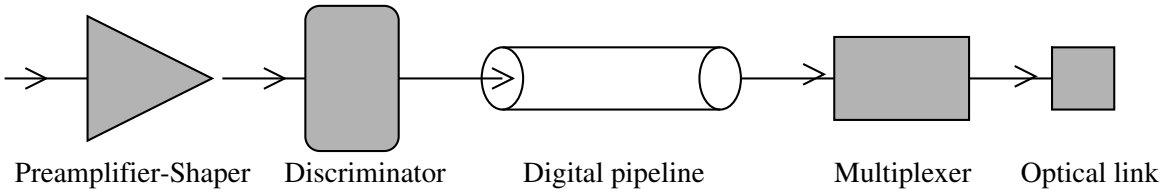

Figure 5.1: Scheme of the bynary readout architecture for one channel.

With this kind of chips, the position resolution is given by the geometrical patterning precision of the silicon detectors.

The efficiency and occupancy are determined by the signal to noise ratio (S/N) of the amplifiers and the threshold uniformity of the discriminators. The binary architecture needs to provide a sufficiently high S/N in order to avoid noise hits and to allow a low discriminator threshold that results into a high efficiency.

The binary readout presents the problem of the common mode noise. This noise can follow from electromagnetic pick-up from power supplies or the connected detector and cannot be subtracted by off-line analysis. Nevertheless, the binary readout has the advantage of a very compact design and a much reduced data transfer rate, since only the data corresponding to hit strips are read out and more chips can use a single optical link.

5.1.2 The analogue readout option

The analog chip has an architecture similar to the digital one, without the discriminator (fig. 5.2). Its main feature is the retention of the hit amplitude information of each channel.

A hit is usually defined when the signal on a strip exceeds a threshold defined in units of the system noise σ. The strip with the highest signal is referred to as the seed strip. The neighbouring strips are then searched for residual parts of the signal. If their

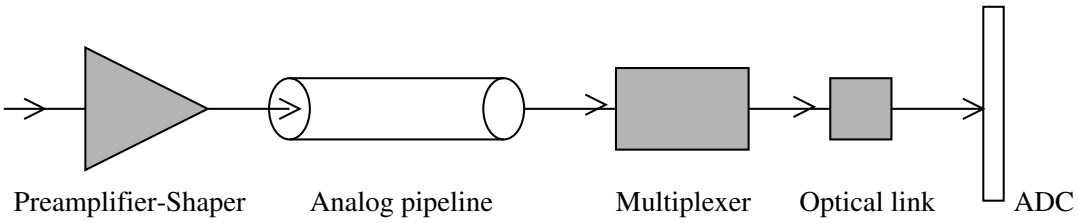

Figure 5.2: Scheme of the analog readout architecture for one channel.

signal exceeds the fixed treshold, they are also included in the cluster. The signals of all channels in a cluster are then added and divided by the sum of the channels noise. This quantity is referred to as the cluster S/N.

Direct access to the pulse height information enables pedestal variations to be corrected in the software. An analog system is robust also to common mode noise which can be easily subtracted in the "off-line". This system allows a continuous monitoring of the detector performance: regions of high leakage current, dead areas or "microdischarges" can promptly be identified, adding reliability to the system. This reliability is traded for a heavier load on data transimssion from the detector over the optical links, both in rate and in the required number and quality of the links.

The use of an analog readout system and a centroid finding alogorithm (reference [36] gives a description of the so called "eta algorithm") permits to improves the detector spatial resolution, since the charge distribution over multiple strips can be used to calculate the location of the particle hit.

5.2 The analog chip SCT128A

The 128-channel analogue front-end chip SCT128A [37] was designed as a back-up solution for the readout of silicon strip detectors employed in the inner tracking detectors of the LHC experiments. It has been however used for the characterisation of the detectors as it allow to collect more information than the bynary chip.

The chip comprises five basic blocks: a frontend amplifier, an analogue pipeline, a control logic for the pipeline including a derandomizing FIFO buffer, a command decoder and finally an output multiplexer. The front-end is based on a fast transimpedence amplifier, followed by an integrator providing a semi-gaussian shaping with a peaking time of 25 ns, and an output buffer. The peak values are sampled at 40 MHz rate and stored in the 128-cell deep pipeline. The readout sequence is initiated by a level 1 trigger transmitted through the command lines in coded format. Once a trigger signal arrives, the pointed physical address of the 128-channel memory column containing the sampled analogue values is stored in a derandomising FIFO and, at the start of the readout sequence, the data are sent to the analog multiplexer. This latter produces a serial data stream and builds the data packet. The chip includes a calibration and a bias circuit.

Figure 5.3 shows the layout of the SCT128A chip. The front-end channels and the

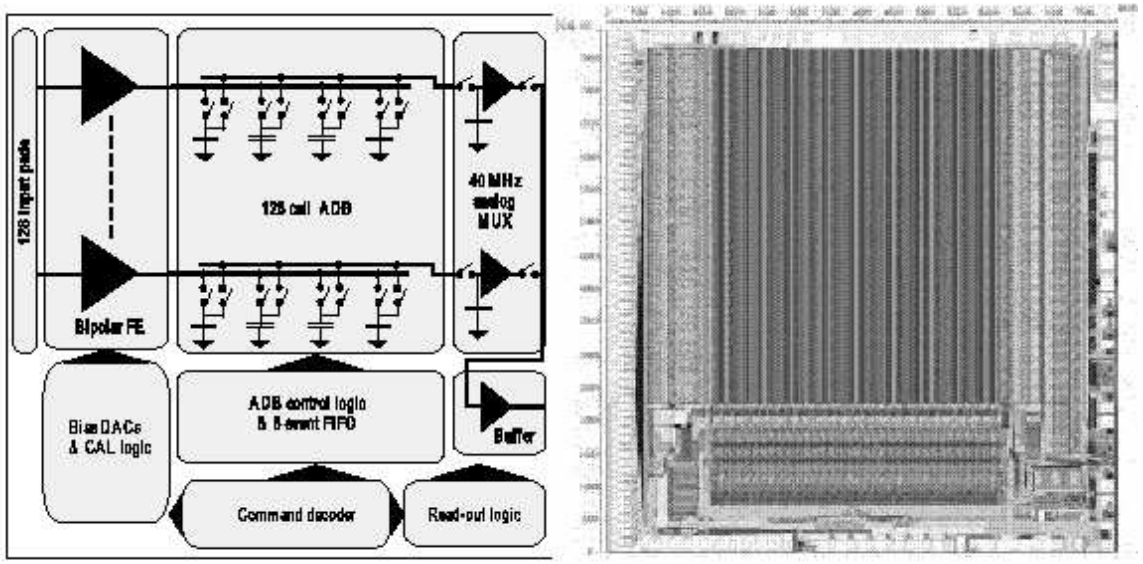

Figure 5.3: Layout of the SCT128A chip.

analogue pipeline are laid out with a pitch of 42 μm, while input bonding pads are

laid out with 60 μm pitch. The bond pads for supply voltages and control signals are located on both sides of the chip. The die area is 7.9×8.0 mm.

5.3 The setup for the readout of silicon microstrip detectors with the SCT128A chip

A dedicated setup has been used to test the response of prototypes silicon detectors to traversing minimum ionising particles (mips).

The chip is mounted on a printed circuit board (PCB) containing the power supplies, the amplifiers and all the necessary connectors to carry control and data signal to and from the chip. 128 channels of the silicon detector under test are bonded to the chip by the help of special glass pitch adapters that allow to use the same chip many times. The detector under measurement is biased to a voltage greater than its full depletion voltage. The PCB with the chip and the detector is located into a metal box acting both as protection and support. This box has an hole on the vertical of the detector where the radioactive source takes place.

This source is ^{106}Ru. It decays to ^{106}Rh that emits β particles with maximum energy of 3.541 ± 0.006 MeV and mean energy of about 1.45 MeV. These electrons can be considered as mips. Figure 5.4 shows that the particles emitted can cross 300μm of silicon and hence reach a scintillator placed under the detector. The scintillator is read by a photomultiplier and provides a syncronous trigger for the β particles.

When an electron crosses the silicon detector, it creates a signal charge in the bulk that is collected on the strips. The electron is not absorbed in silicon and also yields a pulse in the photomultiplier. This pulse is converted into a NIM trigger pulse and is sent to the command generator, an unit that communicates with the readout chip via the serial command interface and also produces the main 40 MHz clock. The pulse from the scintillator is encoded into the level 1 trigger command by the command generator and is sent to the chip.

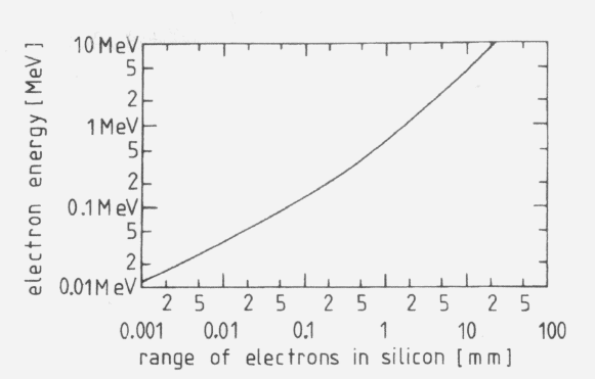

Figure 5.4: Range of electrons in Silicon.

The SCT128A starts the readout sequence upon the reception of the trigger; it multiplexes out a data packet (figure 5.5), which is sent to a fast Analog/Digital converter

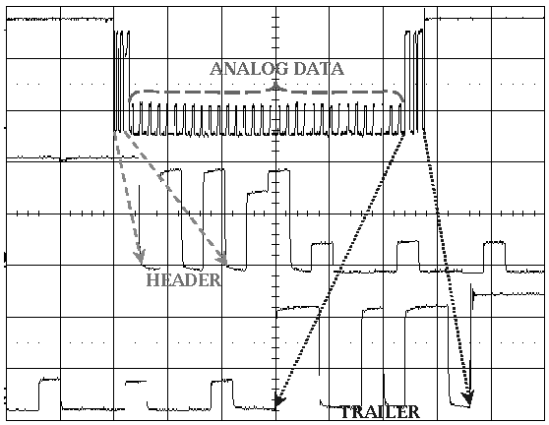

Figure 5.5: View on the oscilloscope of a SCT128A data packet.

and then stored on disk via a VME bus interface.

The software communicates with the chip via the command generator. It allows to run the system with the described trigger ("external trigger") or generating internal pulses of different amplitudes ("internal trigger").

The internal trigger modality allows to test the chip functionality indepedently from

the detector, as described in the following section.

5.4 Chip performance test

Before performing the actual detector readout measurement, it is useful to check the chip behaviour to validate the gain and the noise performance and to identify the bad channels.

This test is performed without the detector and radioactive source, running the chip in the internal trigger mode. The SCT128A internal calibration circuit applies test pulses of variable amplitude (that can be set via software) to the on-chip test capacitors at the input of every channel. By changing the amplitude of the calibration pulses, it is possible to perform a gain scan of the chip under test. The design gain of the SCT128A is around 25 mV/fC [38].

Figure 5.6 presents the results of a chip performance test carried out on a SCT128A before its use to readout silicon detectors: the first two plots show the gain distribution over the 128 chip channels. In the second plot it is visible one low-gain channel (the number 38) that can be excluded via software in the analysis of the following measurements. The third plot shows the distribution over the channels of the electronic noise expressed in number of electrons. Three noisy channels are present, one of them corresponding to the low gain channel discussed above. Again the data coming from these channels will be software excluded in the further readout measurements. The mean noise for the other channels is around 850 electrons. The last plot presents the gain linearity measured for one channel. The average gain is around 25.5 mV/fC and the linearity is kept up to 12fC, which is enough for tracking applications [38].

5.5 Dynamic measurements

The readout of the silicon detector is carried out using the setup with the radioactive source described in section 4.3, triggering on the signal coming from the photomulti-

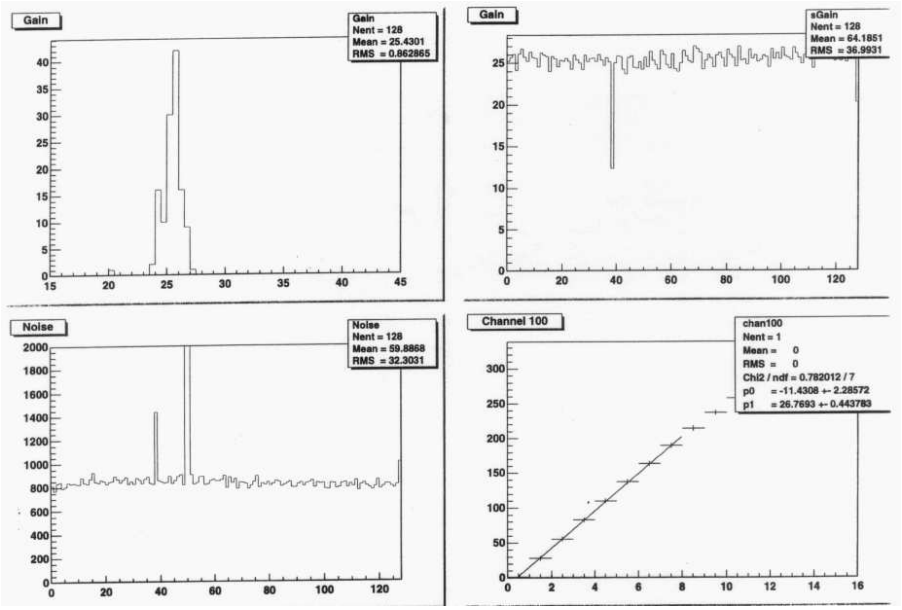

Figure 5.6: Chip performance test. The upper left plot represents the gain distribution in unit of mV/fC; the upper right plot shows the gain, in mV/fC, over the 128 channels. The lower left figure shows the noise, in number of electrons, for all the channels, while the last one shows the gain of the channel 100 versus the test pulse height.

plier.

This measurement allows to check the signal given by the silicon sensor in detecting particles, to compute the S/N ratio, and to identify bad or too noisy channels.

After the data taking, the analysis starts with the computation of pedestal levels for the 128 channels. Then, a search for clusters of hit strips is performed according to the following criteria:

- the S/N of the seed strip is at least four
- neighbouring strips are added to the cluster, provided the S/N value is at least two
- a S/N ratio of at least six is required for the complete cluster

The analysis program perfom the common mode noise subtraction.

In the left part of figure 5.7 is shown the signal distribution measured for a 300μm

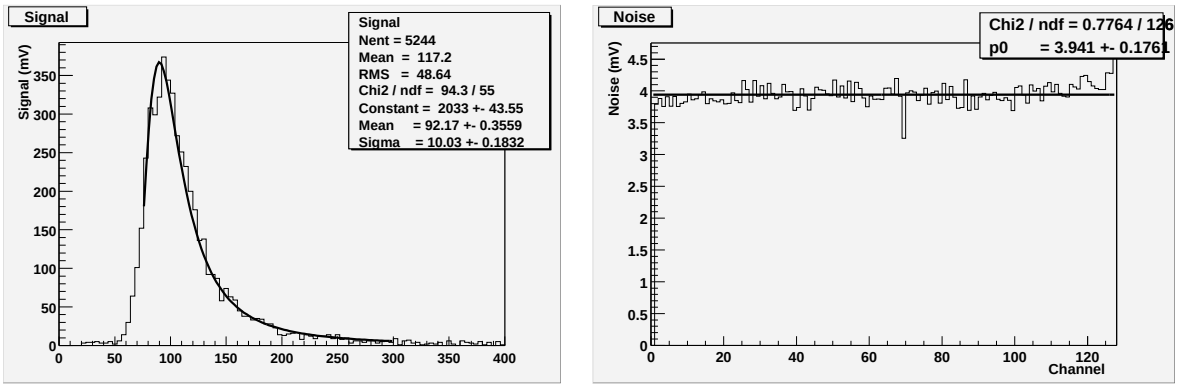

Figure 5.7: Signal distribution (left) and noise spread over the channels (right), measured with a ^{106}Ru source.

thick ATLAS prototype detector. The signal follows a Landau curve as expected, and its most probable value is 92 mV. The measurement was performed with a detector bias voltage of 120 V.

The right plot of the same figure gives the noise level for the 128 channels during the same measurement. The noise is almost constant and its value is around 3.9mV: this detector has no bad channels. This check verifies wether the sensor meets the ATLAS specifications on the percentage of good strips *i.e.* more than 98% of good strips per detector and more than 99% per delivery batch.

The cluster S/N distribution, shown in figure 5.8 follows from those data. For the detector under measurement this value was around 25.

Assuming that a MIP produces in silicon 22500 electron-hole pairs and that the peak of the Landau distribution corresponds to this number, the equivalent noise charge is then 897 electrons. This value is in good agreement with the ENC calculated using the formula 2.33. This amounts to 870 electrons out of wich the main contribution is given by the input channel noise (866e) while the noise coming from the leakage current is 29e and from the bias resistor is 69e.

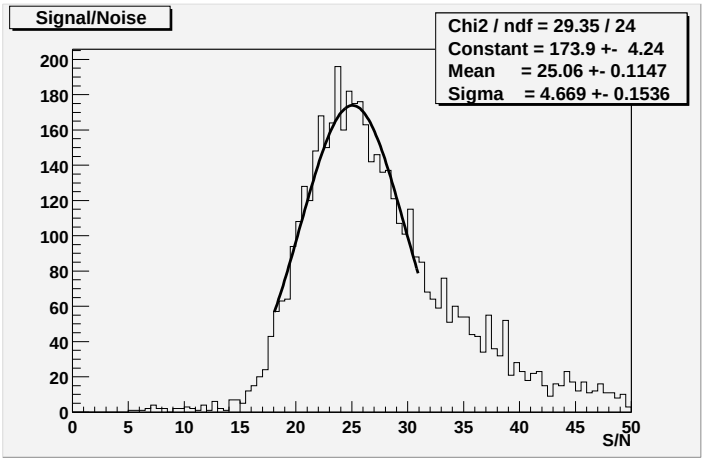

Figure 5.8: Cluster S/N distribution.

It is interesting to perform the readout measurement for different detector bias voltages. In figure 5.9 are shown the plots of the signal, noise and S/N as a function of the detector bias voltage. The signal increases with the bias voltage until it reaches a "plateau" at around 105 V, what corresponds to an overdepletion of ≈35 V since the full depletion voltage obtained by fitting the CV curve is 70 V. The dependence of noise on voltage is quite weack, thus having only a small influence on the S/N behaviour.

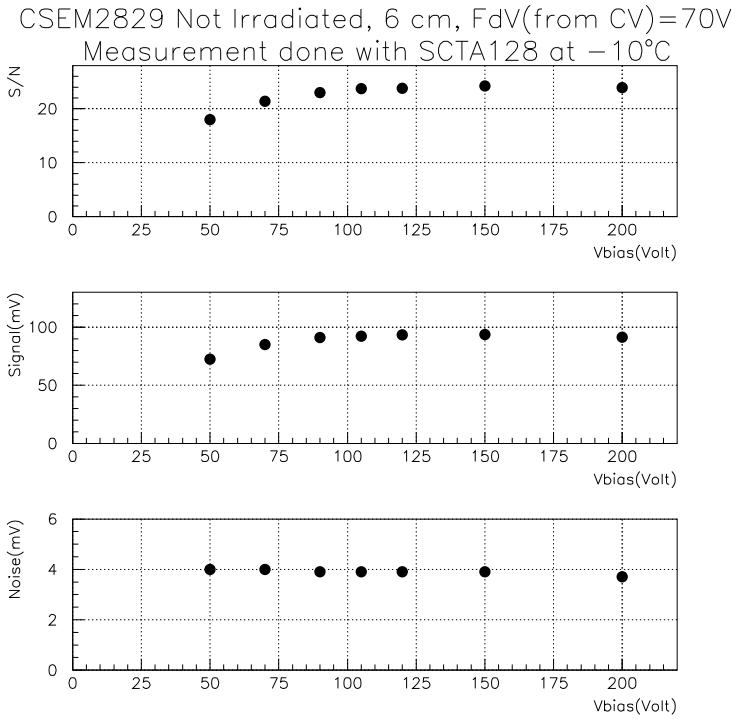

Figure 5.9: Signal, noise and S/N as a function of the detector bias voltage.

Chapter 6

Irradiation program of Atlas silicon detectors

In this chapter an important part of this thesis work is exposed: the measurements carried out on irradiated detectors to investigate the damage induced by radiation and to verify whether the sensors satisfy the ATLAS post-irradiation specifications.

6.1 The ATLAS operating environment and the irradiation and annealing program

As pointed out in chapter 3, the effect of the operating and storage temperature of the silicon sensors strongly affects their performance. To minimise the increase of the reverse current and of the depletion voltage due to radiation, the temperature should be kept as low as reasonably possible. For that reason, it is foreseen to operate the SCT at -7°C. Nevertheless, periods of maintenance, during which the detector will be warmed up, will be unavoidable during the ten years of foreseen LHC operation. The SCT TDR [2] assumed a yearly maintenance scenario of two days at 20°C, and two weeks at 17°C.

The effect of these maintenance periods must be studied to understand their implications on the detector characteristics. It is possible to perform this study in a short time scale by irradiating prototype detectors up to the maximum expected fluence

Ten years with	45 days at 20°C
TDR scenario are	21 days at 25°C
equivalent to :	10 days at 30°C

Table 6.1: Warm up times assuming the ten years scenario proposed in the ATLAS inner detector TDR [2].

over the full LHC operating period and then simulating the effect of the warm up over ten years operation time using a radiation damage model. The Ziock parametrisation is used as the time constants are directly expressed as a function of temperature.
The same amount of annealing as achieved in ten years with the described scenario can be reached by annealing the irradiated detectors at an higher temperature for a shorter time, as summarised in table 6.1.

Post-irradiation specifications have been established by the ATLAS SCT collaboration [39] to ensure a satisfactory performance of the irradiated detectors. The main ones are reported below assuming an annealing period of 7 days at 25°C:

- Strip resistivity, Al Read-out strip resistivity, bias resistor (polysilicon) and coupling capacitance: to remain within their pre-irradiation acceptance limits
- Inter-Strip Capacitance: Capacitance between a strip and its 2 nearest neighbours on both sides $\leq 1.5\,\mathrm{pF/cm}$ at a bias of 350 V, measuring at 100 kHz
- Total leakage current (including the guard rings), $< 0.5\,\mathrm{mA}$ at -10°C and 350 V bias
- Leakage current stability: current to increase by no more than 3% during 24 hours at -10°C and at 350 V
- Percentage of good strips: as for the pre-irradiation acceptance at 350 V bias.
- Maximum operating voltage required for >90% of maximum achievable charge

collection efficiency: 350 V (after connection to readout electronics with effective peaking time of 25 ns)

6.2 Irradiation conditions

In order to study the radiation damage and its annealing, many tens of ATLAS prototype detectors have been irradiated with a 24 GeV proton beam coming from the CERN PS accelerator. The total fluence received is 3×10^{14}p/cm^2, which corresponds to the foreseen total fluence after ten years of LHC operation plus a safety factor. The fluence was determined from activation measurements of aluminium foils.

To be irradiated, detectors were mounted on ceramics boards and the read-out strips were bonded to the pitch adapter. They were then inserted into a special box where cold nitrogen could circulate in order to keep the temperature around -7°C. During the irradiation, the detectors were biased to 100 V and the strips grounded in order to keep them at the same potential and to simulate the condition of being bonded to readout electronics. The box was scanned through the proton beam to ensure uniform irradiation across the whole detector area.

The reverse current was continuously monitored during the irradiation. It is found to increase with the fluence, as predicted in equation 3.1. Figure 6.1 shows the reverse current for one of the irradiated sensors.

After irradiation the detectors were stored at around -10°C, and protected against moisture. Few days of storage are waited in order to decrease their activity.

6.3 Static measurements and results

All the measurements performed on the irradiated sensors are done at low temperature, in order to avoid current breakdown and the consequent destruction of the detector. This is particularly important since after irradiation the current can increase of orders of magnitude.

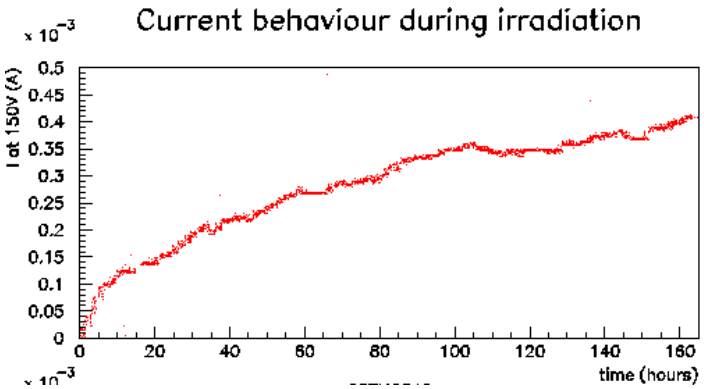

Figure 6.1: Reverse current during irradiation for a 300 μm detector.

The static measurements are performed in a climate cabinet, allowing a temperature and humidity control, and in which nitrogen can circulate. This is the only difference with respect to the measurement procedure adopted for not irradiated sensors.

6.3.1 Reverse current

Figure 6.2 shows the IV characteristics for a 300μm thick detector measured before and immediately after its irradiation. The current still has the $\sqrt{(V)}$ behaviour but

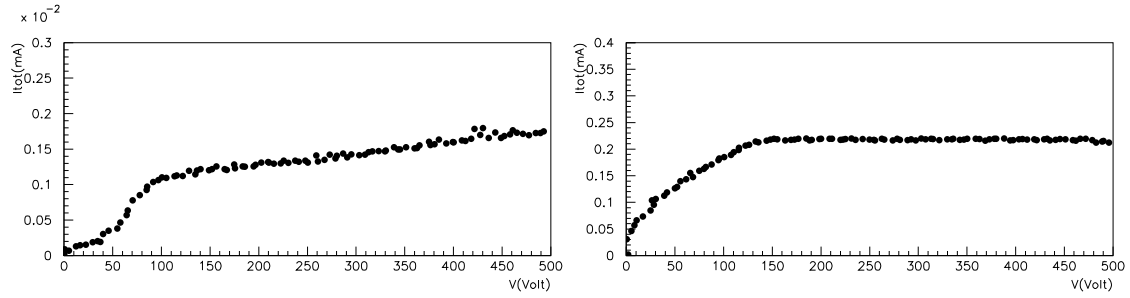

Figure 6.2: IV characteristics for a sensor before and immediately after its irradiation. The measurement were performed at 20°C and -18°C respectively. A difference of two orders of magnitude is observed.

increases after irradiation due to defects created in the bulk region. In detail, the

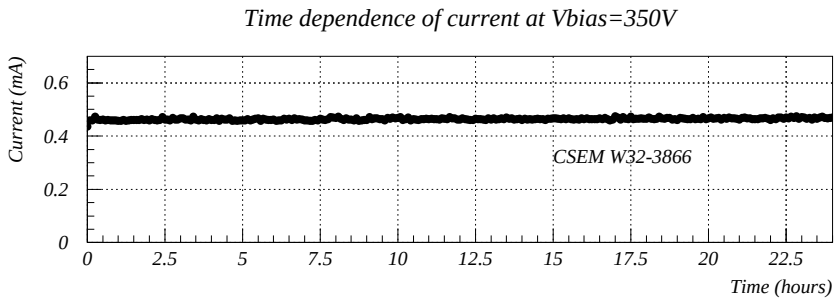

Figure 6.3: Leakage current as a function of time. Measurement performed at -10°C.

current observed before irradiation at 350 V was 1.4μA while the value observed after irradiation at the same bias and at -18°C is 0.2 mA.

To check whether the reverse current had an acceptable value, i.e. it was within the specifications, the same measurement was performed after 7 days of annealing at 25°C. The value found was 0.54, slightly too high to accept that detector for use in ATLAS.

The current stability in time was also checked, and an example of a 24 hours long measurement performed biasing one detector at 350 V is shown in figure 6.3: this detector has a very stable behaviour. Its current is 0.45 mA and is well within specifications.

For some detectors an improvement on the IV characteristic was also observed when they were left under bias for some hours. In the figure 6.4 the recovery of a detector showing soft breakdown before stabilisation is evident.

Further measurements have been performed to verify the temperature dependence of the leakage current: an example is shown in the figure 6.5 and the expected exponential dependence is confirmed.

From the Arrenius fit it is possible to extract the value of the silicon energy gap. The value found for that particular detector is $E_g = 1.07 \pm 3$ eV, which is in good agree-

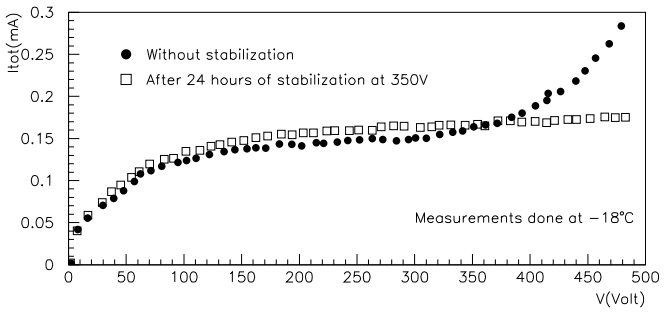

Figure 6.4: IV curve obtained for the same irradiated detector before and after one day biasing at 350 V.

ment whit the accepted 1.12 eV value. This result validates both the model which describes the current and the measurement method in the climate cabinet.

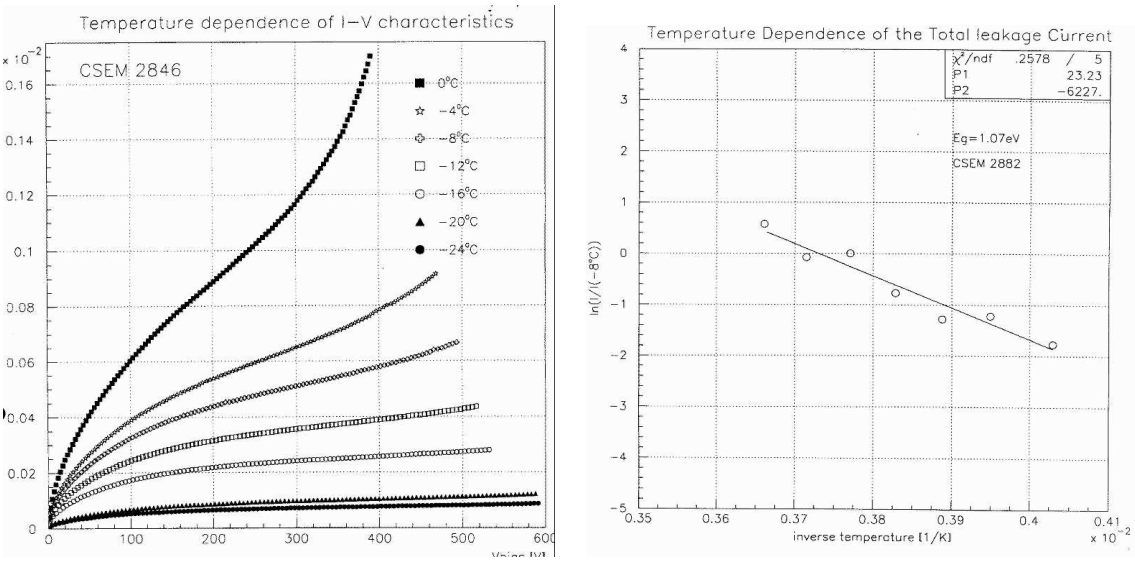

Figure 6.5: IV characteristics at various temperatures (left) and Arrenius plot (right) for a 300μm thick ATLAS prototype detector.

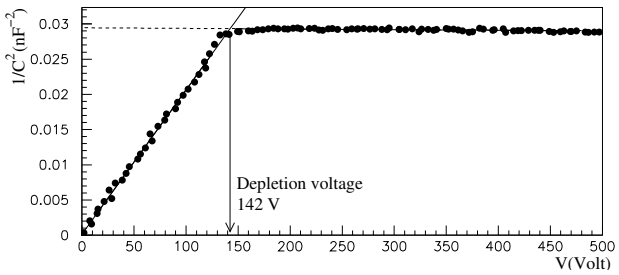

Figure 6.6: CV measurement at 100 Hz and -18°C on an irradiated detector.

6.3.2 Bulk capacitance and depletion voltage

After irradiation, the CV characteristics becomes strongly frequency dependent indicating the influence of defects in the bulk and in the oxide. The effect has been studied in reference [40] where it was observed that at low frequency the detector capacitance still behaves as C$\propto V^{-1/2}$. For this reason, all the CV measurement done on ATLAS prototype detector have been carried out at 100 Hz.

An example of CV characteristic of an irradiated detector, measured at -18°C, is presented in the plot 11.20. A high depletion voltage is found when compared to the value for not irradiated detectors (≈ 65 V) .

The temperature dependence of CV characteristics, and hence of the full depletion voltage of the sensors, has also been studied: a slight increasing of the depletion voltage with temperature was observed. This result is presented in the figure 6.7.

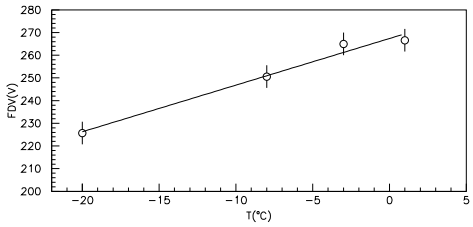

Figure 6.7: Temperature dependence of the depletion voltage of an irradiated sensor.

6.4 Annealing cycle and results

To study the time evolution of the radiation damage, annealing cycles have been followed. Cycles of 21 days at 25°C were followed to simulate the warm up of the silicon detectors over the ten years of LHC operation.

Measurements of current and capacitance were carried out at -10° after approximately every 24 hours annealing at 25°. This method allows to follow carefully the time evolution of the current and the capacitance.

The behaviour of the leakage current as a function of the annealing time is presented in figure 6.8 for few detectors where the value of the reverse current at 350 V bias is chosen. The current decreases exponentially as anticipated in the precedent chapter. It starts at around 1.15 mA immediately after irradiation and decreases up to around 0.52 mA after one month of annealing.

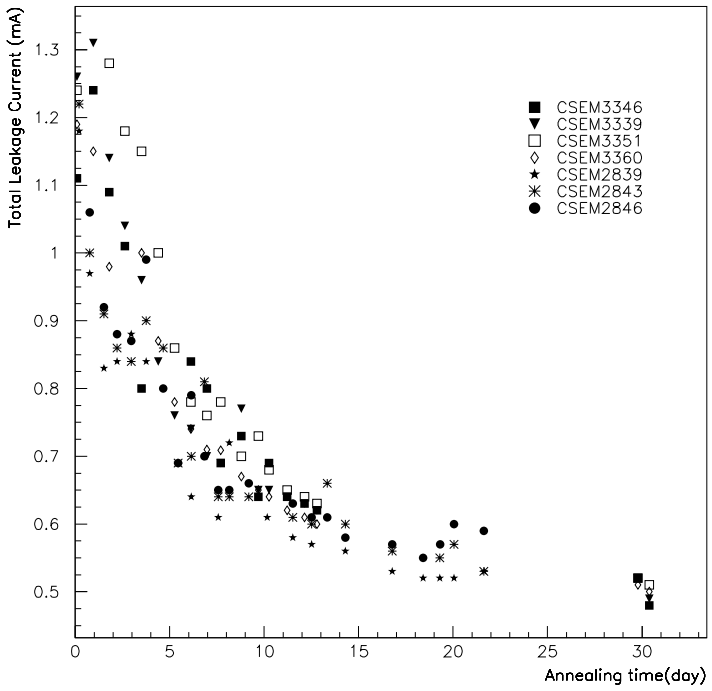

Figure 6.8: Evolution of the leakage current measured at 350 V bias and -10°C.

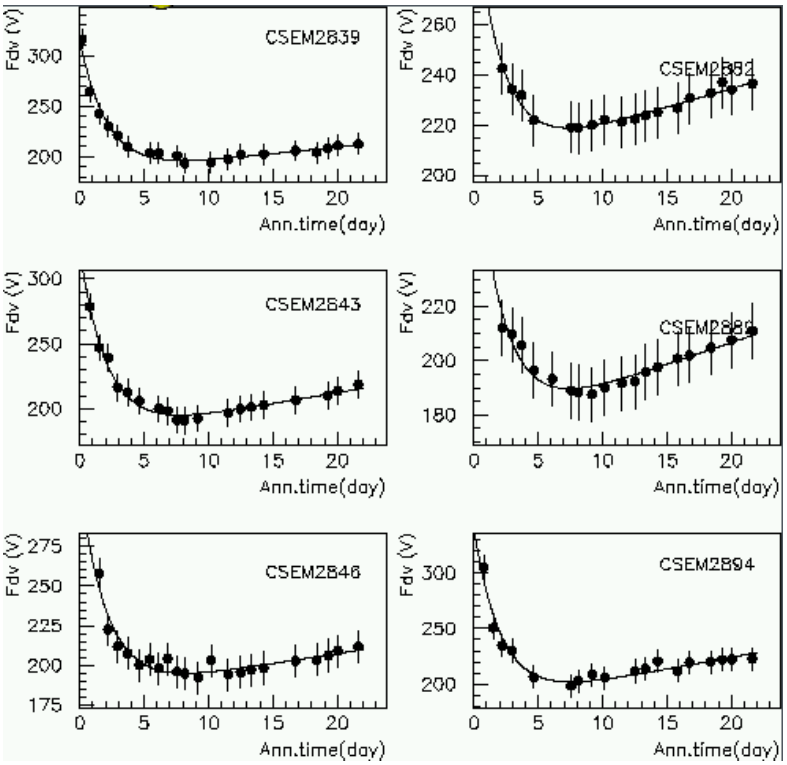

Figure 6.9: Full depletion voltage as a function of the annealing (at 25°C) time.

The annealing of the full depletion voltage for few detectors is presented in figure 6.9. It is clearly visible the first period, of beneficial annealing, during which the depletion voltage falls from around 300 V immediately after the exposure, to a minimum of around 190 V corresponding to approximately 7 days of annealing. Then, the reverse annealing starts and the depletion voltage increases again with time to reach a value of around 230 V at the end of the annealing period. This voltage, plus some over-depletion needed to have a fast charge collection, is an indication of the bias voltage that should be applied to the sensors in the last period of LHC operation.
Is superimposed to the time evolution of figure 6.9 a fit curve, obtained using the Ziock model. A linear approximation has been used to parametrise the reverse annealing due to the restricted time interval covered by the data. The function reproduces well

Detector	$\nu_z \times 10^{-12}\,\mathrm{Vcm}^2$	$\nu_s \times 10^{-12}\,\mathrm{Vcm}^2$	$\nu_a \times 10^{-12}\,\mathrm{Vcm}^2$	τ_s days
2839	0.61	0.44	0.9	2.1
2843	0.59	0.48	1.1	2.1
2846	0.60	0.44	0.9	2.1
2889	0.58	0.40	1.1	2.1
3346	0.62	0.43	1.5	2.0
3351	0.62	0.40	1.3	1.7
Ziock	1.06	1.34	3.8	0.88

Table 6.2: Results obtained by fitting the experimental data with the Ziock parametrisation function.

the behaviour of the experimental data. The fit parameters obtained for a set of irradiated sensors are reported in table 6.2.

Compared to the Ziock results, the damage constants obtained are smaller, indicating a better quality of the detector set.

6.5 Charge collection efficiency

Readout measurements with the SCTA128 setup have been carried out on many irradiated detectors. Again, because of the high leakage current, the measurements were done at low temperatures, storing the box containing the PCB with the detector and the scintillator in a fridge.

Two different strip lengths have been studied: 6 cm and 12 cm. This latter was studied because the ATLAS module is composed by two 6 cm strips silicon detectors connected together. Anyway, to perform the readout measurements, the strips of the same detector are connected two by two using the pitch adapter.

As an example, figure 6.10, shows the signal, noise, and S/N distribution obtained for an irradiated detector biased at 350 V, and hence already over-depleted. The S/N peaks at 14.7, to be compared to values around 25 for not irradiated sensors. The large difference between these value is due both to the trapping effect of the deep lev-

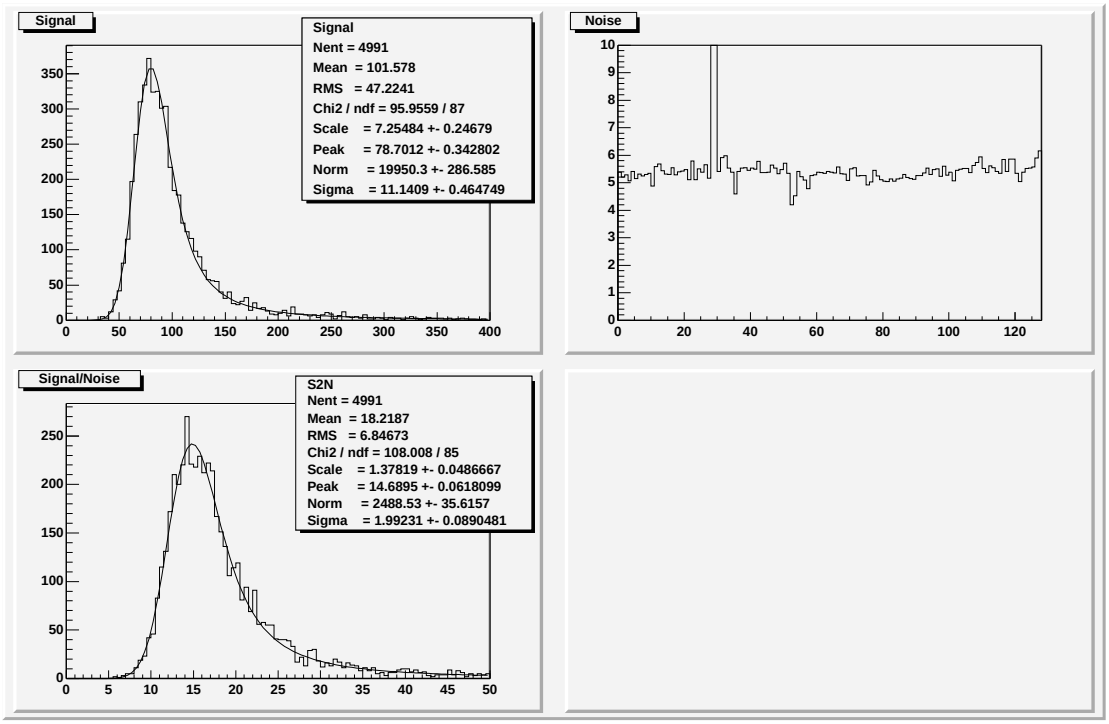

Figure 6.10: Signal, S/N and noise distribution at 350 V bias.

els created by the irradiation and to an increase of noise coming from the increased leakage current and interstrip capacity.

The noise distribution is quite flat, showing good post irradiation strip readout quality, with the exception of two very noisy strips.

To verify whether the sensors satisfy the ATLAS post-irradiation specifications, on the maximum operating voltage for the complete charge collection, the signal collection has been studied as a function of the bias voltage.The figure 6.11. shows that, for the given detector under study, the plateau for the signal starts at around 300 V, satisfying the specification requirement of a bias voltage <350 V.

The charge collection efficiency for irradiated sensors has been computed normalising the number of electrons collected with an irradiated detector biased at 350V, to the number of electrons collected with a not irradiated detector on the "plateau". Typical

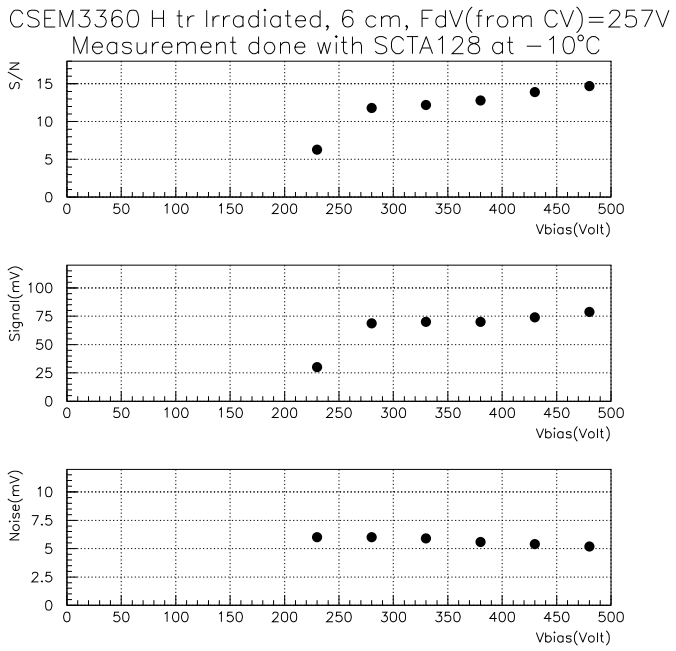

Figure 6.11: Signal, S/N, and noise as a function of the dectector bias voltage.

efficiencies obtained for irradiated sensors with 6 cm strips and using the SCT128A chip are around 0.8.

6.6 Strip integrity

This measurement is performed to check whether additional oxide punch-through are created by irradiation. As the test is performed in a probe-station without temperature control, the measurement is done at room temperature and consequently the detector is biased to a maximum of 10 V. The figure 6.12 shows the result of the strip integrity check performed on the same detector before and after its irradiation. The high value of the current on seven strips only in the post-irradiation test indicates that seven pin-holes have been created. Nevertheless, the detector passes the accep-

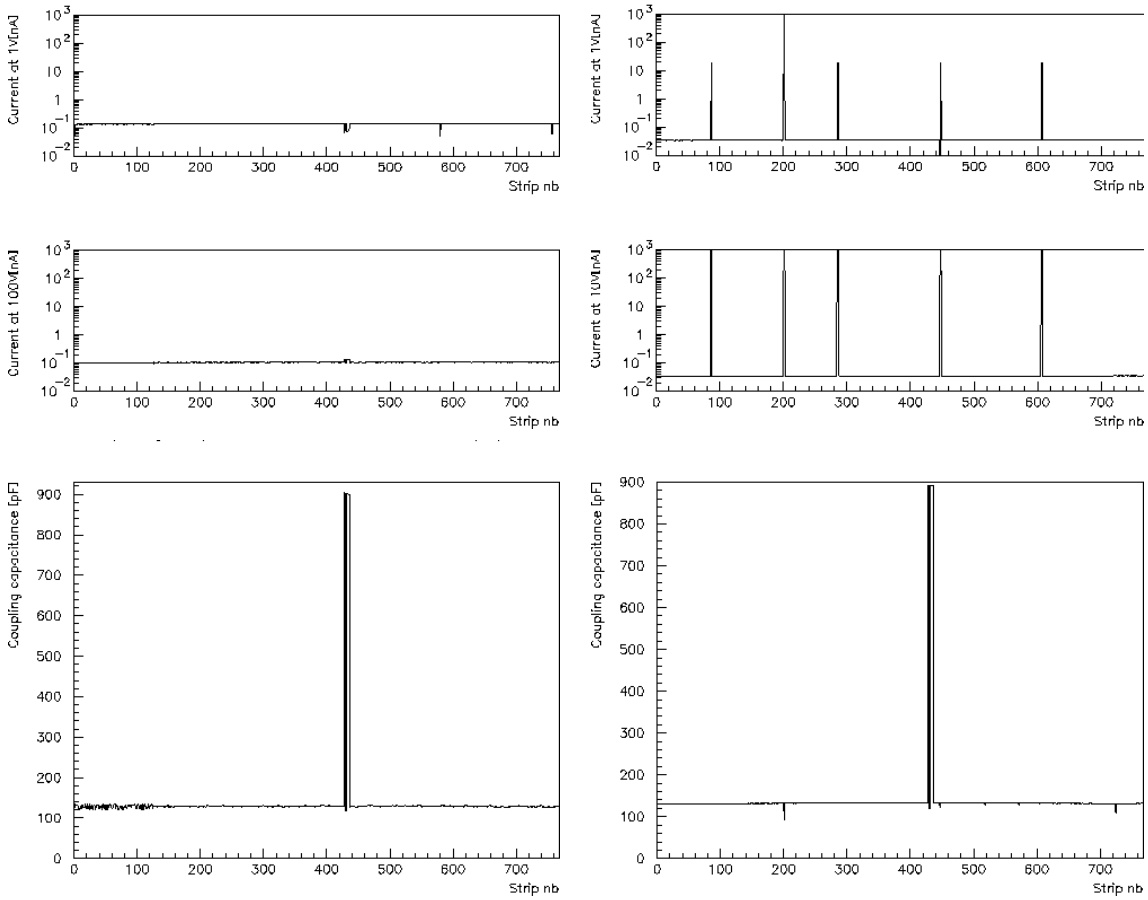

Figure 6.12: Strip integrity test. Left plots refer to before irradiation while the right ones refer to after irradiation.

tance requirement of the ATLAS specification since the percentage of the defective strips is less than 2%.

Chapter 7

Qualification measurements for CSEM detectors and comparison with Hamamatsu

The majority of the ATLAS prototype detectors studied during this thesis work was produced by the Swiss manufacturer CSEM. The tests performed on those sensors were motivated by the need of verifying the quality of the produced sensors and, on the base of the results obtained in both pre and post-irradiation measurements, asses whether the company is qualified for tendering.

7.1 Summary of the measurements and results for CSEM detectors qualification

The test measurements on CSEM detectors have been performed in a period starting from the spring 1998 till the autumn 1999, when the deadline for the qualification of the manufacturers was fixed. During that time, CSEM delivered different batches of detectors, summarised in the table 7.1.

A subset of the delivered batches was irradiated and then studied.

All the measurements performed on CSEM prototype detectors and used to take the decision about the CSEM qualification are described in References [41] and [42].

Detector type	Delivered sensors	Delivery date	Irradiated sensors	Irradiation date
Barrel	7	Spring 98	-	-
Barrel	17	Spring 98	6	Jul98
Barrel	5	Aug98	2	Nov98
Barrel/Htreat	13	Oct98	2	Nov98
W32	23	Jan99	5	Apr99
W32	28	Jun99	3	Jul99
W32	8	Oct99	-	-
W32	6	Dec99	-	-
W31	4	Jun99	-	-
W31	17	Nov99	-	-
W31	17	Dec99	-	-

Table 7.1: CSEM detectors received by the Geneva University and tested for the manufacturer qualification.

Tables 7.5 and 7.6 summarise the type of test performed both before and after irradiation, with an evaluation of the results according to the ATLAS specifications.

Over the year and half of the test period, an intensive interaction with the manufacturer took place and, accordingly with the results of the tests performed, the production process was changed various times, to improve the sensor quality and to meet the specs.

After the first batches of barrel detectors, the CSEM sensors had intrinsic characteristics and depletion voltage in specs. The histogram 7.1 shows the full depletion voltage distribution of wedge sensors not irradiated. The mean value is 70 V, and all the sensors meet the specification value of a depletion voltage below 150 V.

A problem often encountered before irradiation was the leakage current soft breakdown, i.e. a linear increase of the current with the bias voltage that put the sensor outside the pre-irradiation acceptance requirements. The soft breakdown was understood as being due to isolated defects in part due to dust introduced at the time of the n^+ implantation. Under these conditions, one or more strips opposite the defect

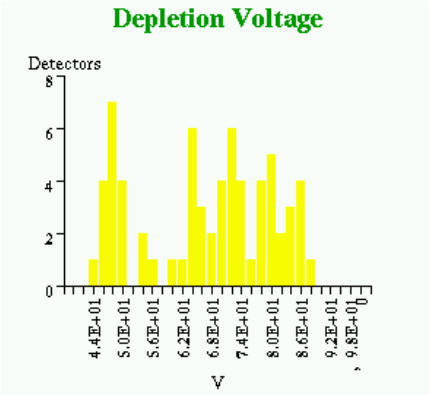

Figure 7.1: Full depletion voltage distribution of CSEM not-irradiated sensors.

will draw a relatively high current after the depletion voltage is reached.

The measured values of leakage current at 150 V and 350 V bias of a CSEM detectors set are reported in figure 7.2. The mean values are around 7μA and 49μA respectly to be compared to the specification values of <6μA and < 20μA. A large fraction of the sensors is outside of the specifications.

The soft breakdown problem was completely hidden by the current increase due to

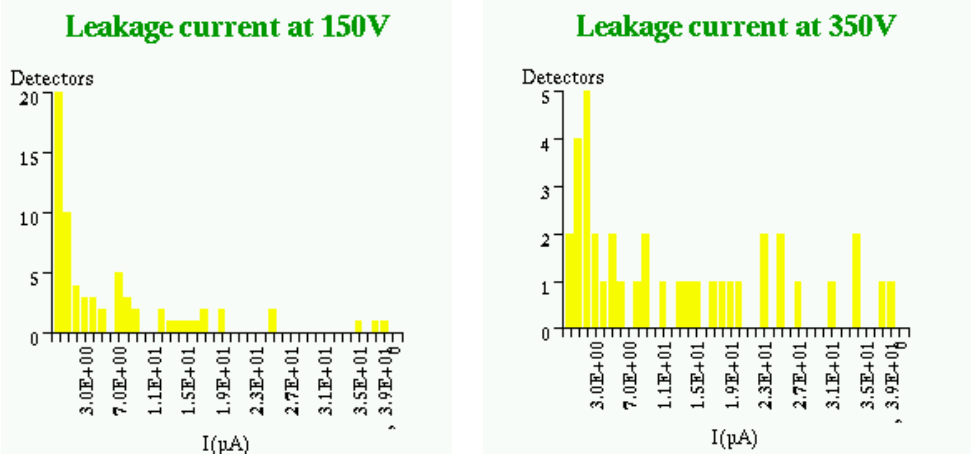

Figure 7.2: Leakage current value distribution for a set of not irradiated CSEM sensors biased at 150 V (left) and 350 V(right).

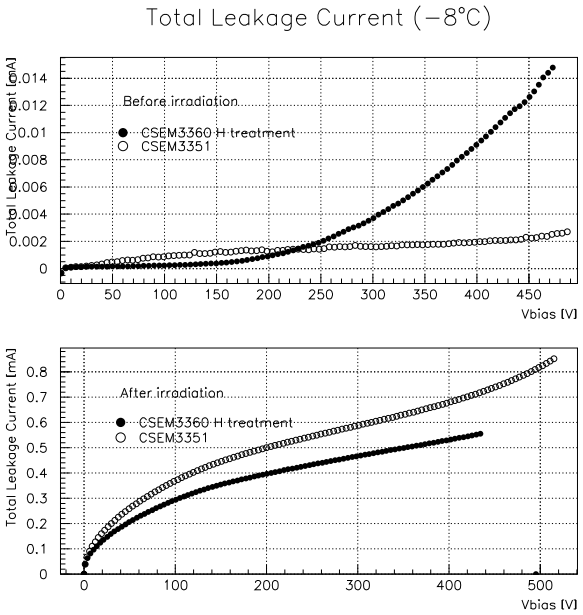

Figure 7.3: IV curve of two CSEM detectors before and after their irradiation. The sensor with full dots did not meet specifications before irradiation but met them afterwards.

bulk damage following irradiation. This implied that a detector outside the specifications before the irradiation could be within afterwards. Figure 7.3 shows an example of a detector, presenting this behaviour.

An other problem suffered by CSEM sensors was the lack of uniformity on the detector surface of their polysilicon resistor. Figure 7.4 shows the results of the measurements of the bias resistor performed on two CSEM detectors as a function of the strip position. The two upper lines show that the value of the bias resistor was not uniform, varying up to a factor two between the edge and the centre strips. To solve this problem, the company developed a special treatment, based on the diffusion of hydrogen ions. The two lower curves show the result of the measurement on the same detector after the hydrogen treatment, done as a last step of the production. The plot confirms the validity of the hydrogenation treatment to make a uniform poly-resistor value,

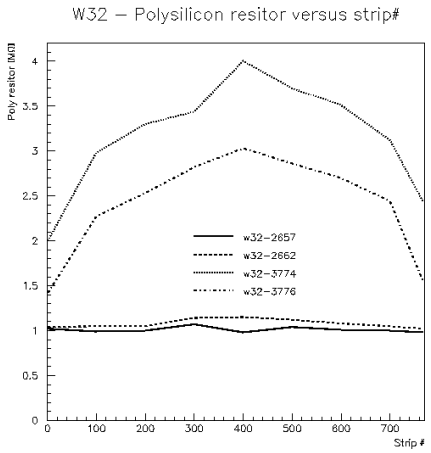

Figure 7.4: Polysilicon resistor value versus strip number. Measurements performed before and after the hydrogenation process are shown.

even though this was not integrated in the manufacturing process, but applied as a corrective step after the passivation.

Further measurements confirmed that the hydrogenation was a reliable method to make the bias resistor values uniform also when integrated in the production sequence, but, unfortunately, the treatment had the inconvenient of rising the detector leakage current. The manufacturer found the solution of this problem in the introduction of a further mask, allowing the hydrogen implantation just on the bias resistor region instead of on the whole detector surface.

7.2 Final judgement on CSEM sensors

Even though the quality of the last delivered batches was certainly improved with respect to the first barrel batches, the ATLAS SCT collaboration decided, on the basis of all the tests performed, not to qualify for tender the swiss manufacturer.

The main problem of those detectors was the high leakage current value before irradiation and the soft breakdown presented by a considerable fraction of them, in

CSEM Barrel Detectors before irradiation

Detector number	IV	Current Stability	Rbias	Cis	Strip Integrity Pinh/break short/open Tot	S/N CCE
2839				0.8pF		
2843						
2846						
2889						
3346					0 / 1 2 / 0 3	
3351					1 / 0 2 / 0 3	
2921						
3339			3.2Mw		2 / 0 2 / 1 5	
3360			3Mw		15 / 0 -	

CSEM W 32 and W31 detectors before irradiation

W32 1st batch 8th of January 1999

Detector number	IV	Current Stability	Rbias	Cis	Strip Integrity Pinh/break short/open Tot	S/N CCE
2661			1.5Mw	0.6pF	0 / 1 0 / 1 2	
3765			1.5Mw	0.6pF	0 / 14 0 / 4 18	
3768			1.5Mw	0.6pF	0 / 0 7 / 0 7	
3775			1.5Mw	0.6pF	0 / 1 0 / 1 2	
3776			1.5Mw	0.6pF	0 / 1 0 / 0 1	

W32 2nd batch June - July 1999

Detector number	IV	Current Stability	Rbias	Cis	Strip Integrity Pinh/break short/open Tot	S/N CCE
3866			4.5Mw	0.6pF		
3867			5.5Mw			
3869			4.5Mw			
3874			4.3Mw			
3845						
3834						
3832					0 / 0 0 / 2 2	
3859					0 / 0 4 / 0 4	
3835						
3842						
3846						
3875						
3880						
3879						
3839						
3854						
3836					0 / 0 2 / 0 2	
3844						
3847						
3853						

W31

Detector number	IV	Current Stability	Rbias	Cis	Strip Integrity Pinh/break short/open Tot	S/N CCE
3901						
3923						
3928						

Figure 7.5: Pre-irradiation measurements performed for the qualification of the CSEM company. Green indicates that the test gave a result in specs, yellow just above the limit and red outside specs.

spite of the efforts made by CSEM to improve the manufacture procedure. This negative decision was also motivated by the fact that, at the time of the deadline fixed to initiate the tendering process, CSEM did not integrate yet in the production process the additional mask, discussed above as the solution of the problem of the current increasing caused by the hydrogenation.

CSEM Barrel Detectors after irradiation

Detector number	IV	Current Stability	Rbias	Cis	Strip Integrity Pinh/breakshort/open Tot	S/N CCE
2839					4 / 3 0 / 10 17	Noisy 0
2843						
2846						
2889						
3346						
3351						
2921						
3339					7 / 0 -	
3360			2.3Mw			Noisy 2

CSEM W 32 and W31 detectors after irradiation

1st batch 8th of January 1999

Detector number	IV	Current Stability	Rbias	Cis	Strip Integrity Pinh/breakshort/open Tot	S/N CCE
2661			1.75Mw		2 / 0 0 / 2 4	
3765					3 / 8 0 / 2 13	Noisy 1
3768					7 / 4 7 / 0 18	
3775					1 / 0 0 / 2 3	Noisy 3
3776			1.5Mw	0.8pF	4 / 0 0 / 3 7	

2nd batch June - July 1999

Detector number	IV	Current Stability	Rbias	Cis	Strip Integrity Pinh/breakshort/open Tot	S/N CCE
3866						
3867						
3869			3.7Mw	1.4pF	0 / 4 0 / 0 4	

Figure 7.6: Post-irradiation measurements performed for the qualification of the CSEM company. Green indicates that the test gave a result in specs, yellow just above the limit and red outside specs.

7.3 Performance of Hamamatsu detectors

One of the companies qualified for tendering in ATLAS was the Japaneese Hamamatsu. The results of some of the tests performed on Hamamatsu pre-series detectors

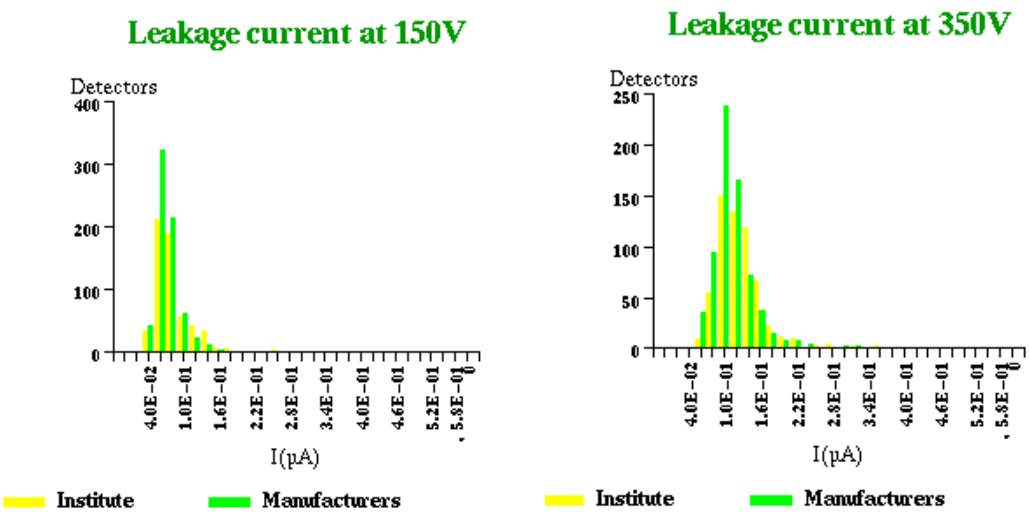

Figure 7.7: Leakage current of Hamamatsu pre-series detectors, measured at Geneva University and by Hamamatsu.

in the last months of this thesis work in ATLAS will be exposed in the following, to compare their performances with respect to CSEM sensors.

The leakage current of the Hamamatsu detectors has extremely low values, on the nA range rather than the μA scale. The values measured at 150 V and 350 V bias are represented in the histograms of figure 7.7. The mean measured value at 150 V is 90 nA, which rises to 118 nA at 350 V. These values are well inside specifications. No soft-breakdown has been observed.

The depletion voltage values all satisfy the specification of being <150 V. The systematic offset of ≈10 V visible in figure 7.8 between the measurement performed in Geneva and by the manufacturer is due to the different extraction of the depletion voltage from the $1/C^2$ versus bias plot. Hamamatsu defines the value to be at the onset of the plateau instead of the intersection of the two straight lines.

All the intrinsic characteristics of the Japanese detectors are inside specifications. In the figure 7.9 an example of polysilicon bias resistor measurement is shown. The resistor values are uniform across all strips of the detector. The average value is

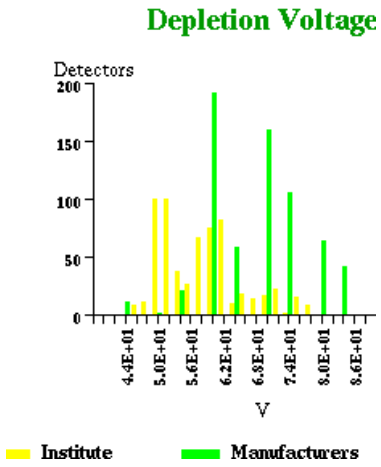

Figure 7.8: Full depletion voltage distribution for a set of Hamamatsu detectors.

1.7 MΩ, within the specified range of 0.5-2.0 MΩ.

The Hamamatsu sensors show a satisfactory behaviour also after irradiation. The leakage current stays within specifications, as well as all the other electrical characteristics.

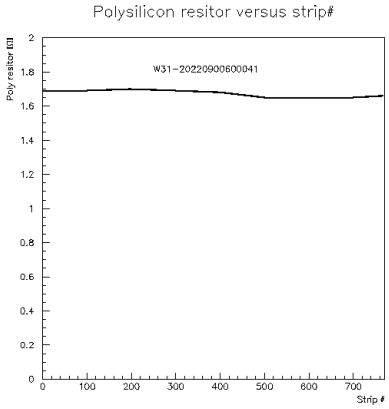

Figure 7.9: Polysilicon bias resistor measurement on an Hamamatsu sensor.

An example of readout measurement of an irradiated sensor at the end of its

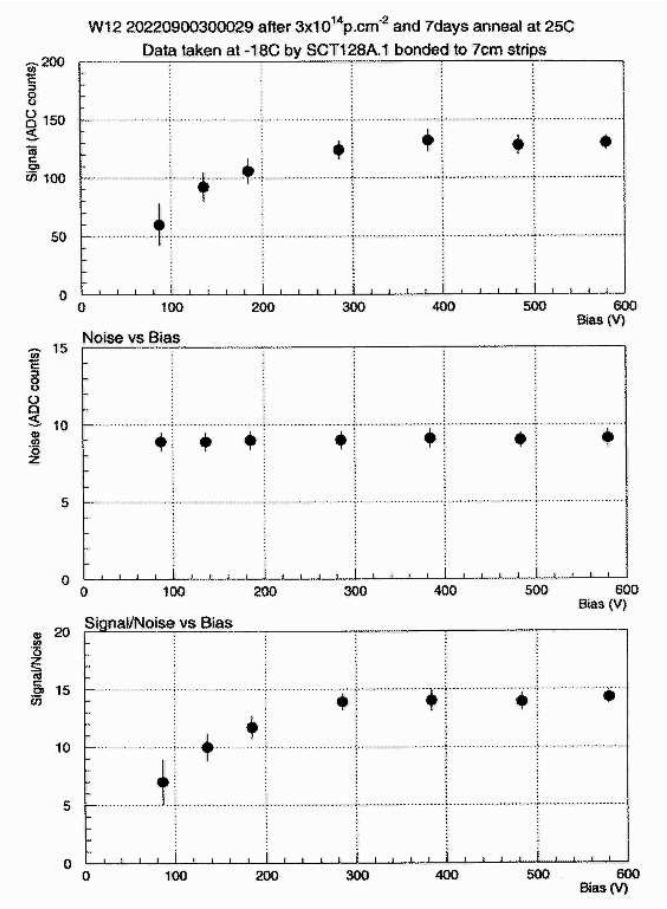

Figure 7.10: Signal, noise and S/N of an irradiated Hamamatsu detector measured with the SCT128A chip.

beneficial annealing is presented in figure 7.10. The plateau of the charge collection efficiency starts at around 300 V.

The strip defect rate is found to be very low both for irradiated and not-irradiated sensors.

In summary the Hamamatsu detectors met all the ATLAS specifications and have shown an overall excellent quality.

Part II

TPC reconstruction in the HARP experiment

Chapter 8

Physics motivation of the HARP experiment

8.1 Motivations

The leptonic flavour mixing and the existence and characteristics of the Higgs particle remain the unexplored sectors of the Standard Model and can disclose signals of physics beyond the standard model. The latter, as mentioned at the beginning of this thesis, will be mainly the task of the LHC experiments, while the former has received a great boost from the evidence for neutrino oscillations and will require dedicated infrastructures, like Neutrino Factories.

Key features of a Neutrino Factory are a high intensity and a precisely understandable neutrino flux from the stored muon beam. Although the neutrino beam is made of two different flavours, their opposite leptonic numbers eliminate pollution effects. The different charge between the source muons, whose polarity can be reversed to produce $\bar{\nu}_e$ beams, and the muons produced by the ν_μ ($\bar{\nu}_\mu$) generated by an oscillation of the initial ν_e ($\bar{\nu}_e$) provides a clear cut signal for the appearance of a different type of flavour. This is crucial for the observation of CP violation in the leptonic sector.

Pions are the natural source of muons and the quality requirements transfer to the generating pion beam. The HARP experiment has been designed to provide the information necessary for the optimisation of targets and projectiles for pion produc-

tion, by measuring on thin and thick nuclear targets proton and pion cross sections with momenta in the range 1.5 to 15 GeV/c [43]. These measurements will allow a substantially improved knowledge of the yield of secondary cosmic rays and of the corresponding neutrino flux whose attenuation constitutes the evidence for atmospheric neutrino oscillations. As a further byproduct, an accurate measurement of the backward low momentum pions is crucial for the design of a high intensity stopped muon source, dedicated to complementary studies of the leptonic flavour sector, like flavour changing rare decays. At present, the knowledge of low momentum pion production, for which the rate is the highest, is estimated by MonteCarlo generators [45] that are however affected by a typical systematic uncertainty of the order of or beyond 15 percent or by fragmentary and rather old data [**?**] without a full coverage of the solid angle and with very large normalisation errors.

The experiment in the present and future phases aims to determine cross sections with a precision of a few percent for pion production and of ten percent for kaons and to study their dependence upon proton, pion and deuteron beams, upon the initial momentum in the 1.5-100 GeV/c range and upon high-Z, oxygen and nitrogen targets.

8.2 Physics background

Neutrino oscillations are made possible by the inclusion in the standard model of right handed neutrinos that are needed to form the Dirac mass term, like for quarks. This could be seen not quite as an extension but as a completion of the standard model that would then treat leptons and quarks on the same footing. Indeed, right handed neutrinos were excluded by the lack of evidence of massive neutrinos, but today are a prerequisite for neutrino oscillations.

The Dirac mass terms for neutrinos arises from the vacuum expectation value of the

Higgs doublet ϕ like for down quarks:

$$\lambda_{ij}\phi\bar{\psi}^i_{left}\nu^j_{right} \rightarrow m_{ij}\bar{\nu}^i_{left}\nu^j_{right} \tag{8.1}$$

where ij are generation indices and λ is the Yukawa coupling. The mass matrix m_{ij} for up and down leptons is diagonalised with bi-unitary transformations:

$$m^{up,down}_{diagonal} = U^{up,down}_L m U^{+up,down}_R \tag{8.2}$$

where $U^{up,down}_{L,R}$ are different specific unitary matrices.

Correspondingly, the left states appearing in the original weak currents are translated into the basis of the mass eigenstates at the price of a flavour mixing in the weak currents represented by a CKM like mixing matrix M_{ckm} , related to the matrices $U^{up,down}_L$ by:

$$M_{ckm} = U^{+up}_L U^{down}_L \tag{8.3}$$

Neutrino weak current eigenstates are connected to the combination of down lepton mass eigenstates defined by:

$$\mid \nu^{current}_\alpha >= \sum_i U^*_{\alpha i} \mid \nu^{mass}_i > \tag{8.4}$$

The present pattern of neutrino mixings and of mass differences that I will shortly review makes the analogy with the quark sector quite unnatural, where mixings are hierarchically correlated to masses. As discussed later, the preferred interpretation of the experimental results features a maximal mixing between the second and the third generation, in striking contrast with the tiny mixing of the top quark with strange and down quarks, and microscopic neutrino mass differences measured in units of charged leptons mass differences.

The absence of an electric charge allows the possibility of an extra Majorana mass term that violates the lepton number. That would represent a real extension of the Standard Model and may justify the differences with the quark sector.

The Majorana term

$$\lambda_{ij}^{Majorana}\phi_{singlet}\bar{\nu}_{right}^{Ci}\nu_{right}^{j} \rightarrow m_{ij}\bar{\nu}_{right}^{Ci}\nu_{right}^{j}, \tag{8.5}$$

where ν_{right}^{C} is the charge conjugated field, connects two right handed fields and violates the lepton number by 2 units.

The field $\phi_{singlet}$ is a new scalar field, singlet under the $SU2_L$, and does NOT belong to the Standard Model. Its vacuum expectation value can be chosen to be much larger than the usual one responsible for the electroweak symmetry breaking, to generate a very high Majorana mass that, together with the Dirac mass leads to the so called see-saw mechanism.

Indeed, the mass matrix with both contributions is of the form:

$$M = \begin{pmatrix} 0 & m_{Dirac} \\ m_{Dirac}^{T} & m_{Majorana} \end{pmatrix} \tag{8.6}$$

with a low eigenvalue smaller than the Dirac mass by a factor $m_{Dirac}/m_{Majorana}$. The smallness of the ratio of neutrino masses to the ones of ordinary charged leptons could be a signal of a see-saw mechanism and give an estimate of the new mass scale $m_{Majorana}$.

Finally, the new possible Majorana term restricts the freedom in redefining the phases of the lepton fields to re-absorb some of the parameters of the CKM matrix [46],[47]. The most general neutrino mixing matrix in this case contains two extra phases, sources of additional CP violation in the lepton sector with respect to the quark sector that are associated with the heavy mass scale.

As far as oscillations are concerned the extra phases play no role and the mixing matrix can be assimilated to the CKM one.

The experimental evidence for neutrino oscillations concerns three groups of measurements: the solar neutrinos, the atmospheric neutrinos and the ground based experiments [48]. It constraints the mass differences and the mixing angles of the matrix in eq. 8.3. The absolute value of the neutrino masses are still poorly constrained and

the limits derive from the end point spectrum of the electrons in tritium decay that sets:

$$m_{\nu_e}^{effective} < 2.5eV \text{ [49]}, \tag{8.7}$$

where m_ν is the minimal neutrino mass of the combination coupled to the charged electron current, and from cosmological arguments that impose:

$$\sum_i m_{\nu^i} < 2.5eV \tag{8.8}$$

As we will see, some mass differences seem to be significantly smaller than the above limits suggesting either a strong degeneracy or poor experimental limits.

The absolute value of the Majorana mass term regulates rare processes with lepton number violation, such as the neutrino-less double beta decay:

$$N + N \rightarrow P + P + e^- + e^- \tag{8.9}$$

The limit on the lifetime of such a process corresponds to an exchanged (average) Majorana mass in the eV range and could be extended in the future down to the meV range [50].

Neutrino oscillations are basically a typical quantum mechanical effect affecting the time evolution of a state generated by a weak current that is a linear superposition of mass eigenstates with different eigenvalues. The current eigenstates during the time evolution change their relative phases and the initial state oscillates into a superposition of itself and the other states of the current basis. In formulae:

$$\mid \nu_i^{current}(t) >= \sum_k U_{ik}^* exp^{-i(E_k t - p_k L)} \mid \nu_k^{mass} > \tag{8.10}$$

where U_{ik}^* are the same mixing matrix elements of eq.8.2. The relative phases evolve with time with the energy differences. In the case of mass degeneracy, the phase is an overall phase that leaves the state in its original superposition. Assuming a common momentum and neglecting higher order effects in the neutrino masses, one

can rewrite, at a distance L and after a time t:

$$\mid \nu_i^{current}(t) >= \sum_k U_{ik}^* exp^{-i(m_k^2/2E)L} \mid \nu_k^{mass} > \tag{8.11}$$

The probability of finding a different state oscillates with time and takes a very simple form for a two-state oscillation that is a good approximation when the experimental conditions are sensitive to a dominant mass difference only.

$$P(\nu_i \rightarrow \nu_k) = sin^2 2\theta sin^2(1.27\Delta m^2(eV^2)(L(Km)/E(GeV))) \tag{8.12}$$

where Δm^2 is the mass square difference and physical units have entered the expression.

So far, oscillation experiments have been only able to see the disappearance of the initial state, but have not been able to resolve the typical oscillation pattern. Still, the information gathered so far represents a compelling evidence for oscillations.

Solar electron neutrinos have been the first to disappear: the flux reaching the earth is roughly half of what is expected on the basis of the solar standard model. Recently a crucial test has been added to the pure disappearance: the flux of neutrinos coming from the sun measured via neutral current interactions agrees with the expected value.

Solar oscillations take place partly in the sun and may be affected by the so called

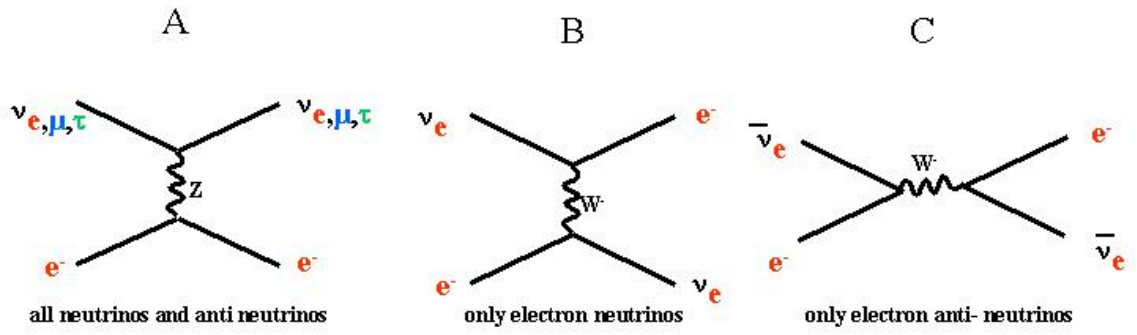

Figure 8.1: The amplitudes leading to matter effects on oscillations.

MSW effect: matter can change the Hamiltonian of different neutrino species and alter the relative oscillation pattern. Indeed, the ν_e and $\bar{\nu}_e$ receive a contribution to their Hamiltonian in matter that is not shared by the other neutrino species. The interactions with the atomic electrons can occur via neutral currents (figure 8.1a), or via charged currents (figure 8.1b,c). The latter two amplitudes involve ν_e and $\bar{\nu}_e$ only, come with opposite signs due to the Fermi statistics and mark a difference between ν_e and $\bar{\nu}_e$. Matter propagation is then different from vacuum propagation, and the oscillation patterns depends upon the amount of matter encountered, its density, the beam energy and the particle/anti-particle nature. In particular, there is a "resonant" energy-length condition that makes the oscillation complete.

Finally, the oscillation depends upon the mixing angle and the absolute value of the maximal suppression of the initial state provides a measurement of the mixing angle.

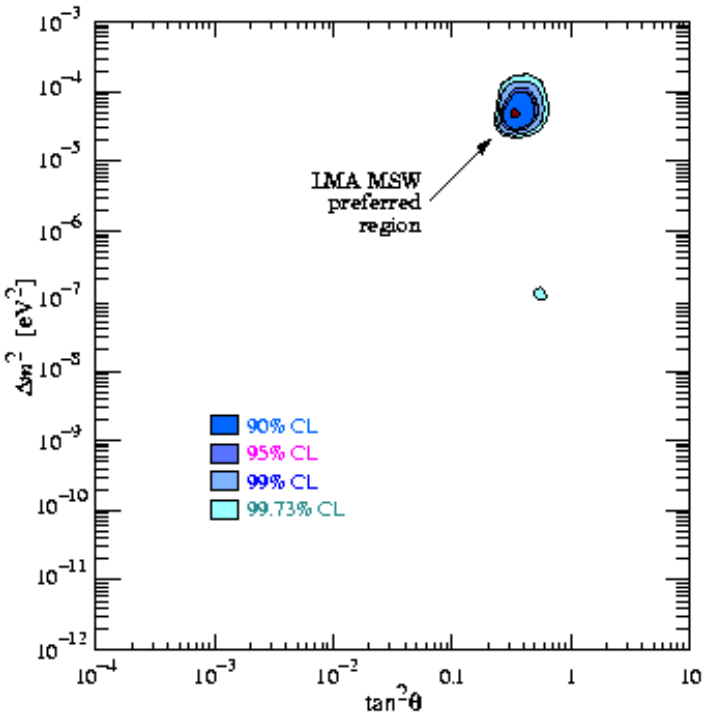

Figure 8.2: Allowed region of the solar neutrino parameter space as from [51].

The results collected from the analysis of the most recent solar experiment SNO are summarised in figure 8.2 and tend to select a solution called the MSW-large angle with a mass difference of the order of $7 \times 10^{-}5eV^2$ and a mixing angle θ between the electron and an effective single state mixture of muon and tau neutrino given by $tan^2\theta = 0.26$ [51]. The forthcoming observation of solar monochromatic neutrinos based on the ^7B reaction will further support or disprove the preferred solution.
Last December, the KamLAND collaboration has reported a deficit of the $\bar{\nu}_e$ flux with energies >3.4 MeV, coming from reactors at a dominant distance of about 180 Km.

$$\frac{\bar{\nu}_e measured}{\bar{\nu}_e expected} = 0.611 \pm 0.085(\text{stat}) \pm 0.041(\text{syst})[52] \tag{8.13}$$

This is compatible, as shown in figure 8.3, only with the LMA solution, that is than

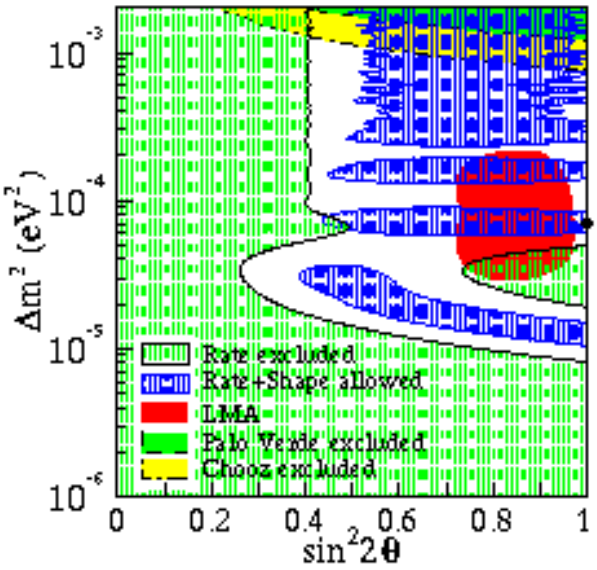

Figure 8.3: Excluded regions of neutrino oscillation parameters for the rateanalysis and allowed regions for the combined rate and shape analysis from KamLAND at 95% C.L. At the top are the 95% C.L. excluded region from CHOOZ [53] and Palo Verde [54] experiments and the 95% C.L. allowed region of "Large Mixing Angle" solution of solar neutrino experiments [55]. The thick dot indicates the best fit to the KamLAND data in the physical region: $\sin^2 2\theta$=1.0 and $\Delta m^2 = 6.9 \times 10^{-5}$ eV^2.

confirmed as "the" solution for the ν_e ($\bar{\nu}_e$) oscillations.

Atmospheric neutrinos are produced by primary cosmic rays in the atmosphere. We reiterate that their flux is evaluated through Monte Carlo simulations and the contribution of HARP may become essential to reduce the corresponding systematic uncertainty. The Super Kamiokande detector has brought evidence for oscillations by reporting a decrease of the expected flux that depends upon the length of the path covered by neutrinos. Indeed, the isotropy of the neutrino flux leads, independently from its absolute normalisation, to a symmetry between neutrinos coming from the bottom, produced at the antipodes and passing through the earth, and those coming from the top. An asymmetry has been measured, that, together with the calculated decrease of the absolute flux, has a natural explanation in terms of the oscillation of the muon neutrino mainly into a tau neutrino.

$$\frac{FluxUp}{FluxDown} = 0.54 \pm 0.04[56] \tag{8.14}$$

with a maximal mixing , $sin^2 2\theta_{atm} > 0.02$, and a mass difference within the limits:

$$1.6 \times 10^{-3} eV^2 < \delta m^2_{atm} < 3.9 \times 10^{-3} eV^2 \tag{8.15}$$

This is a measurement that could be affected by the atmospheric neutrino flux systematics.

The effect has been confirmed by the baseline experiment K2K where the flux of a monitored ν_μ beam has been measured at a distance where, according to ν_μ oscillations, a depletion should be visible. The observed suppression is of 52/80 expected events [57] and the corresponding mass limits under a maximal mixing hypothesis are:

$$1.5 \times 10^{-3} eV^2 < \delta m^2_{atm} < 3.9 \times 10^{-3} eV^2 \text{ [58]} \tag{8.16}$$

very consistent with the result of atmospheric measurements. A replica of the K2K target has been used with the HARP detector in order to minimise any uncertainty

in the K2K results, coming from the pion production cross section.

The results of the LSND experiment [60] seem to indicate the existence of a third mass difference besides the two from solar and atmospheric experiments, that cannot be accommodated within the standard three neutrino picture, that has been confirmed by the precise measurements of the Z width at LEP:

$$N_\nu^{LEP} = 2.984 \pm 0.008 \text{ [59]} \tag{8.17}$$

If the LSND result is confirmed (by MiniBooNe), it can only be accommodated within a four neutrino mixing pattern, where one of the mixed states does not couple to weak intermediate bosons to evade the LEP limit. Nevertheless, the existence of such a "sterile" neutrino would affect the nucleosynthesis process in the early universe and, without a compelling experimental evidence, is not considered the preferred scenario. Instead, the existence of two distinct mass differences can be accommodated within a simple scheme for the mass spectrum and the mixing angles, reported in figure 8.4. The corresponding mixing matrix can be parametrised as follows assuming maximal

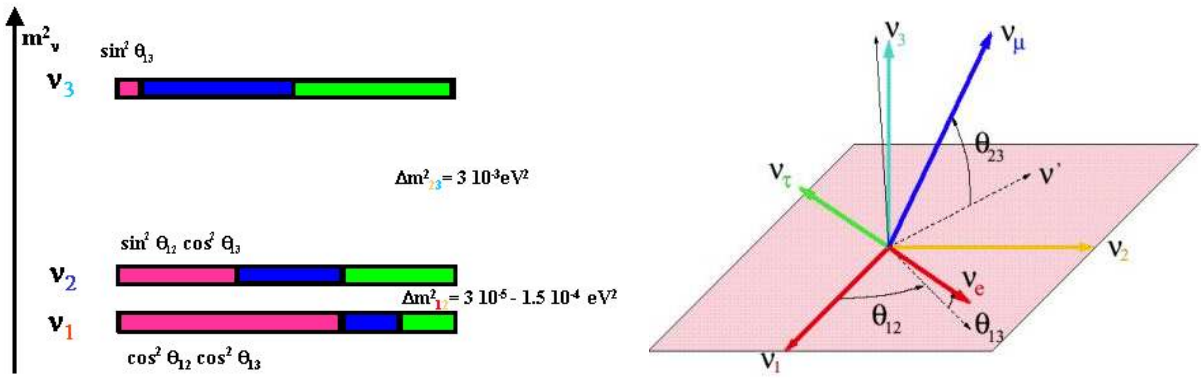

Figure 8.4: Three-neutrino $(\text{Mass})^2$ spectrum (left plot) that accounts for the flavour changes of the solar and atmospheric neutrinos: the ν_e fraction of each mass eigenstate is red, the one of ν_μ is blue and the one of ν_τ green, and scheme of the mixing angles (right plot).

mixing of atmospheric oscillations and the LMA solution:

$$\begin{array}{c} \\ \nu_e \\ \nu_\mu \\ \nu_\tau \end{array} \begin{array}{c} \begin{array}{ccc} \nu_e & \nu_\mu & \nu_\tau \end{array} \\ \begin{pmatrix} \sim \frac{\sqrt{2}}{2} & \sim -\frac{\sqrt{2}}{2} & s_{13}e^{i\delta} \\ \sim \frac{1}{2} & \sim \frac{1}{2} & \sim -\frac{\sqrt{2}}{2} \\ \sim \frac{1}{2} & \sim \frac{1}{2} & \sim \frac{\sqrt{2}}{2} \end{pmatrix} \end{array} \tag{8.18}$$

where δ is a CP violating CKM-like phase.

The crucial issue for future experiments is the value of $sin(\theta_{13}) \equiv s_{13}$ that governs the neutrino oscillation yield of CP violation in the leptonic sector, given by, for $\nu_e \rightarrow \nu_\mu$ oscillations:

$$\frac{P(\nu_e \rightarrow \nu_\mu) - P(\bar{\nu}_e \rightarrow \bar{\nu}_\mu)}{P(\nu_e \rightarrow \nu_\mu) + P(\bar{\nu}_e \rightarrow \bar{\nu}_\mu)} = A_{CP} \propto \frac{\sin\delta \sin(\Delta m^2_{12} L/4E) \sin\theta_{12}}{\sin\theta_{13} + \text{solar term...}} \tag{8.19}$$

that increases for decreasing values of s_{13}. The ν_e oscillations are the best to observe CP violation that in general requires a large solar and small atmospheric oscillation probabilities, which is not the case for ν_μ oscillations.

A background to genuine CP violation is represented by the matter effect which can produce a fake asymmetry. Figure 8.5 shows the dependence of the CP asymmetry

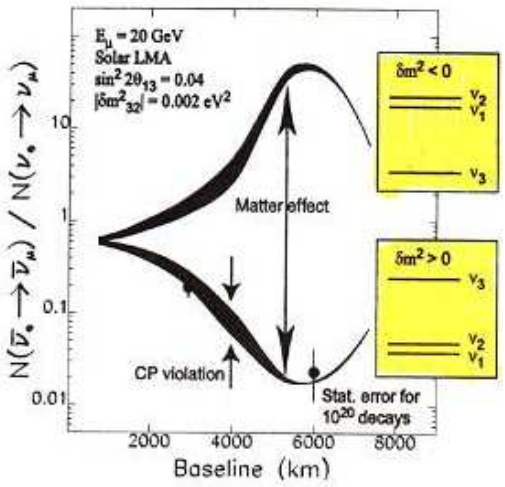

Figure 8.5: Ratio of the oscillation probabilities of anti-neutrinos and neutrinos as a function of the baseline. After about 1000 km, matter effects dominate over CP violation, whose effects even go to zero at a particular baseline around 7500 km.

upon the baseline and the sign of Δm^2_{32}, and highlights the relevance of matter effects with respect to genuine CP violation effects.

The Neutrino Factory [61] can measure carefully the asymmetry in the appearance which measures CP violation, and, by varying the beam energy and the distance of the detector, can disentangle genuine CP violation effects from matter effects, establishing at the same time the sign of Δm^2_{23}. The Neutrino Factory, has also the unique feature of making possible a measure of $\nu_e \to \nu_\tau$ oscillations which are expected to show a CP asymmetry opposite to the one of $\nu_e \to \nu_\mu$ from CPT invariance.

Figure 8.6 gives a comparison of the sensitivity in the $\Delta m^2_{23} - s^2_{13}$ plane among the existing, forthcoming or competing projects.

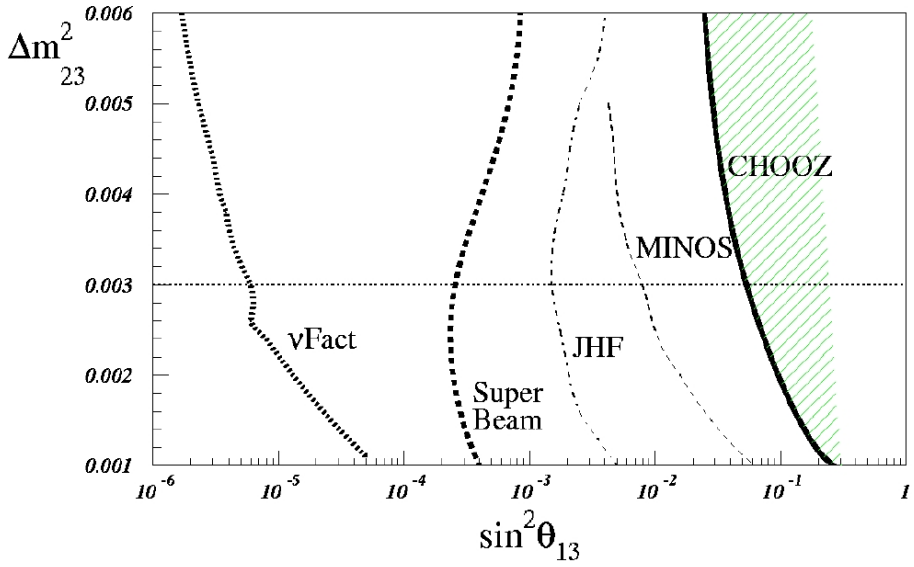

Figure 8.6: Comparison of reach in the $\nu_\mu \to \nu_e$ oscillations. Right to left: present limit from the CHOOZ experiment, expected sensitivity from the MINOS experiment, from JHF to SuperKamiokande project, from a possible neutrino beam from CERN-SPL to a 400 kton water Cherenkov detector in the Frejus tunnel, from a Neutrino Factory with a 40 kton Magnetic Detector.

The feasibility of the very intense neutrino fluxes qualifying the factory will be

clarified by the investigations carried out at the HARP experiment.

8.3 Summary of design parameters for a hadron production experiment

The design considerations of the Neutrino Factory require the following measurements:

- Proton beam with momentum between 2 and 24 GeV/c.
- Thick high-Z targets. However, since the proton target of the neutrino factory is in a very high magnetic field, its final efficiency for pion production will be determined from a combination of thin- and thick-target measurements, and calculations. The calculated thick-target yield in a non-magnetic environment is checked by measurement.
- Secondary pion yield over the phase space: 100 MeV/c $< p_l <$ 700MeV/c and $p_t <$ 400MeV/c; secondary proton yield to assess problems of induced radiation.
- Deuterium beams with momentum of 1 GeV/c per nucleon to assess its usefulness for a better π^+ / π^- ratio than that obtained with a proton beam.
- Yield of backward-going pions to assess its usefulness for a high-intensity stopped-muon source.

For a reliable calculation of the atmospheric neutrino flux down to 100 MeV energy, the following measurements are needed:

- Proton and pion beam with momentum between 1 and 100 GeV/c.
- Targets of oxygen and nitrogen nuclei.

- Secondary π^+, π^-, K^+, K^- and proton yields over the full phase space, with particle energy as the kinematical quantity of primary interest. The precision requirement is a few per cent for π^+, π^- and proton, and $\sim 10\%$ for kaons.

- Helium ions with momentum between 0.5 and 50 GeV/c per nucleon to complement the proton data.

In the context of atmospheric neutrinos, it should be recalled that the measurement precision of the π^0/e ratio in SuperKamiokande, which is relevant for the question whether a sterile neutrino is required, depends on the precision of the measurement of the π^0 production via neutral currents in the K2K experiment at KEK. This experiment is in turn limited by the knowledge of pions and kaons produced by 12 GeV protons on a thick Al target. The results from HARP would be instrumental in achieving a better precision on this important cross-section. The MiniBooNe experiment at Fermilab would also benefit from precision measurements of 8 GeV/c protons on a thick Al target. This experiment aims to refute or confirm the LSND neutrino oscillation claim.

The HARP experiment aims to measure the hadron production cross sections using proton and pion beams from the CERN PS in the range 2–15 GeV/c. During the two seasons of data taking, several thin targets spanning the full range between Be and W nuclei have been used as well as a selection of thick targets and cryogenic targets.

8.4 HARP precision requirements

Both for the neutrino factory and for the atmospheric neutrino flux, an overall precision of 2% for the inclusive cross-section of secondary particles is the primary aim. This is motivated by the wish to obtain 5% precision both on the production of accepted muons in the neutrino factory's front stage, and on the atmospheric neutrino flux. Either prediction will involve uncertainties beyond those of the results of HARP.

A 2% overall accuracy requires some 10^4 events for each measured point.

To achieve this precision, the detector has been designed to have as much redundancy as could be afforded. For example, pion/proton identification is provided by $\mathrm{d}E/\mathrm{d}x$ in a Time Projection Chamber (TPC), by time of flight (TOF), and by a threshold gas Cherenkov detector. Overlap in certain kinematical domains will help to understand absolute efficiencies.

Chapter 9

The HARP detector

The HARP experiment was approved in February 2000. It was constructed in a very tight time schedule and some of the most important of its subsystems (including the TPC and the Cherenkov detector) were built from scratch. The first data taking started in August 2001 and was interrupted for the PS winter shutdown. At the time of writing, the second and last data taking period is nearing its end.
In the last years, a lot of activity has taken place within the HARP Collaboration to understand the detector behaviour, to solve the unavoidable problems presented by any commissioning, to calibrate all subsystems, and to develop the reconstruction software.
In this chapter, an overview of the detector is given, together with some results on the subsystem performances at the time of writing. As my own work in HARP has been devoted to the development of the reconstruction software for the TPC, this particular sub-detector will be treated in more detail in a following chapter.

9.1 Overview of the HARP detector

The layout of the HARP spectrometer is shown in figure 9.1. Its subsystems are:

- TPC: to measure tracks at large angles; the target is located inside the TPC.
- Solenoid magnet: generates a 0.7 T longitudinal magnetic field for the TPC.

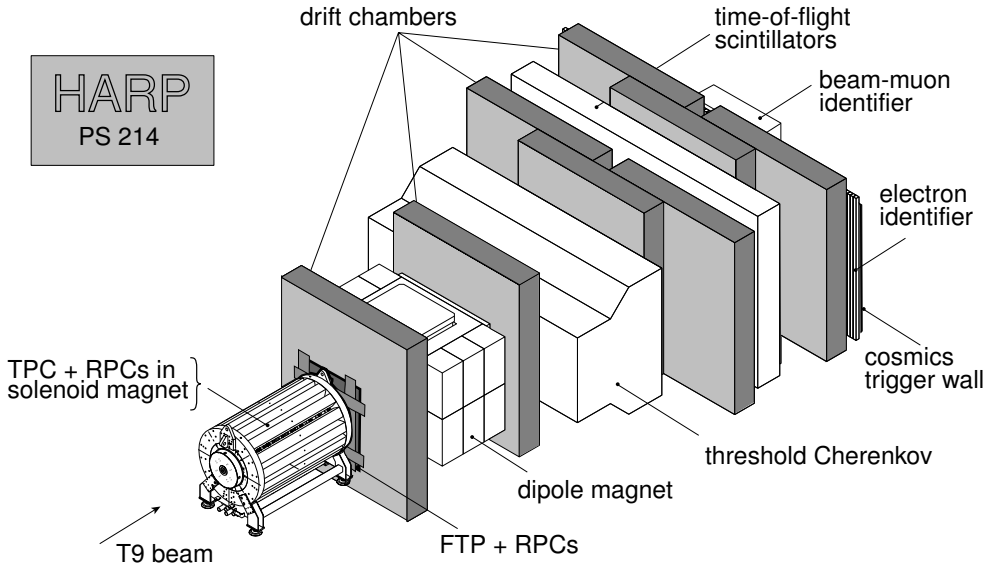

Figure 9.1: Layout of the HARP detector.

- Inner Trigger Cylinder (ITC): to trigger on tracks at large angles; it consists of three cylindrical layers of scintillating fibres located around the target.

- Forward Trigger Plane (FTP): to trigger on forward tracks; it consists of two planes of scintillator sheets; a central hole of 6 cm diameter allows non-interacting beam particles to pass through without triggering.

- RPCs: to provide discrimination between pions and electrons by time-of-flight; 30 chambers surround the TPC and intercept tracks at large angles; further 16 chambers, arranged in two planes, are located in front of the FTP to intercept tracks at intermediate angles.

- Drift-chambers: five modules with 4 drift-chambers each are the key element of forward tracking; each drift-chamber consists of three wire planes, one with vertical wires and two with wires at $\pm 5^{\circ}$ with respect to the vertical ones; three further modules, each with only one drift-chamber, are used to define the

position of clusters in the electro-magnetic calorimeter.

- Dipole magnet: the 0.5 T vertical field allows the momentum spectrometry of forward tracks.

- Cherenkov counter: to discriminate between protons and pions at high momentum; the threshold is provided by C_4F_{10} gas at atmospheric pressure.

- TOF wall: a plane of scintillator counters to discriminate between protons and pions at low momentum.

- Electron identifier: lead-scintillating fibre counters, to discriminate between hadrons, and photons and electrons.

- Cosmic trigger wall: a plane of scintillator sheets to trigger on cosmic muons, for monitoring and calibration purposes.

- Beam muon identifier: a small iron-scintillator calorimeter to identify beam muons.

The spectrometer is complemented by beam instrumentation consisting of:

- Beam Cherenkov counters: threshold counters, either 5 m (BC-A) or 3 m (BC-B) long. They are filled with CO_2 and are used to discriminate protons, pions and electrons forming the beam.

- Beam scintillator counters: they are identified as TOF-A and TOF-B and are used to detect the the passage of a beam particle, to possibly identify it by its time-of-flight, and to start the trigger logic.

- Beam MWPCs: are used to define the track parameters of an incoming beam particle; there are three x-y chambers with 1 mm wire spacing and one x-y chamber with 4 mm wire spacing.

The TPC, together with the forward spectrometer, ensures nearly full 4π coverage for momentum measurement.

9.2 Detector performance

9.2.1 Beam detectors

To measure the hadron production cross section, a knowledge of the beam composition is fundamental for a correct normalisation. The beam detectors are needed to distinguish the different particles that are present in the beam and to measure their position and momentum.

In HARP the beam particle identification is performed using two Cherenkov detectors placed along the beam line and by the measurement of their time-of-flight between two scintillator planes, located 21 m apart. The use of the beam instrumentation as a function of the beam momentum is summarised in Table 9.1. Figure 9.2 shows

Beam Momentum (MeV/c	Electron tagging	π, p tagging
< 5	BCA at 1 bar	TOF
5	BCA at 0.6 bar	TOF + BCB at 2.5 bar
> 5	electron identifier	BCA at 1.25 bar + BCB at 1.5 bar

Table 9.1: Use of beam instrumentation to tag particles.

the good particle separation potential of the time-of-flight counters for a beam momentum of 3 GeV/c. The TOF spectrum allows not only to separate particle species, but also to calibrate the beam momentum to a few MeV/c [62] and to estimate the beam momentum spread.

It is interesting to note that the beam contains enough deuterons to measure at least the total cross section of deuterons on nuclei. A small admixture of tritons is even apparent in figure 9.2.

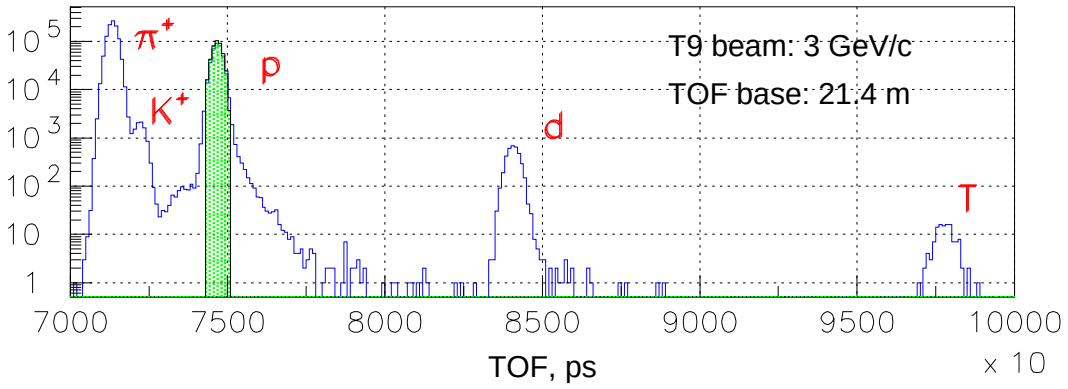

Figure 9.2: Separation of protons from other particles in the T9 beam at a momentum of 3 GeV/c. Electrons are rejected with the beam Cherenkov counters. The shadowed band corresponds to a purity of 98.7% for proton selection.

9.2.2 RPCs

At large production angles, the separation between electrons, pions and protons rests on the dE/dx measurement in the TPC. This technique is not effective to separate electrons and pions in the momentum range between 150 and 250 MeV/c. Given the sizeable rate of electrons arising from the conversion of photons from π^0 decay, another discrimination method must be employed in that momentum range. The choice was to employ a time of flight technique. In order to achieve good separation on the short flight path of about 40 cm, a time resolution better than 300 ps is needed. The time-of-flight measurement is performed with barrel and forward Resistive Plate Chambers surrounding the TPC.

The barrel RPC detector consist of two layers of 15 chambers segmented in 8 pads 24 cm long in the beam direction while the forward one is composed of two layers of 8 chambers located after the TPC.

At present, the time calibration of the RPCs is not completed and it is not yet

possible to discriminate particles by time-of-flight. Nevertheless, very preliminary distributions of time-of-flight for one pad ring are presented in figure 9.3. The particles

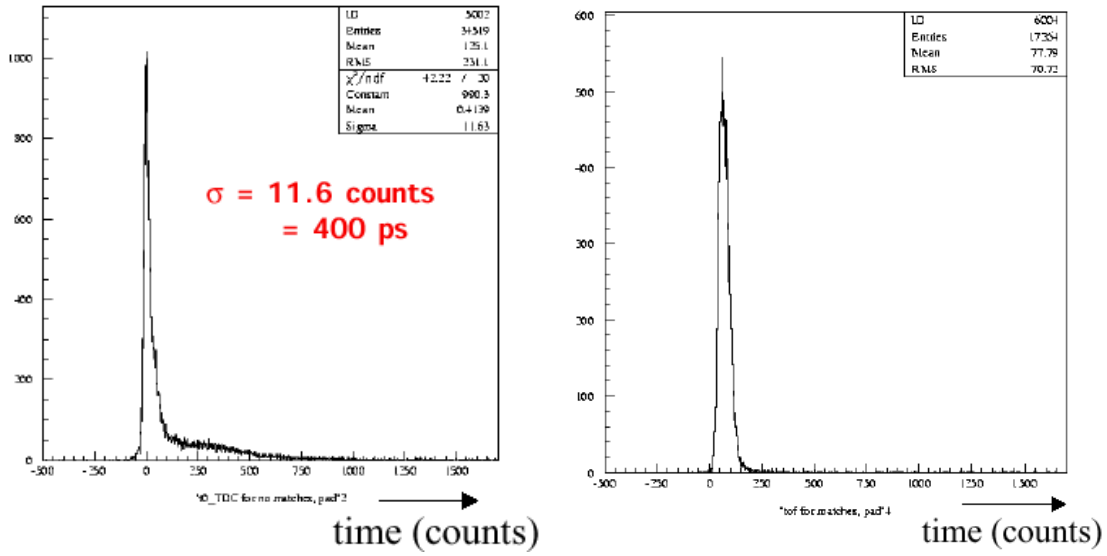

Figure 9.3: Barrel RPCs time distribution for neutral (left plot) and charged particles (right plot).

in the left plot are those not matching any TPC track. They can be identified as neutral particles, when the absence of match of a TPC track is not due to TPC reconstruction inefficiency. A resolution of 400 ps for barrel RPCs is observed. This includes the uncertainty on z due to the target length (10 cm in this sample) and to the pad length (of 24 cm).

For particles with a matched track in the TPC the distribution is wider. No selection on track length or momentum has been applied, that would make the distribution narrower.

9.2.3 Drift chambers

The tracking in the forward direction is performed using 23 drift chambers recuperated from the NOMAD experiment [63]. They have three gas gaps and the wires

are placed at a stereo angle of $\pm 5^\circ$ with respect to the magnetic field direction. In HARP the chambers have been turned by 90° with respect to the NOMAD situation, in order to align the wires along the vertical magnetic field of the dipole magnet.

The drift chambers are grouped in five modules of four chambers each, while the remaining three are part of the electron identifier (figure 9.1).

The efficiency of the chambers has been measured from the trajectories of non-interacting beam particles. The typical efficiency per wire plane is $\sim 90\%$[68], as shown in figure 9.4. Notice that a few seemingly lower efficiencies stem from chambers located outside the beam particle trajectories and have no meaning for lack of statistics. The overall efficiency is significantly lower than 100%, due to the fact that

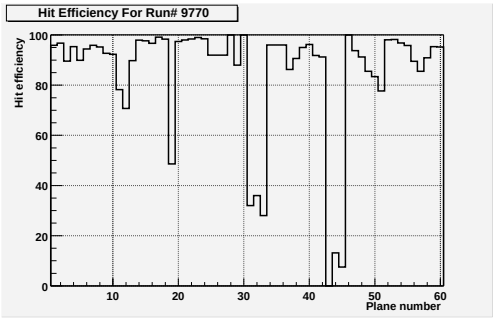

Figure 9.4: Hit efficiency per wire plane of the NOMAD drift-chambers, for non-interacting beam particles.

the original gas mixture used in NOMAD (40% argon + 60% ethane) was flammable and had to be changed for safety reasons. In HARP, the drift chambers are filled with a mixture of 90% argon + 9% carbon dioxide + 1% methane. However, the low efficiency per wire plane is compensated by the use of as many as 12 planes per drift-chamber module.

At the time of writing, the alignment of the drift chambers is in progress and initial results give a resolution of $400\,\mu$m. [64].

Particle	Threshold momentum
pion	2.6
kaon	9.3
proton	17.6

Table 9.2: Threshold momenta for the different particles in the Cherenkov detector.

9.2.4 Cherenkov

The Cherenkov detector allows particle identification in the forward direction for particle of high momenta ($> 3\,\mathrm{GeV/c}$). It is located between the second and third layer of the drift-chambers at a distance of 6 m from the target. It is operated at atmospheric pressure with perfluorobutane (C_4F_{10}), eight times heavier than air. The threshold momenta for the different particles to give a signal in the detector are summarized in table 9.2.

Figure 9.5 shows the detector response to charged pions as a function of the momentum. The measurements have been performed using non-interacting beam particles and good agreement with the expectations is found.

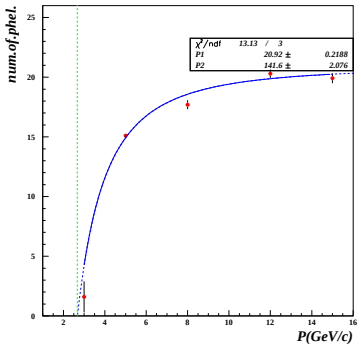

Figure 9.5: Number of photoelectronsproduced by charged pions in the Cherenkov counter as a function of the momentum. The points denote the measurements, the full line the expectation.

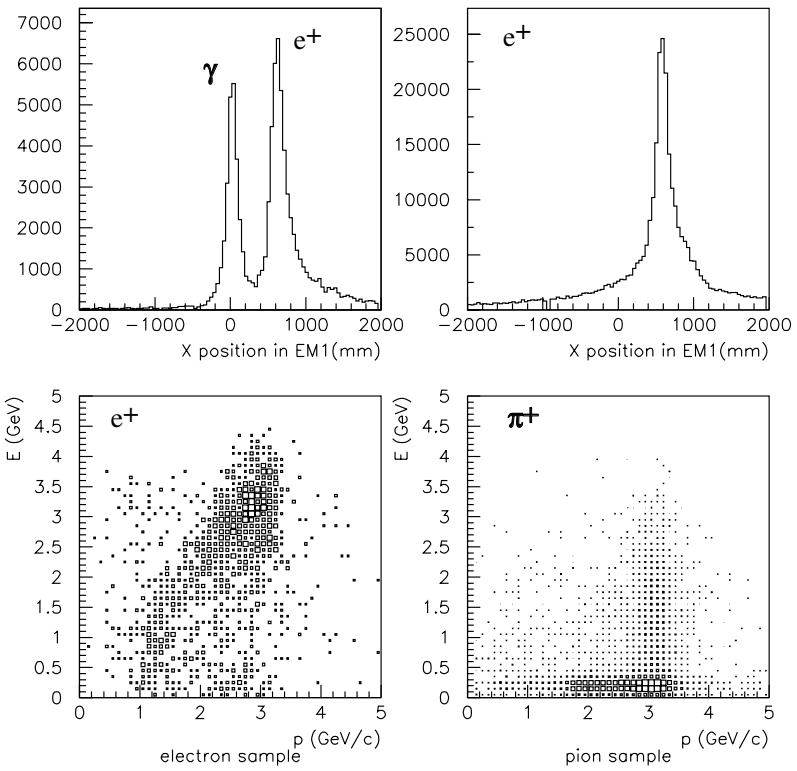

Figure 9.6: Response of the electromagnetic calorimeter to photons, electrons and pions.

9.2.5 Electron identifier

The primary purpose of the electron identifier is to discriminate electrons from pions, when both are above the Cherenkov treshold.

The electron (and π^0) identifier is composed by various elements. The first one is a "preshower", converting a good fraction of gammas from π^0decay. The identification is done through the invariant mass of the two photon system, reconstructed in the assumption that both photons originate from the target centre. The second set of elements is constituted by three NOMAD drift chambers out of which just one plane per chamber is read giving one track point per particle. Then, following the z direc-

tion, there are two stages of calorimeter modules previously used by the CHORUS experiment [65], [66]. The modules are made of lead and scintillator fibers ("spaghetti calorimeter"). The first modules are 4 cm thick (5.37 radiation lengths or 0.19 interaction lengths [67]), while the seconds modules are 8 cm thick (11.0 radiation length or 0.4 interaction length). The last stage of the electron identifier is a plane of scintillators, used in coincidence with the TOF wall to generate a cosmic-muon trigger to monitor the response of the subdetector.

Figure 9.6 shows the response of the calorimeter to photons, electrons and pions for a beam momentum of 3 GeV/c. Incoming beam electrons and pions are tagged by the beam Cherenkov counters. The entries are dominated by non-interacting beam particles. In the upper plots, the measured x coordinate of the particles is shown. The 'electron' sample also shows radiated photons which go forward along the beam direction whereas electrons and pions are bent by the dipole field of the spectrometer magnet. The lower plots show the expected difference in the energy measured in the electromagnetic calorimeter for electrons and pions.

9.2.6 TOF wall

The scintillator based "TOF wall" detector performs the particle identification for low momentum particles ($p \leq 3.5\,\mathrm{GeV/c}$) in the forward direction, in combination with information on the particle momentum measured by the drift chambers.

In figure 9.7, the mechanical structure of the system is shown: it is composed of a set of 39 scintillation counters, arranged in three vertical walls, each consisting of 13 counters. The TOF wall covers an area of $6.57 \times 2.43\,\mathrm{m}^2$, which guarantees an almost complete geometrical coverage for the particles produced at the target and deflected by the spectrometer magnet [69].

The detector is calibrated in time using both a laser based system and cosmic ray data. A resolution of $\approx$225 ps is reached. In HARP, the time-of-flight of particles

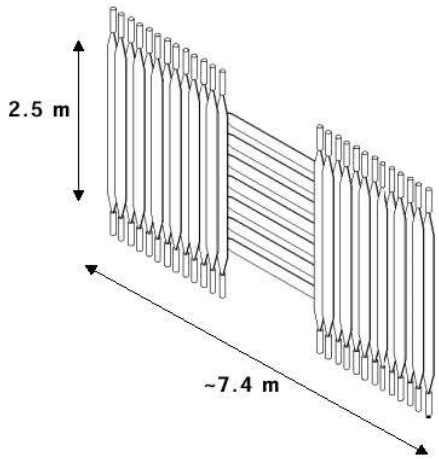

Figure 9.7: Layout of the TOF-wall.

produced at the target is obtained from the difference between the time measured in the TOF wall and in the TOF B counter, located before the target, for a time-of-flight length of aprroximately 10 m. The TOF B counter has an intrinsic time resolution of about 100 ps. The final time resolution on the time-of-flight is expected to be ≈190 ps [69].

After the calibration procedure, the π and p are separated at better than 5σ at 3 GeV/c incident momentum [70], as shown in figure 9.8

9.2.7 Muon identifier

At low energies of the secondary pions and kaons, the decay-in-flight probability is sizable ($\sim$ 5% for pions and $\sim$ 40% for kaons of 2 GeV/c momentum). The decay of these particles can produce a wrong longitudinal and transverse momentum assigment and a possible pion/kaon confusion because of the increase of time-of-flight when a pion decays in the Cherenkov detector.

In addition, beam muons need to be identified since they would lead to a wrong interaction cross-section if accounted as pions.

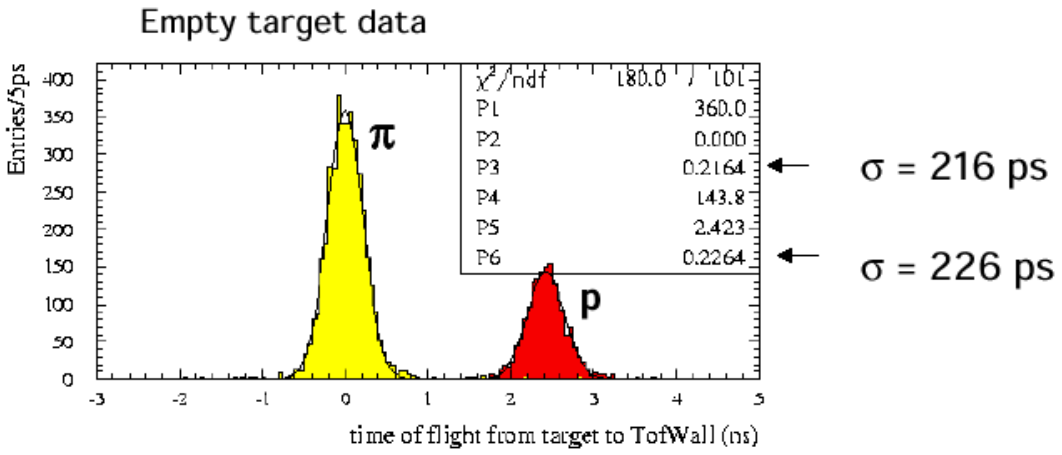

Figure 9.8: Time of flight from the target to the TOF wall for beam protons and pions.

The muon identifier is constituted by a 32 cm layer of iron and by a calorimeter composed by 5 cm thick five iron planes with scintillators sandwiched between them. The detector, whose layout is shown in figure 9.9, is asymmetric in the horizontal direction with respect to the beam line, in order to detect for all beam momenta beam muons which are horizontally deflected by the spectrometer magnet.

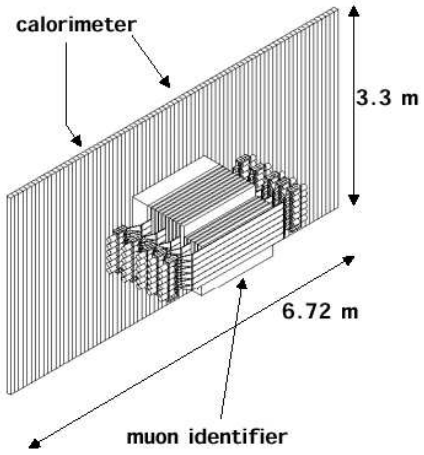

Figure 9.9: Layout of the muon identifier.

9.3 Targets

The HARP target is located inside the TPC, 50 cm downstream of the read-out chamber, in a cylinder surrounded by the inner field cage and the inner trigger chamber (described in the next section) as shown in the figure 9.10.

During the two data taking seasons, solid targets of various materials and thick-

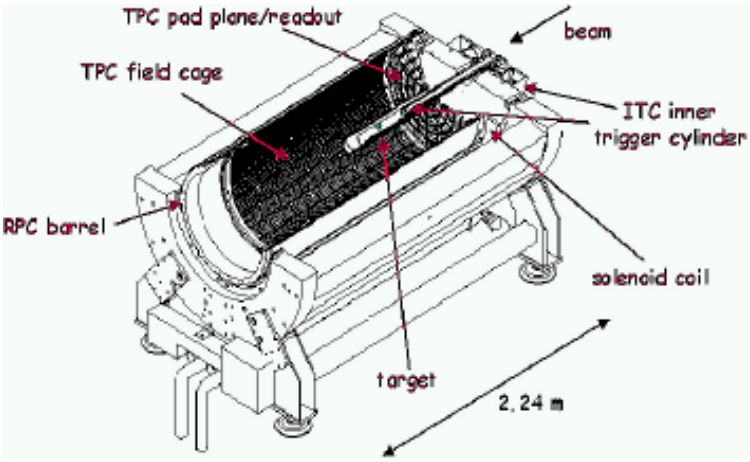

Figure 9.10: Layout of the HARP TPC with the target support.

nesses have been used as well as cryogenic targets. The complete list can be found in table 9.3 together with the beam momentum settings.

The thickness of the targets was chosen to be 2% and 5% of an interaction length ("thin targets") to minimize re-interaction in the target itself while keeping a reasonable interaction rate. A certain number of "thick targets", of 1 interaction length, were used with the aim of checking the simulation of reinteractions. "Button" and "skew" targets were also studied [71].

Dedicated runs with the goal to determine the neutrino yield of the K2K (Al) and MiniBooNE (Be) targets were performed.

Material	Z	A	0.02 λ (cm)	0.05 λ (cm)	1.0 λ (cm)	Comment
Be	4	9.01	0.81	2.03	40.70	
Be	4	9.01				0.5 λ (MiniBooNE)
Be	4	9.01				MiniBooNE target replica
C	6	12.01	0.76	1.90		
Al	13	26.98	0.79	1.98	39.44	
Al	13	26.98				0.5 λ (K2K)
Al	13	26.98				K2K target replica
Cu	29	63.55	0.30	0.75	15.00	
Cu	29	63.55				'button' target
Cu	29	63.55				'skew' target
Sn	50	118.71	0.45	1.13		
Ta	73	180.95	0.19	0.48	11.14	
Pb	82	207.2	0.34	0.85	17.05	
H2	1	1				6 cm
D2	1	2				6 cm
N2	7	14.01				6 cm
O2	8	16.00				6 cm

Table 9.3: Summary of HARP targets

9.4 Trigger

The HARP trigger system can distinguish between physics and calibration events.
A physics event is separated in the trigger logic in "an incoming beam particle" and in secondaries generated over the full solid angle during an "interaction".
The detectors on which the trigger system relies are shown in figure 9.11: they are the TOF-A, TOF-B, Beam Scintillator (BS), Target Defining Scintillator (TDS), HALO-A, HALO-B, BC-A, BC-B on the beam line to select incoming beam particle, and, Inner Trigger PLane (ITC), Forward Trigger Plane (FTP), RPC, Cherenkov to select interactions.
The "halo" counters are scintillators with a hole in the middle, to allow the beam to pass and to veto non collimated particles. The TDS is placed just in front of the

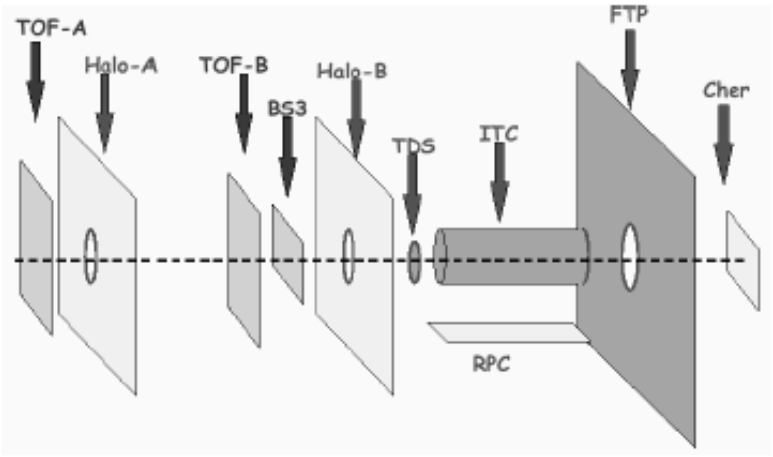

Figure 9.11: The trigger detectors.

target (which has a diameter of 3 cm). The scintillator has a diameter of 2 cm and tags particles that will surely hit the target. The ITC is constituted by scintillating fibers sorrounding the target and detects particles emerging at large angles. The FTP is a vertical plane of scintillators placed after the TPC to detect particles emitted in the forward direction; it has a 6 cm diameter hole in the middle, not to be hit by not interacting particles. The size of the hole is a compromise between the maximum efficiency in detection of secondary particles and insensitivity to non-interacting beam particles.

The physics trigger logic is slightly different depending on the incoming particle momentum and on the kind of target. For thick targets, a physics trigger is given by the "BEAM", defined as BS && TOFB && TOFA && TDS && !(HALOA || HALOB)[1]. This selects a good incoming particle, *i.e.* a particle with a good trajectory that hits the target. As the interaction probability in the thick target runs is high, no additional requirements are added to the trigger condition, so the data are unbiased. For thin targets, when the probability to have an interaction is small, a physics

[1]In the notation used for the trigger conditions, the symbol "&&" means logic *and*, "||" means logic *or*, while "!" means logic *not*

trigger is given by the BEAM×INTERACTION where "INTERACTION" is FTP || ITC. Only events with an interaction and hence secondaries detected at small or large angle are selected. This sample is biased by the request of the interaction. A "down-scale" factor to have unbiased events is applied to provide absolute flux normalisation. The physics trigger condition for thin targets hence is DOWNSCALE || (BEAM×INTERACTION). DOWNSCALE is defined as BS && TOF-B prescaled by a factor of 64 [72]. In this way a sample of unbiased (and tagged) events is added to normal thin target data [73].

At low momentum a high percentage of electrons is present in the beam. These electrons are vetoed by BC-A in a physics trigger.

For calibration purposes, cosmic, pedestal and pulser events have to be taken. For example the TPC cosmic trigger is provided by the RPCs. The triggering signal is given by a coincidence of hits in two opposite RPC modules.

9.5 Data Acquisition

In HARP, 16 VME crates containing the front-end electronics have to be read per event. The software used for the DAQ is DATE [74], a system developed by the ALICE Collaboration.

The basic dataflow architecture is organised along parallel data streams where data are merged and eventually recorded as a complete event. This architecture is depicted in figure 9.12. The LDC (Local Data Concentrator) is a front-end processor present in all VME crates, whose main purpose is to read out the front-end electronics of a given section of the detector. The LDCs manage concurrent streams of data; the triggering system provides the necessary synchronization with the physics events. The LDC data streams are injected on the data-acquisition network (TCP/IP) via an Ethernet switch, through which they reach the GDCs. These two Global Data Collectors are processors that perform the event-building function. They collect the various sub-

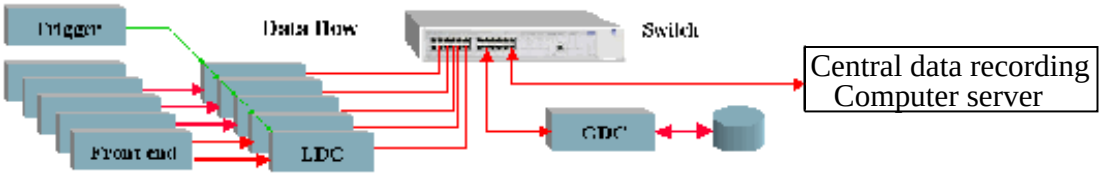

Figure 9.12: Layout of the HARP data flow.

events from the LDCs, put them together and encapsulate them with the proper event structure. They also perform the recording function, by writing the data in files run by run. The files are then merged with information on the run conditions and settings and sent to an object oriented database system, interfaced with the CERN CASTOR mass storage facility.

Chapter 10

The Time Projection Chamber

10.1 The working principle of a TPC

A Time Projection Chamber is a detector used for tracking, with the aim of measuring three dimensional coordinates for each track point with great accuracy.
It is constituted of two elements: a drift space and a readout chamber. The drift volume has typically a cylindrical shape, it is filled with an appropriate gas mixture, and it is in uniform magnetic and electric fields, both parallel to the cylinder axis. The electric field is generated by a negative high voltage membrane at one end of the chamber and by a cathode plane in the readout chamber close to the other end. The uniformity of the field is obtained using field cages in which parallel conductive strips are kept at decreasing potentials.
The readout chamber, not physically separated by the drift volume, starts with a gating grid, followed by a cathode plane of wires, by sense wires kept at high positive voltage and by a segmented cathode plane on which signals are read.
The primary ionisation produced by charged particles traversing the detector, drift in the electric field toward the ends of the chamber. The magnetic field suppresses the diffusion perpendicular to the field. This is achieved by the action of the magnetic forces on the drifting electrons which, as a consequence spiral around the direction of the magnetic field. An amplification of the primary ionisation take place in proximity

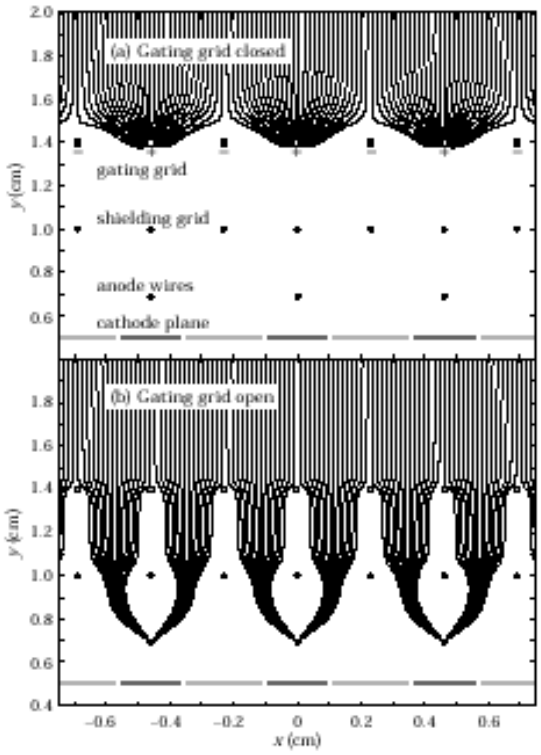

Figure 10.1: Drift paths of electrons in the gate region.

of the sense wires: here the increasing electric field accelerates the primary electrons which produce further ionisation and start an avalanche process. The electrons are collected on the sense wires while the positive ions drift towards the segmented cathode (pad plane) on which they induce a negative signal, on average proportional to the number of the primary electrons. In HARP the wires are not read out. The arrival time of the induced signals on the pads supplies the z coordinate along the cylinder axis when the drift velocity is known.

The signal is usually spread on a few contigous pads, yielding a cluster. The x and y coordinates are obtained from the position of the center of gravity of the cluster.

To prevent field distortions that can be caused by the ions entering in the drift region, a gating grid close to the cathode is used [75]: it is constituted by wires kept at

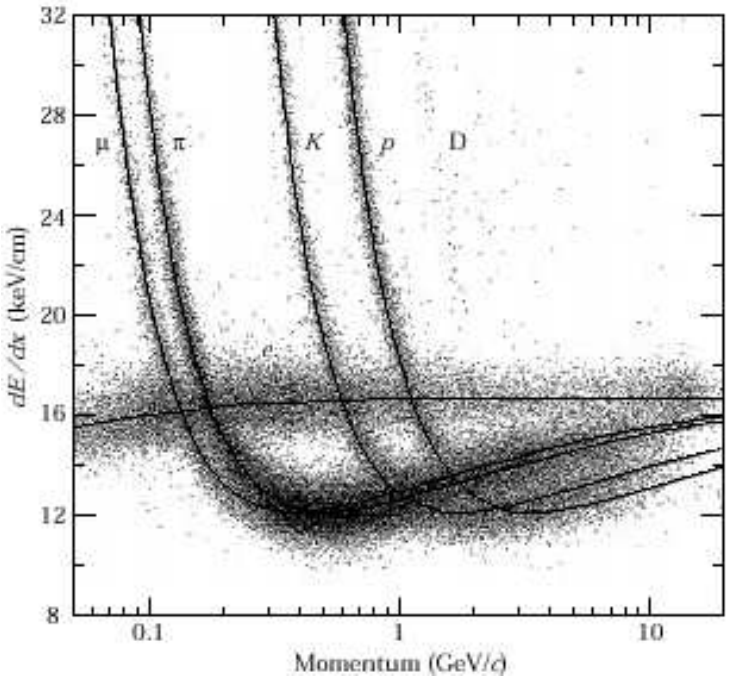

Figure 10.2: dE/dx curves measured with the PEP4/9 TPC.

a potential variing between the nominal one for the plane position, necessary to have a uniform gradient (gate open), and a situation in which neighbour wires are kept at two different voltages alternatively lower and higher than the nominal (gate closed). When there is no trigger, the gate is closed *i.e.* the drifting electrons are collected on the gating grid preventing them to form avalanches outside of the readout period (figure 10.1).

When the gate is opened by a trigger, the electrons pass through the grid towards the amplification region around the anode wires. In this case the grid also act as a barrier for the ions which can move back to the drift volume.

The amplitude of the pad signals as a function of the time is well approximated by a gamma function: $\Gamma = t^2 \exp(-t)$ where the time t has to be offset by the time at which the electrons arrive at the anode wires and scaled by a factor which depends on

the shaping time of the electronics, the longitudinal diffusion of ionisation electrons in the gas and on the track inclination and the radial extent of the pads.
The distribution of the charge induced on the pads as a function of the transverse distance between the center of the pad and the ion cloud, is the pad response function, described by a Gatti- Mathieson function [77].
A TPC with magnatic field allows to determine the momentum of charged particles from the determination of the parameters of the helicoidal trajectory they will follow, as will be described in the following chapter. Multiple measurements of dE/dx. along the particle trajectory, combined with the momentum information, also allow to identify pions, kaons and protons at low momenta as shown in the figure 10.2.

10.2 Layout of the HARP TPC

The central tracker of HARP is the Time Projection Chamber, inside which the target is located. The TPC is situated inside a solenoid magnet which gives a magnetic field of 0.7 T, parallel to the z axis.
The drift volume is a cylinder 1.5 m long and with a radius of ≈ 40 cm, filled with a mixture of Ar (90%) and methane (10%) at atmospheric pressure.
The layout of the field cages is shown in figure 10.3: at the right end there is a high voltage membrane, kept at (-30 kV); at the left end there is the readout chamber. The field cages are made of an outer and inner Stesalit (a plastic fiber) cylinders on which are located a first layer of potential rings and second layer of metallised Mylar strips. The inner field cage cylinder, that contains the target, has a radius of 5 cm, hence the TPC cannot detect track segments in its central region.
A schematic drawing of the readout chamber and a sector of the pad plane are presented in figure 10.4.

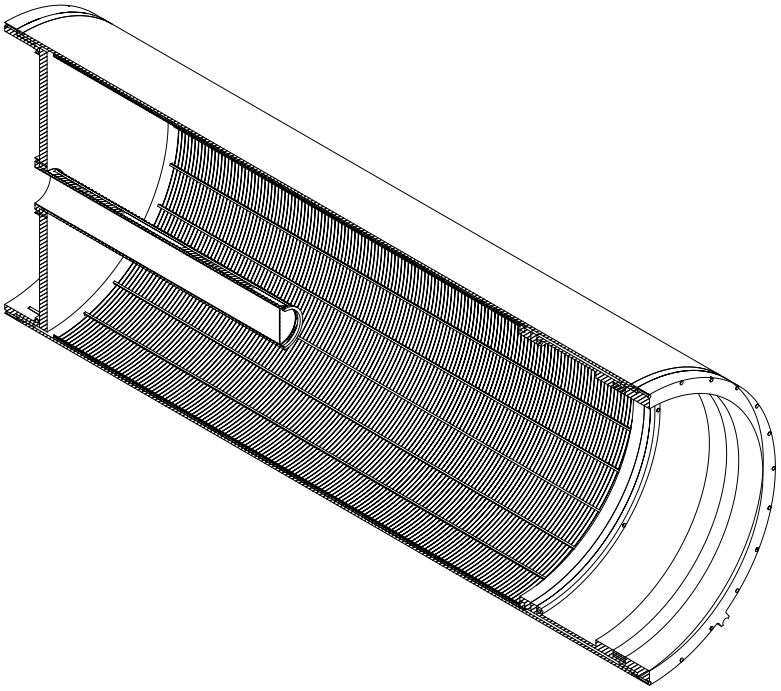

Figure 10.3: Layout of the TPC field-cage.

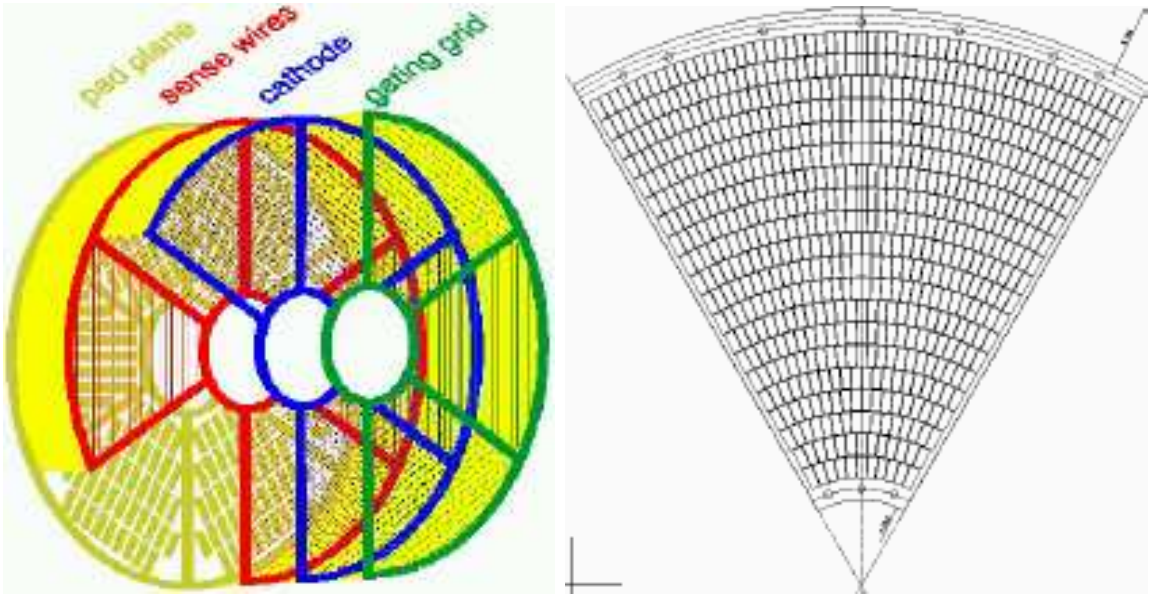

Figure 10.4: Schematic drawing of the HARP TPC read-out chamber (left) and of a sector of the pad plane (right).

In HARP the wires of the gating grid are kept at the nominal potential $\pm 35\,\mathrm{V}$ when the gate is closed. The cathode and the pad plane are grounded, while the sense wire plane is kept at $+1.5\,\mathrm{kV}$.

The pad plane contains approximately 4000 pads, arranged in 20 concentric rows. The average pad size is $6.5\,\mathrm{mm} \times 15.5\,\mathrm{mm}$.

The pad plane is an electronic printed circuit board which contains also the preamplifiers for each pad. Here the signal coming from the pads is shaped and then sent via special flex cables to a daughter card, which is in turn connected to ADCs.

The ADCs are sampled with a 10 MHz clock frequency.

10.3 TPC performance

With the HARP gas mixture, the transverse diffusion is of $208\,\mu\mathrm{m}\sqrt{\mathrm{drift(cm)}}$ per cm of drift [78]. Transverse diffusion makes some ionisation electrons from the track drift to pads neighbouring the one the would have been hit in the absence of diffusion. Over the maximum drift distance of 150 cm, the dispersion reaches 2.5 mm.

Longitudinal diffusion increases the width of the time distribution of the signals. The HARP gas has a longitudinal diffusion coefficient of approximately $380\,\mu\mathrm{m}$ per cm of drift [78] and a drift velocity of $5.2 cm/\mu\mathrm{s}$. Over the maximum drift distance of 150 cm, this leads to a dispersion of $\approx$100 ns. This diffusion only affects tracks that are parallel with the pad plane.

The pads are designed to have a resolution in $r-\phi$ (in the $X-Y$ plane) of $300\,\mu\mathrm{m}$ [43]. The Gluckstern formula[1] gives, with a magnetic field of 0.7 T and 21 samplings, a p_t resolution of

$$\Delta p_t/p_t = 0.07 p_t. \tag{10.1}$$

Unfortunately, after a first analysis of TPC data, they have been found to be affected by cross-talk. In particular, in absence of cross talk, the signal shape in time should

[1] $\Delta p_t/p_t = \sigma_{r\phi}/(0.3\,B\,L^2)\sqrt{720/(N+4)}\,p_t$ [GeV/c]

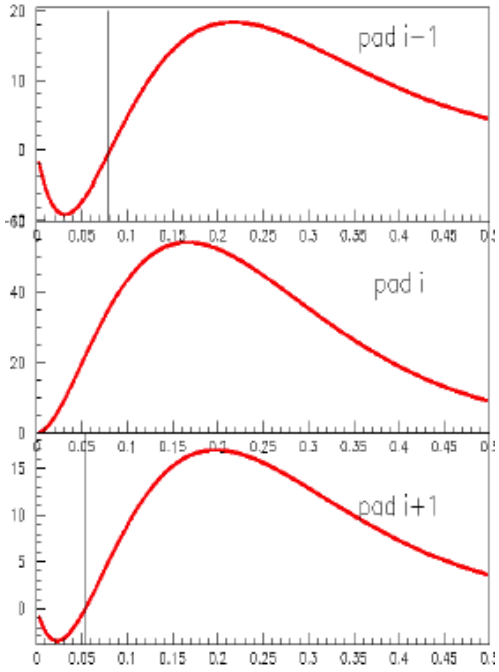

Figure 10.5: Signals on the leading (middle) and on satellite pads (upper and lower) obtained injecting short charge pulses.

be a gamma function with a larger amplitude for the leading pad, and a smaller amplitude on the satellite pads on which the charge is also induced. What is instead observed very often in TPC data, is shown in figure 10.5: the "pad i" is the leading pad and the its pulse reaches the maximum after approximately 150 ns; the signals on the satellite pads (i-1 and i+1) show a negative component at the beginning, and then reach the maximum at approximately 200 ns. The cross-talk is explained by a capacitive coupling between the preamplifier output of one pad and the preamplifier input of another pad [79]. It clearly affects the charge distribution across pads and therefore the spatial resolution in the $X - Y$ plane and the $\mathrm{d}E/\mathrm{d}x$ resolution.

The cross-talk effect will be corrected a posteriori via software, using a map of cross talk between pads obtained by injecting short pulses of charge into one pad and studying the response of the satellite pads.

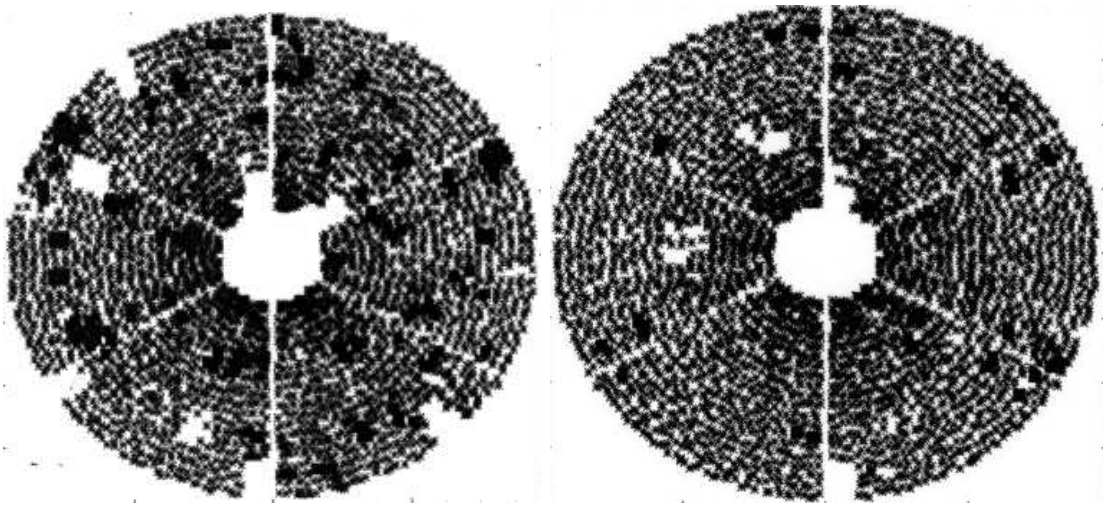

Figure 10.6: TPC active pads in 2001 (left) and 2002 (right).

An other problem suffered by the TPC in the 2001 data taking period has been that approximately the 5% of the pads were not functional: a part of them was "dead" because of problems due to the readout micro flex cables, and a part was very noisy because of interference effects in the voltage supplies of the preamplifier chips. During the winter shutdown between the 2001 and 2002 data taking periods, the problems were solved and a better data quality is expected for 2002 data compared with 2001. Figure 10.6 shows a map of the TPC active channels in the two seasons.

The TPC spatial resolution, measured using cosmic ray data taken in the 2001 run, was of approximately 2 mm in $r-\phi$ and 3 mm in Z [80] as shown in figure 10.7. These values are far from the project ones but they are expected to improve as soon as the cross-talk problem will be solved.

10.4 Laser calibration

The TPC has been continuously calibrated using shots of laser light into the gas volume at the high-voltage membrane, at precisely known locations.

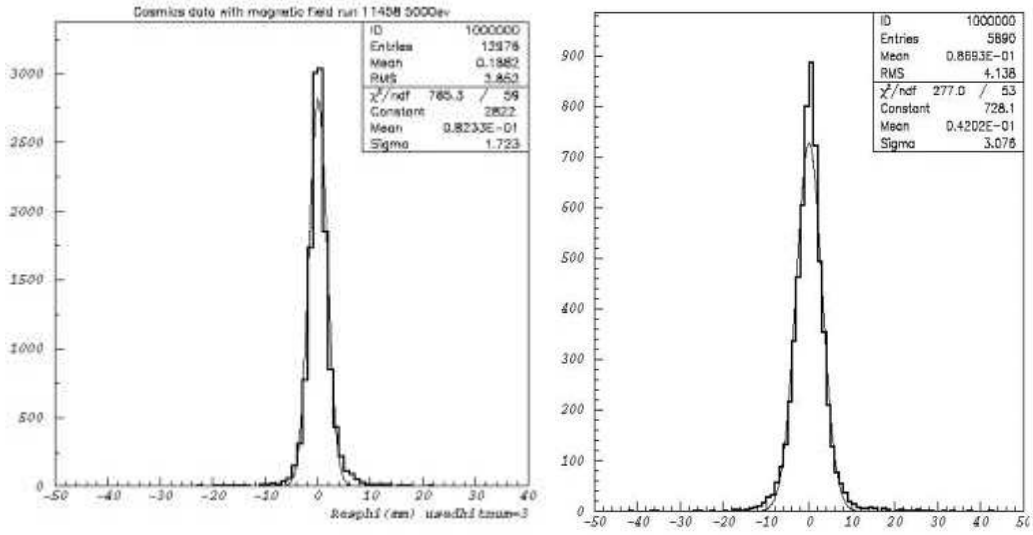

Figure 10.7: Residual distributions in $R-\phi$ (left) and Z (right).

Laser light produces ionisation and the corresponding signal is studied. This method is very useful to understand whether field inhomogeneities causing distortion of the drift path from a straight line are present and to accurately measure the drift velocity of the electrons.

At the time of writing, preliminary studies on the position of the cluster associated to the laser shot reveal a possible electric field inhomogeneity. Nevertheless, the observed shift can be due to the not (yet!) perfect pad gain equalisation or to cross talk effects [81].

Knowing the exact time at which the laser pulses, it is possible to measure the drift of the photoelectrons, which is a fundamental parameter for the z coordinate reconstruction ($z = v_{drift} \cdot t$).

The figure 10.8 shows the measured pulse amplitude as a function of the signal arrival time. This is in line with the expectation from the 100 ns digitisation intervals, folded with longitudinal diffusion in the gas and the preamplifier response function [68]. The drift velocity is estimated to be $(5.173 \pm 0.013)\,\mathrm{cm}/\mu\mathrm{s}$.

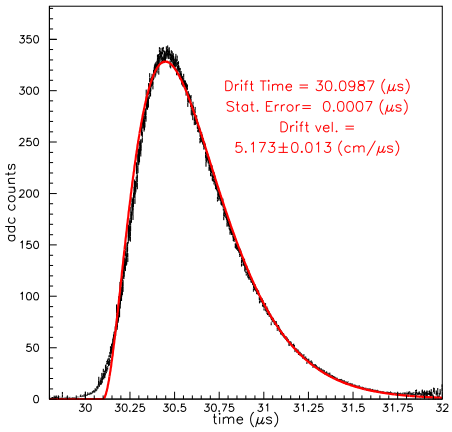

Figure 10.8: Pulse amplitude vs time of laser signals.

10.5 The HARP TPC software reconstruction chain

In order to extract physics information such as momentum, particle identity and trajectory from the raw data, it is necessary to perform a series of steps, namely the pad gain equalisation, the ionisation cluster finding, the track finding and fitting. This is accomplished by a series of algorithms, written in the GAUDI [85] framework. The logic data flow is schematically represented in the figure 10.9.

All the steps preceding the track fit are described in the following subsections, while the algorithm performing the fit and the momentum and charge reconstruction will be described in detail in the next chapter, as it represents my personal contribution to the HARP experiment.

10.5.1 Pad gain equalisation

As already explained, the amplitude of the signal on the pads should be on average proportional to the number of primary electrons. The proportionality constant is the pad gain. Due to variations in the electronics as well as construction factors such as

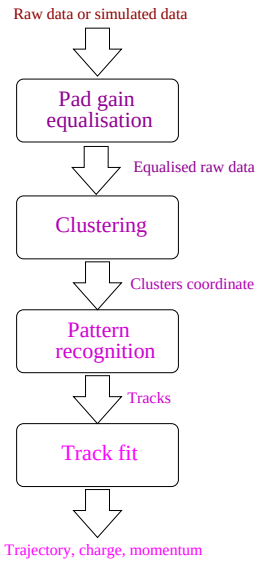

Figure 10.9: Logic flow of the HARP TPC reconstruction chain.

wire sag, the various pads show different gains. This is pernicious to the following analysis of data, as it can determine a wrong assignment of coordinates to the clusters, and worsen the dE/dx measurements. It is therefore necessary to equalise the signals coming from the different pads. This is done in HARP using two different techniques, cosmic rays and radioactive Krypton, exposed in the following subsections.

Cosmic

The method is based on the assumption that cosmic rays events should deposit approximately equal amounts of charge on each pad. For the central limit theorem, the mean of the charge distribution should, for each pad, converge to a fixed value for a large number of entries. This value is the equalisation constant of the pad [82].
An algorithm to extract the equalisation constant from cosmic ray events has been developed, and its result is the equalisation map shown in the figure 10.10. This algorithm is the first step of the TPC software reconstruction chain.

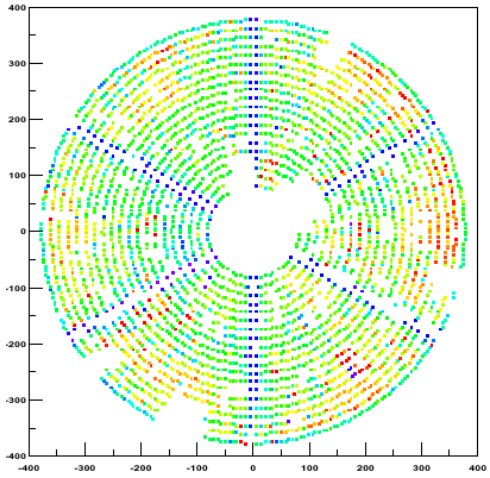

Figure 10.10: Colour map of the TPC pad plane showing the equalisation constants from the cosmic ray equalisation method.

Krypton

Radioactive ^{83}Kr gas injected in the TPC volume deposits ionisations via several mechanisms: internal conversion electrons, Auger electrons and photons with a total energy of 9.4 keV, 12.6 keV, 19.6 keV, 29 keV or 41.6 keV (figure 10.11).

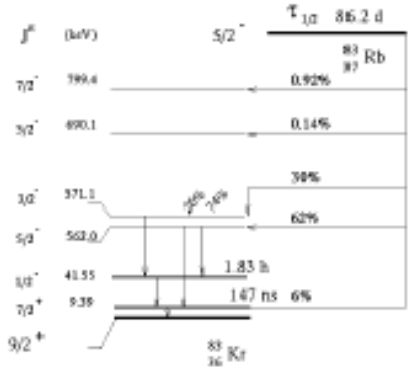

Figure 10.11: Decay scheme of ^{83}Ru and ^{83}Kr

The spectrum of these processes can be reconstructed in the pads, and yields the

calibration coefficients. In figure 10.12 the krypton spectrum obtained both using the Krypton equalisation constants and the cosmic ones is shown. The two methods have compatible results.

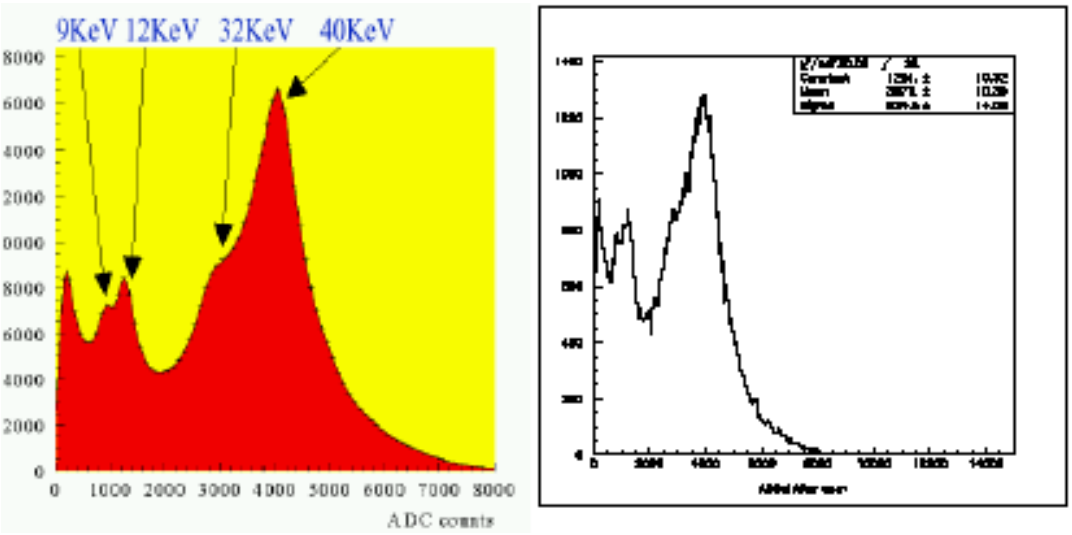

Figure 10.12: Krypton spectrum obtained with (left) Kr equalisation method and (right) cosmic method.

10.5.2 Clustering

The aim of the "clustering" algorithm is to define and assign three dimensional coordinates to signals detected in the TPC [83]. It takes as input the equalised ADC signals and its output is constituted by the x, y, z coordinates and the total charge of the clusters.

The first step is the "hit" definition for each pad. The $x - y$ position of the hit is simply given by the pad centre location, while the z coordinate has to be estimated from the signal shape. The z estimator should have minimal sensitivity to the track inclination and have the smallest RMS possible. The z position of the hit is hence defined as $z = t \cdot v_{drift}$, where the time t is chosen to be the time corresponding to

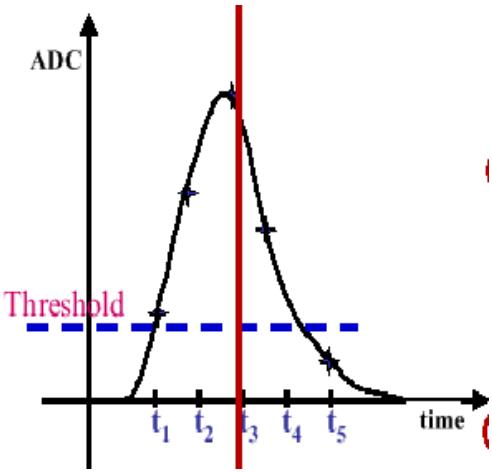

Figure 10.13: Schematic of the ADC signal as a function of the time. For the clustering purposes the interesting signal is above the threshold and up to the maximum value.

the 50% of the maximum ADC value obtained during the readout period. Then the clusters have to be found. Different pads are considered to belong to a cluster if they are neighbours in a row (with the exception for dead and noisy) and if their signals are overlapped or close in time. The cluster position is given by the centre of gravity coordinate of the hits, weighted by their ADC value. The ADC value of a pad is given by the sum of the ADC values exceeding a fixed threshold at consecutive time samples, as illustrated in figure 10.13.

The sum is cut when the signal reaches its maximum in order not to take into account the tail, related to the cross-talk delayed signal.

10.5.3 Pattern Recognition

The pattern recognition algorithm aims to recognise tracks. It takes as input the cluster coordinates and its output are the tracks,*i.e.* groups of clusters recognised as belonging to the same track [84].

The algorithm does not assume the actual helicoidal shape of the tracks. It first

establishes "links" between points. As the tracks are supposed to be less dense in the outer region of the TPC, the search of clusters to be added to these links starts using the links of the outer region as seeds. The line connecting the first two points is followed toward the detector axis. When a cluster is located in the volume of a truncated cone with the axis along this line, it is added to the track candidate. The parameters of the cone as radius, opening angle and forward acceptance (figure 10.14) have been optimised to achieve a maximum track finding efficiency for particles with momentum greater than 100 MeV/c.

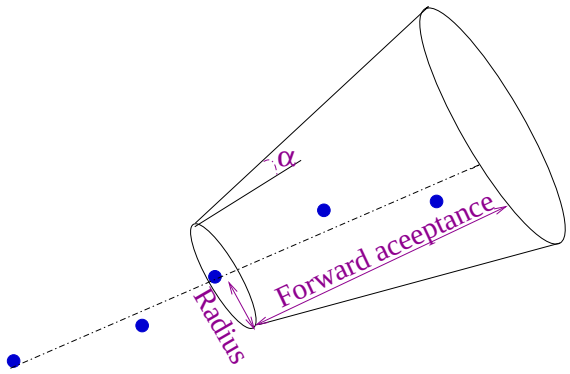

Figure 10.14: Parameters of the pattern recognition algorithm.

Chapter 11

The TPC helix fit and momentum reconstruction algorithm

11.1 Introduction

A helicoidal trajectory results whenever a charged particle moves in a constant magnetic field. This is the case in the HARP Time Projection Chamber. In the TPC, the magnetic field goes along the Z axis of the HARP reference system. The trajectory of the charged particles will be therefore a helix with the axis parallel to the Z axis. Its projection in the X-Y plane will be a circle and the Z displacement will be proportional to the length of the arc described in the X-Y plane, called s_{xy}. Therefore the particle trajectory in the $s_{xy} - Z$ plane is a straight line.

11.2 The parameters describing a helix

A helix is described by five parameters. One possibility is to use the following ones, out of which the first tree are defined in the $X - Y$ plane and the other two in the $s_{xy} - Z$ plane:

- $\rho = 1/R$, the inverse of the radius of curvature. This parameter has a sign: positive if, seen from the origin, the track bends clockwise; negative if it bends

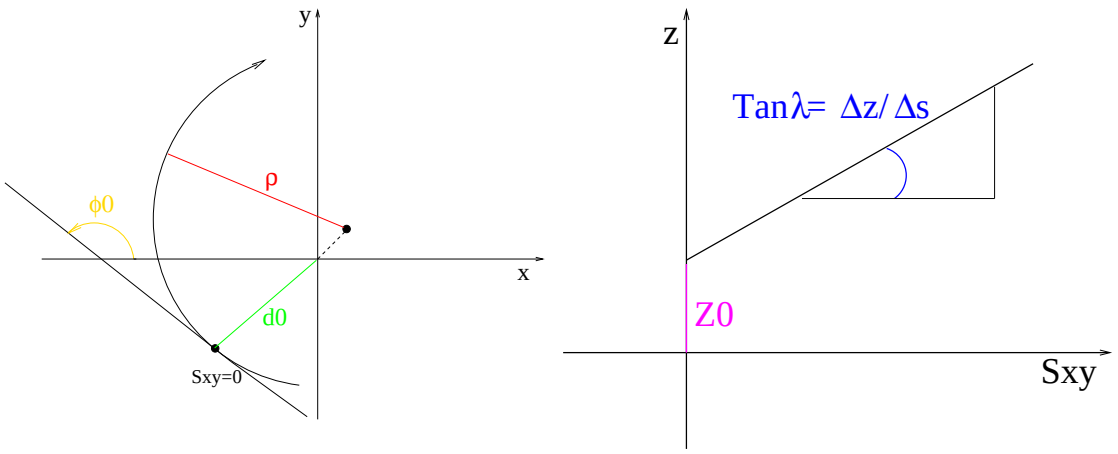

Figure 11.1: Helix parameters used in the fitting algorithm. In the particular case shown ρ and d_0 are positive.

anti-clockwise

- d_0, the impact parameter in the $X-Y$ plane. It has positive sign if the Z axis is inside the helix, negative if it is outside.
- ϕ_0 the angle between the projection on the $X-Y$ plane of the particle momentum at the impact point and the X axis
- tanλ=dz/ds_{xy}, the tangent of the dip angle
- z_0 the z coordinate at the impact point where $x^2+y^2=d_0^2$.

The five variables are sketched in figure 11.1.

11.3 General fitting procedure

The fitting algorithm "FitTpcTracksAlg" takes as input the tree dimensional coordinates (x_i, y_i, z_i) of the clusters that the pattern recognition assigns to a track. It has to be pointed out that the pattern recognition algorithm doesn't look for helix

candidates, but rather builds links between points in a defined region.

The goal of the fitting algorithm is to determine the parameters describing the helix that better fit these points and that will be used to measure the momentum of the particle.

The fit is performed in two consecutive steps [86]: the first is a circular fit in the $X-Y$ plane that allows to determine ρ, d_0 and ϕ_0, the second performs the linear fit in the s_{xy}-Z plane and calculates tanλ and z_0.

The parameters giving lengths are expressed in millimetres and the angles in radians.

11.4 The circle fit in the $X-Y$ plane

For n points given in a plane by their coordinates (x_i, y_i), it is necessary to draw the circle

$$(x-a)^2 + (y-b)^2 = R^2, \tag{11.1}$$

minimising the mean square distance from the given points to this circle.

It is useful to introduce a new variable, $\nu = x^2+y^2$, in the circle equation to transform it into a linear equation and then apply a linear regression method. The new equation becomes:

$$\nu = \alpha x + \beta y + \gamma, \tag{11.2}$$

where $\alpha = 2a, \beta = 2b, \gamma = R^2 - a^2 - b^2$ are treated as the unknown parameters in the linear regression.

The problem is equivalent to minimise the function:

$$M(a,b,R) = \sum_{i=1}^{n} \left((x_i - a)^2 + (y_i - b)^2 - R^2 \right). \tag{11.3}$$

It has been found [87] that the computation accuracy can be improved by transferring the origin of the coordinate to the centre of gravity of the points and by minimising

the alternative function $K(a,b,R) \equiv M(a,b,R)R^{-2}$:

$$K(a,b,R) = \sum_{i=1}^{n} \left(\frac{x_i^2 + y_i^2}{R} - 2\frac{a}{R}x_i - 2\frac{b}{R}y_i + \frac{a^2 + b^2 - R^2}{R} \right)^2 \tag{11.4}$$

Equating to zero the derivatives of the functional (11.4), a second order nonlinear system of equations is obtained:

$$\begin{aligned} Fa + Hb - a\gamma &= P \\ Ha + Gb - b\gamma &= Q \\ 2Pa + 2Qb + \gamma^2 &= T \end{aligned} \tag{11.5}$$

Using the Gauss brackets notation, $\sum_{i=1}^{n} x^p y^q = [x^p y^q]$, the coefficients in the system are defined as:

$$\begin{aligned} F = \frac{1}{n}[3x^2 + y^2], \quad G = \frac{1}{n}[x^2 + 3y^2] \\ H = \frac{2}{n}[xy], \quad P = \frac{1}{n}[x(x^2 + y^2)] \\ Q = \frac{1}{n}[y(x^2 + y^2)], \quad T = \frac{1}{n}[(x^2 + y^2)^2] \end{aligned}$$

Then, by eliminating the unknown a and b in the system (4.5), a fourth degree equation in the remaining unknown variable γ is obtained:

$$\gamma^4 + \gamma^3(-F - G) + \gamma^2(FG - T - H^2) + \gamma[T(F + G) - 2(P^2 + Q^2)] + W \tag{11.6}$$

where $W = T(H^2 - FG) + 2(P^2G + Q^2F) - 4PQH$.

The previous equation is solved iteratively using the Newton method with an accuracy of 10^{-16}.

Once γ is known, the parameters a, b, and $|R|$ can be easily calculated.

The sign of R remains to be determined. To accomplish that, the asymmetry of the experimental points is evaluated defined as:

$$Asym = \frac{a}{|R|} * Ycg - \frac{b}{|R|} * Xcg, \tag{11.7}$$

where X_{cg} and Y_{cg} are the coordinates of the centre of gravity of the points, in which the origin has been translated to perform the circular fit. The sign of R is positive if the asymmetry is positive, *i.e.* if, seen from the origin, the track bends clockwise, and is negative otherwise.

The helix parameters ϕ_0 and d_0 can be evaluated using the following formulas:

$$\phi_0 = \arcsin\left(-\frac{a}{\sqrt{a^2+b^2}}\right) + \frac{\pi}{2} + (\frac{R}{|R|} - 1)\frac{\pi}{2} \quad \text{for } b > 0$$
$$\phi_0 = 2\pi - \left[\arcsin\left(-\frac{a}{\sqrt{a^2+b^2}}\right) + \frac{\pi}{2} + (\frac{R}{|R|} - 1)\frac{\pi}{2}\right] \quad \text{for } b < 0 \tag{11.8}$$

$$d_0 = |R| - \sqrt{a^2+b^2} \tag{11.9}$$

11.5 The convention on the direction of motion

Following reference [88] and defining the $\delta\psi$ as the angle between the projection on the $X-Y$ plane of the particle momentum at the generic point and the one at the impact point (figure 11.2), it is possible to parametrise a helix using the following

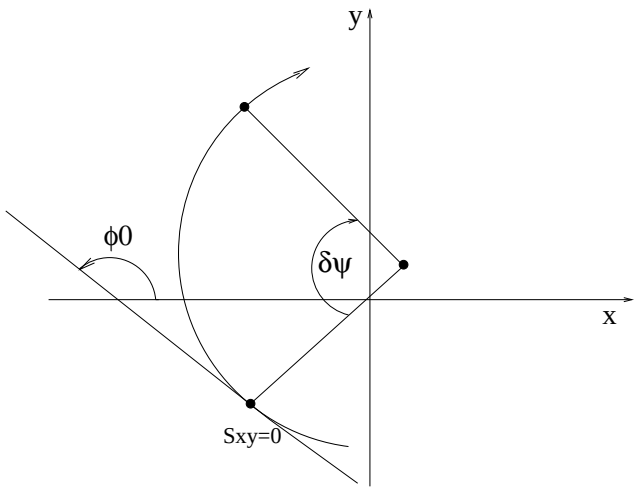

Figure 11.2: The ψ angle.

equations:

$$x = A\cos(\phi_0 - \frac{R}{|R|}\frac{\pi}{2}) - R\sin(\phi_0 + \delta\psi) \quad (11.10)$$

$$y = A\sin(\phi_0 - \frac{R}{|R|}\frac{\pi}{2}) + R\cos(\phi_0 + \delta\psi) \quad (11.11)$$

$$z = z_0 - R\tan\lambda\,\delta\psi \quad (11.12)$$

with $A = |R| - d_0$.

The parametrisation is consistent with the already mentioned convention on the sign of R and describes a helix that "moves forward" when the value of $-R\delta\psi$ increases and, depending upon the sign of R, screws clockwise ($R > 0$) or anti-clockwise ($R < 0$). This feature can be simply checked:

there are four cases, according to the signs of R and d_0.

1. $d_0 > 0$ and $R > 0$. (Figure 11.3)

   The specific case $\phi_0 = \pi/2$ is illustrated. In this case,

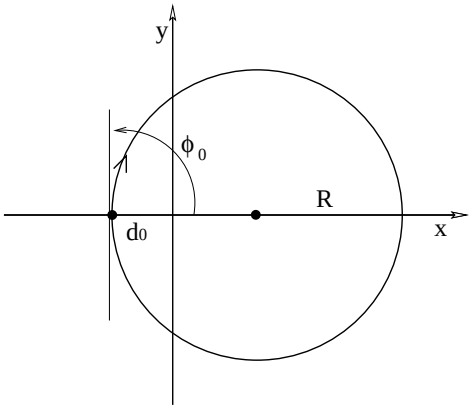

Figure 11.3: The case of d_0 and R positive.

$$x = |R| - d_0 - R\sin(\frac{\pi}{2} + \delta\psi)$$

$$y = R\cos(\frac{\pi}{2} + \delta\psi)$$

or, equivalently,

$$\begin{aligned} x &= |R| - d_0 - R\,\cos(\delta\psi) \\ y &= -R\,\sin(\delta\psi). \end{aligned}$$

The point $\delta\psi$=0 gives $x = -d_0$ and $y = 0$.

Considering now $\delta\psi < 0$ (so that $-R\delta\psi > 0$) and infinitesimal

$$\begin{aligned} x &\simeq -d_0 + R\frac{(\delta\psi)^2}{2} \\ y &\simeq -R\,\delta\psi. \end{aligned}$$

i.e. the point moves clockwise.

2. $d_0 > 0$ and $R < 0$ (Figure 11.4)

   Note that in this case the tangent that determines the value of ϕ_0 is oriented

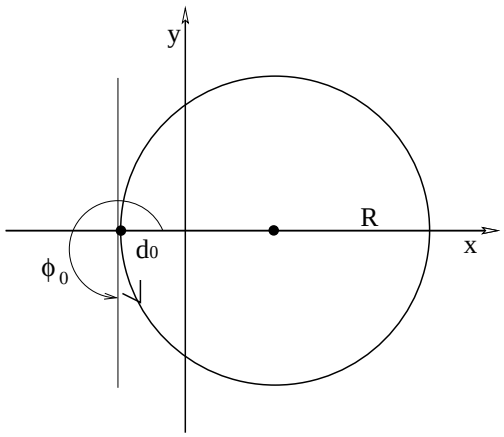

Figure 11.4: The case $d_0 > 0$ and $R < 0$.

in the opposite way and the case which can be compared to the previous one is $\phi_0 = \pi/2 + \pi = 3/2\pi$. One obtains:

$$x = |R| - d_0 - R\,\sin(\frac{3\pi}{2} + \delta\psi)$$

$$y = R\cos(\frac{3\pi}{2} + \delta\psi)$$

i.e.

$$\begin{aligned} x &\simeq |R| - d_0 + R\cos(\delta\psi) \\ y &\simeq R\sin(\delta\psi). \end{aligned}$$

The point $\delta\psi = 0$ gives $x = |R| + R - d_0 = -d_0$ and $y = 0$. For small $\delta\psi > 0$ (as $-R\,\delta\psi > 0$ always), in this case

$$\begin{aligned} x &= -d_0 - R\frac{(\delta\psi)^2}{2} \\ y &= R\,\delta\psi. \end{aligned}$$

i.e. the point moves anti-clockwise.

3. $d_0 < 0$ (Figure 11.5)

   In the previous two cases ($d_0 > 0$), the formulas were obtained without assuming a specific sign for d_0: this only enters in the drawing of the circle with respect to the origin. In the case of $d_0 < 0$ the circle is external to the origin but the arguments concerning the direction on the motion still hold.

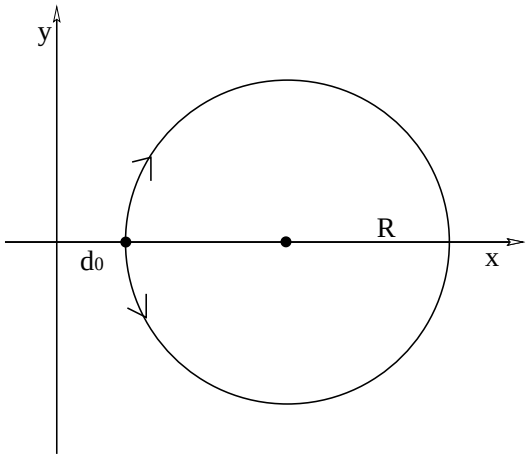

Figure 11.5: The case with $d_0 < 0$.

11.6 The linear fit in the $s_{xy} - Z$ plane

The second part of the algorithm "FitTpcTracksAlg" performs, as already mentioned, a linear fit in the s_{xy}-Z plane to get the last two helix parameters, tanλ and z_0.
The relation of the linear fit is:

$$z = z_0 + \tan\lambda \, s_{xy} \tag{11.13}$$

To perform the linear fit (which is done using the least square method), one has to calculate the value of s_{xy} of the experimental points. This is the crucial part of the code.
The value of s_{xy} ($s_{xy} = -R\delta\psi$) has to be calculated from the knowledge of R, d_0 and ϕ_0. It can be related to $r^2 = x^2 + y^2$, the distance from the origin in the $X - Y$ plane of the experimental points, which is known.

$$r^2 = (a - R\,\sin(\phi_0 + \delta\psi))^2 + (b + R\,\cos(\phi_0 + \delta\psi))^2 \tag{11.14}$$

where

$$\begin{aligned} a &= (|R| - d_0)\cos(\phi_0 - \frac{R}{|R|}\frac{\pi}{2}) \\ b &= (|R| - d_0)\sin(\phi_0 - \frac{R}{|R|}\frac{\pi}{2}) \end{aligned}$$

By playing with the equation (11.14) one gets $\delta\psi$:

$$\begin{aligned} r^2 &= a^2 + b^2 + R^2\,\sin^2(\phi_0 + \delta\psi) + R^2\,\cos^2(\phi_0 + \delta\psi) \\ &\quad -2aR\,\sin(\phi_0 + \delta\psi) + 2bR\,\cos(\phi_0 + \delta\psi) \\ &= (|R| - d_0)^2 + R^2 + 2R(|R| - d_0)\cdot \\ &\quad [\cos(\phi_0 + \delta\psi)\sin(\phi_0 - \frac{R}{|R|}\frac{\pi}{2}) - \sin(\phi_0 + \delta\psi)\cos(\phi_0 - \frac{R}{|R|}\frac{\pi}{2})] \\ &= (|R| - d_0)^2 + |R|^2 + 2R(|R| - d_0)\sin(\phi_0 - \frac{R}{|R|}\frac{\pi}{2} - \phi_0 - \delta\psi) \end{aligned}$$

but

$$\sin(-\frac{R}{|R|}\frac{\pi}{2} - \delta\psi) = -\sin(\frac{R}{|R|}\frac{\pi}{2} + \delta\psi) = \begin{cases} -\cos\delta\psi & \text{if } R > 0 \\ +\cos\delta\psi & \text{if } R < 0 \end{cases}$$

$$\begin{aligned} &= (|R| - d_0)^2 + |R|^2 - 2\frac{R^2}{|R|}(|R| - d_0)\cos\delta\psi \\ &= (|R| - d_0)^2 + |R|^2 - 2|R|(|R| - d_0) + 2|R|(|R| - d_0)(1 - \cos\delta\psi) \\ &= d_0^2 + 4|R|(|R| - d_0)\sin^2(\frac{\delta\psi}{2}) = r^2. \end{aligned} \tag{11.15}$$

From equation (11.15) the final expression reads:

$$\sin\frac{\delta\psi}{2} = \pm\sqrt{\frac{r^2 - d_0^2}{4|R|(|R| - d_0)}} \tag{11.16}$$

It is now proved that the quantity under the square root is not negative.

- $r^2 - d_0^2 \geq 0$: indeed, d_0 it is the distance from the origin of the impact point, by definition the closest to the origin of the helix points.
  If $d_0 = |R|$ the circle is centred at the origin and $r^2 = d_0^2$.

- $|R| - d_0 \geq 0$

  1. if $d_0 < 0$ the origin is outside the circle (refers to figure 11.5).
     In this case, $|R| - d_0 = |R| + |d_0| > 0$.

  2. if $d_0 > 0$ the origin is inside the circle (refers to figures 11.3 and 11.4), and by definition $d_0 < R$

The extraction of $\delta\psi$ from equation (11.16) presents two problems: the sign must be chosen and the arcsin must be defined beyond the "first branch" of the function.
The problem of the sign ambiguity can be solved in the following way. It is known that

$$\frac{\delta\psi}{2} = \pm\arcsin\frac{1}{2|R|}\sqrt{\frac{r^2 - d_0^2}{(1 - d_0/|R|)}} \tag{11.17}$$

and that

$$s_{xy} = -R\delta\psi = \mp 2R \arcsin \frac{1}{2|R|}\sqrt{\frac{r^2 - d_0^2}{(1 - d_0/|R|)}}. \tag{11.18}$$

However, $-R\delta\psi > 0$,

$$\delta\psi > 0 \quad \text{for } R < 0$$

$$\delta\psi < 0 \quad \text{for } R > 0$$

a condition that can incorporated into $\delta\psi$ by defining

$$\delta\psi = -2 \arcsin(\frac{1}{2R}\sqrt{\frac{r^2 - d_0^2}{1 - d_0/|R|}}). \tag{11.19}$$

Now, no matter what R is, the sign ambiguity is solved and s_{xy} is always growing and positive beyond the impact point. It is given by:

$$s_{xy} = 2R \arcsin(\frac{1}{2R}\sqrt{\frac{r^2 - d_0^2}{1 - d_0/|R|}}), \tag{11.20}$$

or, by the simpler formula:

$$s_{xy} = 2|R| \arcsin(\frac{1}{2|R|}\sqrt{\frac{r^2 - d_0^2}{1 - d_0/|R|}}). \tag{11.21}$$

The equation (11.13) says that $s_{xy} = 0$ at $z = z_0$ (the impact point). The TPC tracks however can start either after ($s_{xy} > 0$) or before ($s_{xy} < 0$) the impact point. The value of s_{xy} extracted by its definition is always positive and the expression must be modified to account for tracks starting before the impact point, as it will be discussed in the next section.

11.7 The reconstruction of s_{xy} in the case $R > 0$

Let us now come to the second problem mentioned in section 4.6: the reconstruction of the arcsin for values of $|\delta\psi|$ greater than π.

"func" is defined as the argument of the arcsin *i.e.*, from eq (11.20), func=sign(R)$|\sin(\psi/2)|$.

Then the following hypothesis for the reconstruction of s_{xy} is assumed: the value of $-R\delta\psi$ of the first point is smaller than πR and bigger than $-\pi R$. The hypothesis implies that the first point is either in zone A or in zone B of figure 11.6. Zone A

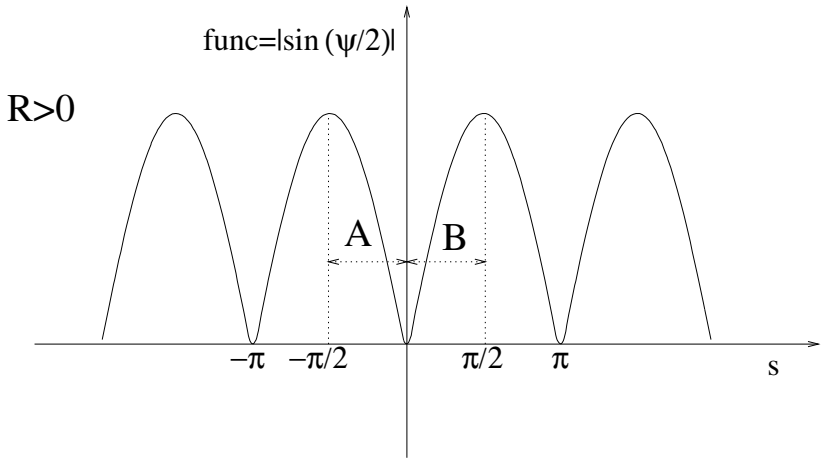

Figure 11.6: The $func$ behaviour as a function of s in the case of $R > 0$.

corresponds to negative s_{xy}/2R, i.e. to a value of s_{xy} before the impact point, while zone B corresponds to a positive s_{xy}/2R, beyond the impact point. They can be distinguished by the decreasing (A) or increasing(B) behaviour of *func*. Notice that, by mistaking the regions, one would pick up a point differing in $\delta\psi$ by a multiple of 2π and therefore having the correct tanλ and a different z_0.

The transition from zone A to zone B is characterised by the changing behaviour of *func*, as well as the exit from zone B. The program takes care of the different zones to correctly reconstruct the secondary branches of the arcsin.

11.7.1 The reconstruction of the branches

The code calculates s_{xy} as:

$$s_{xy} = 2R[\epsilon \arcsin(func) + (1-\epsilon)\frac{\pi}{2} + phase\,\pi] \equiv 2Rs \tag{11.22}$$

When the position of the first experimental point is in zone "A" of figure (11.6), *func*

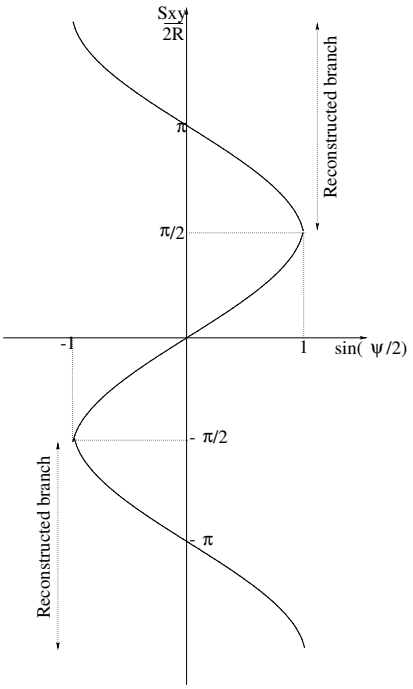

Figure 11.7: The arcsin and its different branches.

is decreasing as indicated by the calculation of the discrete derivative "der_curr". In this case, one sets $\epsilon = -\epsilon$ after initialising $\epsilon = 1$, *i.e.* sets $\epsilon = -1$, and $phase = -1$, to obtain $s = -\arcsin(func)$: negative and increasing to zero .
The turning point is monitored by the derivatives:

$$\begin{aligned} func(i+2) - func(i+1) &= \text{der\_next\_to\_next} \\ func(i+1) - func(i) &= \text{der\_next} \\ func(i) - func(i-1) &= \text{der\_curr} \\ func(i-1) - func(i-2) &= \text{der\_back} \end{aligned}$$

and occurs when

$$\begin{cases} \text{der\_back*der\_next} < 0 \\ \text{der\_curr*der\_next} < 0 \\ \text{der\_curr*der\_next\_to\_next} < 0 \end{cases}$$

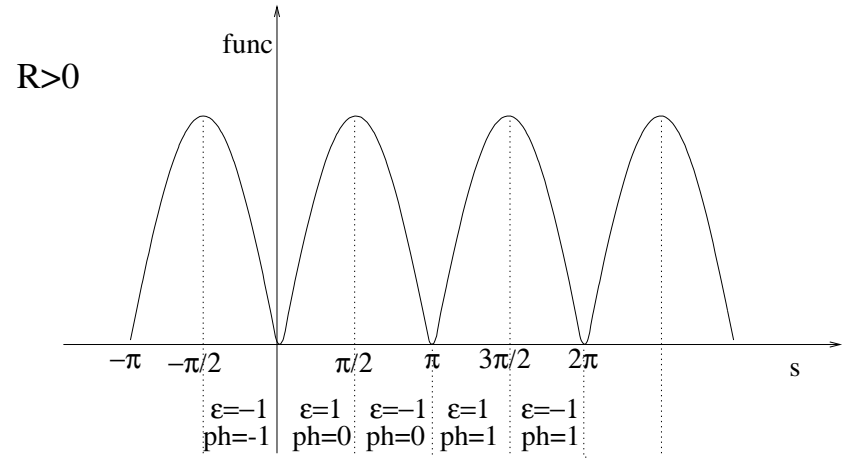

Figure 11.8: The values of ϵ and *phase* in the different zones of $func$.

The multiple check aims to get rid of the accidental fluctuation of a single point.

At the turning point between zone A and zone B, the variable *phase* is incremented by 1 and ϵ is reversed to obtain, s=arcsin($func$), i.e. positive and increasing beyond zero.

If the particle starts in zone "B", func is increasing, $phase = 0$ and ϵ has the initialisation value, *i.e.* $\epsilon = 1$.

At the next turning point *func* is increasing again, phase is kept as it was and ϵ is reversed into -1, to obtain $s = -\arcsin(func) + \pi$,i.e. positive and increasing beyond the first branch that ends at $s = \pi$.

The different zones are described by different values of ϵ and phase according to figure (11.8).

$$\begin{aligned} s = &\quad -\arcsin(func) && (\text{-}\pi/2 \rightarrow 0) \\ s = &\quad \arcsin(func) && (0 \rightarrow \pi/2) \\ s = &\quad -\arcsin(func) + \pi && (\pi/2 \rightarrow \pi) \\ s = &\quad \arcsin(func) + \pi && (\pi \rightarrow 3/2\pi) \end{aligned}$$

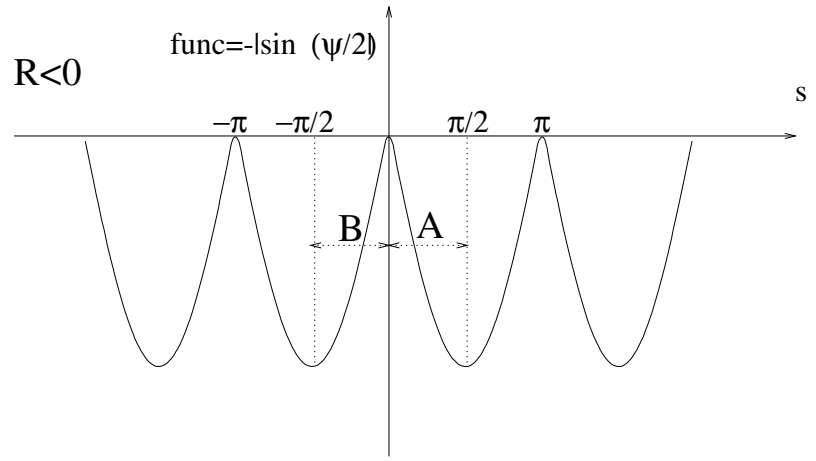

Figure 11.9: The $func$ behaviour as a function of s in the $R < 0$ case.

$$s = \quad -\arcsin(func) + 2\pi \qquad (3/2\pi \to 2\pi)$$

11.8 The reconstruction of s_{xy} in the case $R < 0$

In this case $func = signR\,|func|$ is negative (fig(11.9)) : s moves from positive values before the impact point and toward negative values beyond the impact point. The final quantity $s_{xy} = 2Rs$ instead behaves like in the previous case, from negative to positive.

Indeed, signs do compensate in the final result for s_{xy} that can be written according to eq. (11.21) in all cases. The code takes the latter shortcut and treats the case $R < 0$ like the one $R > 0$, replacing *func* by $|func|$.

This can be easily checked by considering the occurrences of *func*:

1. the check for der_curr is made with $sign(R)\times$ der_curr,
2. the condition for the turning points is quadratic in *func* and is blind to its sign,
3. the final expression for s involves $sign(R) \times \arcsin(func)$.

The case $R < 0$ is then mapped into the previous one.

11.9 The point ordering

The order of the experimental points along the helix must be consistent with the clock convention related to the sign of R. The reconstruction of the higher branches and the transition from negative to positive s_{xy} values is based on the validity of such a convention.

The program checks for its validity: the quantity *clock* is defined, corresponding to the tangent of $\psi + \phi_0$, through:

$$clock(i) = \frac{x(i) - a}{y(i) - b} \tag{11.23}$$

that generally increases or decreases if the point "i" moves clockwise or anti-clockwise in the $X - Y$ plane, respectively. The sign of the difference

$$clock(i + 1) - clock(i) \tag{11.24}$$

can then be used to monitor the respect of the convention.

However, this is false when the neighbouring points in the equation above belong to different branches of the tangent. This exception can be handled by calculating the sum of the signs of the clock differences over many points, where the effect of the pathological pair is washed by the normal ones. If the ordering convention is not respected, the order of the points is reversed and a standard analysis is made.

11.10 Flags

The algorithm performs a check to signal pathological cases to the user. This is done with a flag in the output that warns the user on the reliability of the corresponding results when its value is different from 0.

In the critical cases, the flag can assume three different values, as follows:

- the number of points is less than six. The flag is set to -1000.

- the track is too straight *i.e.* the radius is bigger than 100 m, corresponding to a transverse momentum exceeding 20 GeV/c. The flag is set to -2000.

- the points are not smooth and there is a false turning point due to a fluctuation of the point along the helix.

  The code makes a check using the derivatives for the existence of a turning point "i", and in addition calculates the difference of $func$ of the two neighbours of "i". At the true turning point, the absolute value of such a difference should be below a *threshold*. At a false point, it will be larger than *threshold* showing that $func$ is still an increasing or decreasing function. The value of *threshold* has been determined by optimising the efficiency of the fitting algorithm. The flag is set to -3000.

11.11 Charge reconstruction

The sign of R is associated with the charge of the particle. The convention on the sign of R, which assumes that the particle comes from the origin, (this condition is verified for the majority of the cases) is that for positive beam momenta, R positive means positive charge, and R negative means negative charge.
For negative beam momenta the charge assignment must be inverted (by the user).
The charge reconstruction for cosmic rays and secondaries is somehow more complicated and it will be discussed in separate sections.

11.12 Momentum reconstruction

The momentum is reconstructed using the following formulas:

$$\begin{aligned} p_x &= aR\cos\phi_0 \\ p_y &= aR\sin\phi_0 \\ p_z &= p_t\tan\lambda \end{aligned} \tag{11.25}$$

where $a = 0.299 \cdot 10^{-3} \cdot B \cdot Q$. B indicates the magnetic field, whose nominal value of 0.7 T is used. Q is the charge of the particle, set to $\pm$ 1, according to the sign of R. Note that, in the case of negative beam momenta, the value of B should be -0.7 T and the sign of the charge should be the opposite of the sign of R. Those two effects do compensate in the definition of a, and the formulae given above are valid both for positive and negative beam momenta.
The particle momentum is given in units of GeV/c.

11.13 Running "FitTpcTracksAlg" on cosmic rays

The Fitting algorithm can be used also for cosmic rays, knowing the following.
The HARP pattern recognition divides a cosmic trajectory in two tracks. The fitting algorithm finds, for one of the two tracks, a helix parametrised by the usual five parameters R, d_0, ϕ_0, z_0, tanλ, and, for the second track, a helix parametrised by $-R, d_0, \phi_0 + \pi, z_0$, -tan$\lambda$. These two sets of parameters correspond to the same geometric helix, but there is an ambiguity on the signs of the charge and of the momentum components.
The ambiguity comes from the fact that the sign of R is assigned evaluating the asymmetry: seen from the origin, the two tracks associated to the same cosmic ray bend in opposite directions.
The ambiguity on the physics information to be extracted from the helix parameters cannot be solved using TCP data only. It can be solved for example using the time information given by the RPC: the first branch in time will be the incoming particle, and for this one the signs of the charge and of the momentum components must be inverted.

11.14 Secondaries

The hypothesis on the starting branch of the arcsin explained at the beginning of section 7, is such that the z_0 value for tracks starting from secondary vertexes, corresponds to true physics interpretation for high transverse momentum ($> 40\,\mathrm{MeV/c}$) particles.

The other helix parameters are correctly found, and the absolute value of the momentum components is also reliable, being independent on z_0.

The information on the signs of the charge and of the momentum components is again ambiguous because the tracks do not start from the origin. The ambiguity has to be solved using the additional information coming from other detectors.

Chapter 12

The efficiency of the TPC reconstruction chain

In order to test the track parameters and momentum reconstruction efficiency, two kind of tests have been performed. Firstly, Monte Carlo events have been used, and secondly, cosmic ray data have been analysed.

12.1 Momentum reconstruction using Monte Carlo events

The Monte Carlo events used contain a single muon, of fixed momentum, emerging at variable angles from the origin. The muon propagation in the TPC material is simulated, taking into account effects of energy loss, and ionisation clusters are then formed and given in input to the pattern recognition algorithm. A fit to the data assess the efficiency of the last part of the TPC reconstruction chain (pattern recognition and fit) but is of course not sensitive to calibration and clustering. This test of the pattern recognition algorithm is restricted to the simple case of single track events. Real events have more than one track, and the assignment of clusters to the correct tracks, is of course more complicated.

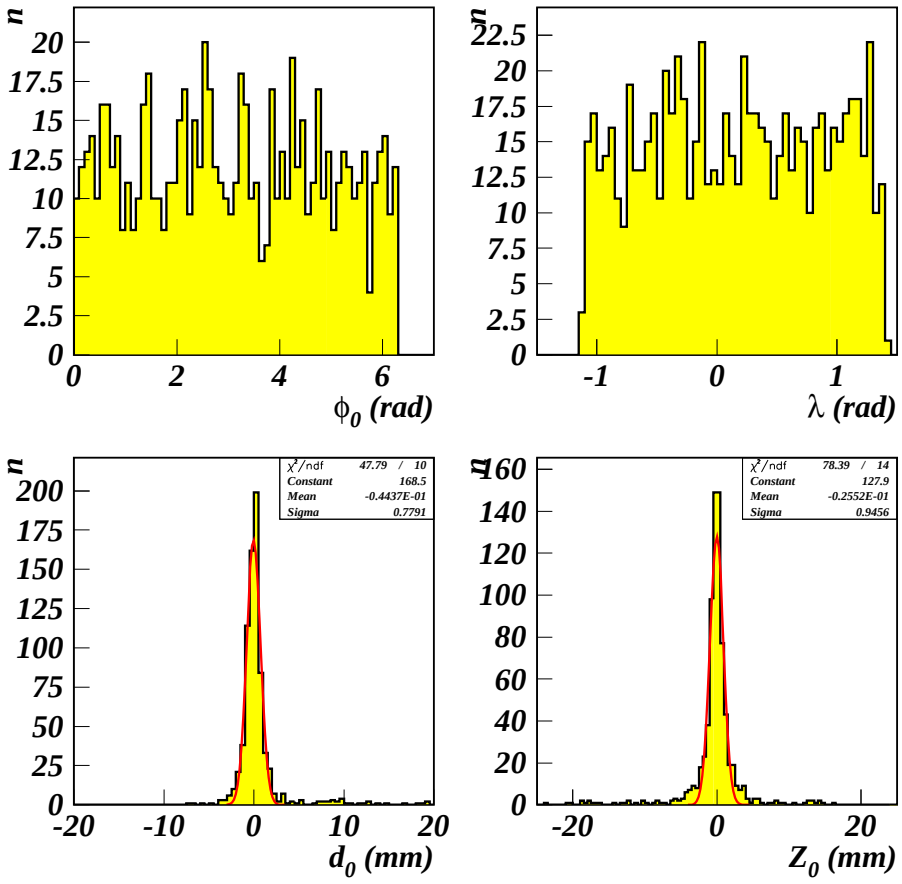

Figure 12.1: Angular distributions and impact point resolution for simulated muons of 176.4 MeV/c total momentum.

12.1.1 Results without point smearing

A first test was performed using tracks of muons emerging from the origin and subject to multiple scattering and energy loss, without any point smearing. The kinetical energy of the simulated muons was chosen as 100 MeV, corresponding to a total (and fixed) momentum of 176.4 MeV/c.

Figure 12.1 shows the distributions of the helix geometric parameters for selected muon tracks having at least ten clusters and without error flag. The upper plots

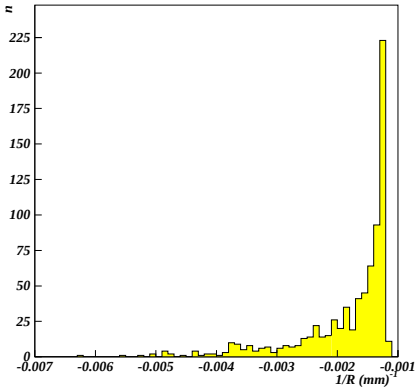

Figure 12.2: Inverse of the curvature radius of the reconstructed tracks. Its sign gives the charge of the particle.

show the angular distribution of the tracks. They uniformly cover the full solid angle around the target.

The lower plots show the resolution on the impact point coordinates. The radial coordinate has a resolution of 0.8 mm while the z coordinate is reconstructed with a resolution of approximately 1 mm.

The inverse of the radius of curvature of the tracks, ρ, is presented in figure 12.2. The sign of ρ is always negative. It gives the charge of the muons, which is correctly reconstructed for the totality of the events. The absolute value of the radius is related to the transverse momentum of the muons, which ranges from 30 MeV/c and the total momentum of 176 MeV/c.

Figure 12.3 shows the momentum distribution. The cyan line corresponds to the true value of the momentum. The shift of 3.1 MeV/c between the central and the true value is due to the fact that the energy loss mechanisms is not taken into account in the track fitting (the energy loss by a muon of 100 MeV kinetical energy traversing

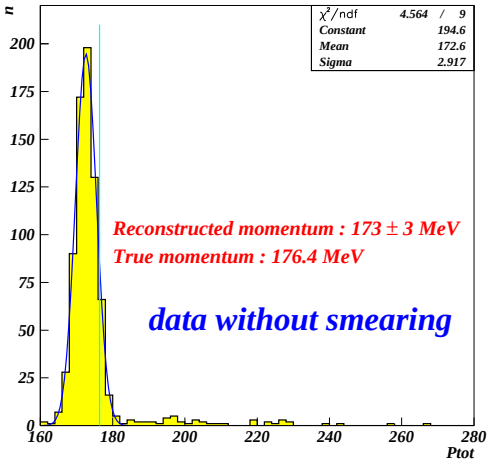

Figure 12.3: Reconstructed momentum for simulated data without any point smearing. The cyan line represents the true momentum.

the target support, the scintillator fibers of the inner trigger cylinder and the inner field cage is of the order of 3 MeV).

The error on the momentum due to the multiple scattering is not considered either in the reconstruction algorithms. It can be estimated as [76]:

$$\left.\frac{\sigma(Ptot)}{p_t}\right|^{MS} = 0.045\frac{1}{B\sqrt{LX_0}} \tag{12.1}$$

where L is the track length and X_0 the radiation length, expressed in meters. The momenta are in units of GeV/c. Taking into account the drift in the gas, for an average track length of 0.5 m, the error due to the multiple scattering is approximately 1.3 MeV/c. Future developments of the software will take into account the energy loss mechanism and the multiple scattering.

The queue in the histogram is mainly due to events emerging at $\phi_0 \approx \pm\pi/2$ where the fitting algorithm is less efficient.

Decomposing the momentum in its transverse and longitudinal parts, the transverse momentum resolution $(\Delta P_t)/P_t^2$ is $0.12\times10^{-3}\,(\mathrm{MeV/c})^{-1}$ while the longitudinal momentum resolution is around 3 MeV/c, as shown in figure 12.4.

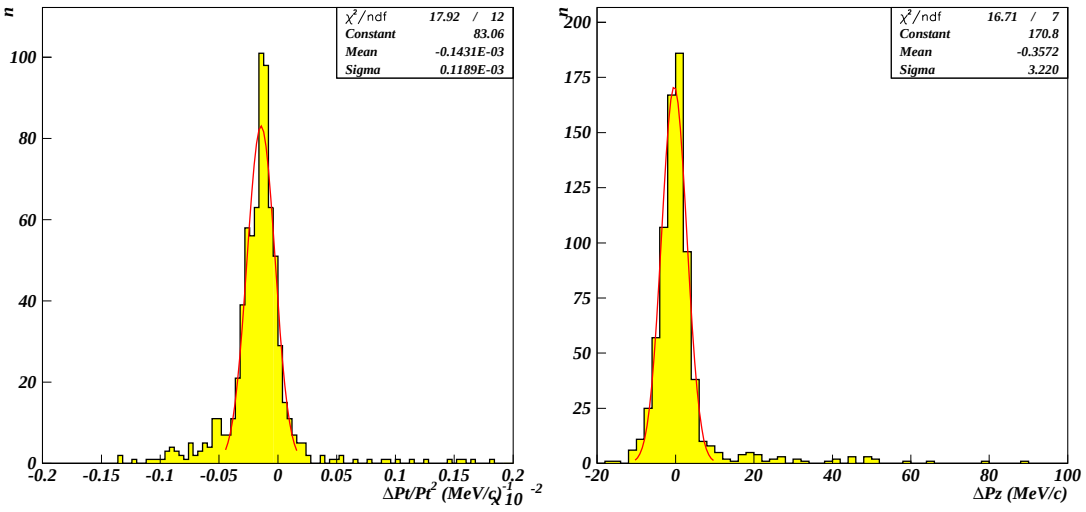

Figure 12.4: $\Delta Pt/Pt^2$ and ΔPz obtained for simulated muons of 176 MeV/c total momentum and without smearing.

12.1.2 Results with point smearing

The same test described above has been performed using Monte Carlo data which include 2 mm smearing of the clusters coordinate to take into account a more realistic detector resolution. This figure follows from the studies of the residuals between the cluster position and fitted helix already presented in section 10.3.

The simulated data sample is composed of single track events (μ^+), of total momentum varying from 176 MeV/c to 800,MeV/c, spanning the full solid angle.

Figure 12.5 shows the reconstructed radial and longitudinal coordinates of the impact point: their resolutions are 2.3 mm and 3.2 mm respectively. Those numbers are approximately 2 mm worse than in the case of tracks without smearing, as expected.

The charge assignment from the fit remains correct at the per mille level.

The transverse momentum resolution is shown in figure 12.6 as a function of the transverse momentum itself: p_t is determined with 20% accuracy at 500 MeV/c and the error introduced ignoring the energy loss and the multiple scattering is negligible

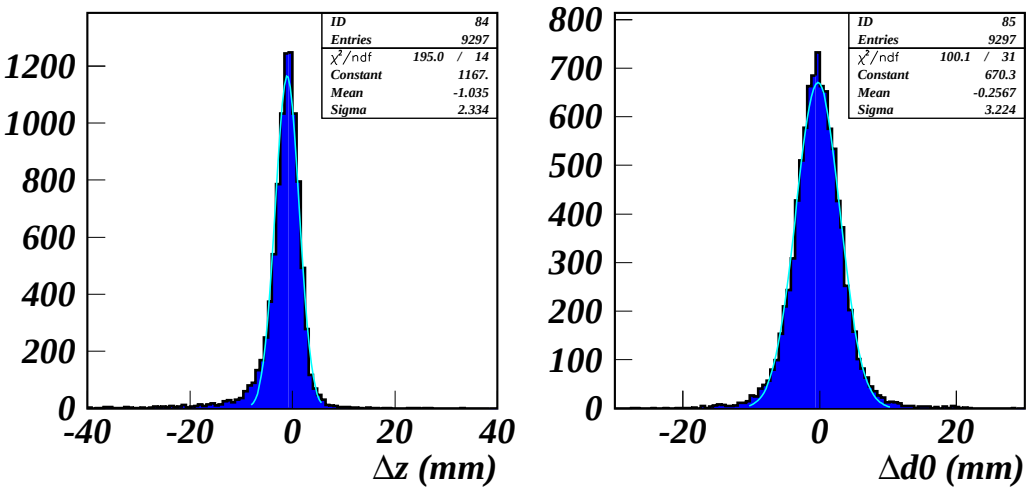

Figure 12.5: Impact point resolution

at the end.

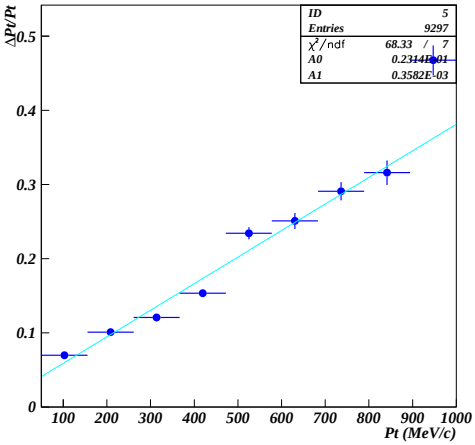

Figure 12.6: Transverse momentum resolution for single track Monte Carlo data with 2 mm smearing, and no inefficiencies.

12.2 Cosmic ray data

Cosmic rays passing trough the central blind zone of the TPC are reconstructed in HARP as two separate tracks. An example is given in figure 12.7. As the two segments belong to the same particle, they should be reconstructed with correlated helix parameters (as already explained in the section 4.13) and with the same momentum. The TPC resolution can be evaluated using the difference of the reconstructed geometric parameters and momenta associated to these two track segments.

The cosmic rays are triggered by couples of diametrically opposed barrel RPCs.

An analysis has been performed using 2002 data which selects events with two tracks

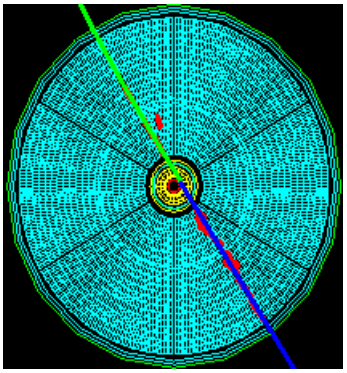

Figure 12.7: $X - Y$ view of a cosmic ray traversing the TPC. Its track is divided in two regions by the pattern recognition.

composed by at least 10 clusters and not more than 20. These limits are chosen to have a good track fit accuracy and taking into account the number of pad rows of the TPC, which is 20. If a track has more than 20 clusters it means that the muon track does not pass by the central zone and it is not divided in two branches. An example of event with this characteristic is displayed in figure 12.8. In addition a cut on the z coordinate of the clusters is made: it is required that the muons do not pass trough the stesalite structure around the target region.

Even after applying these exposed cuts, the data sample contains a certain number

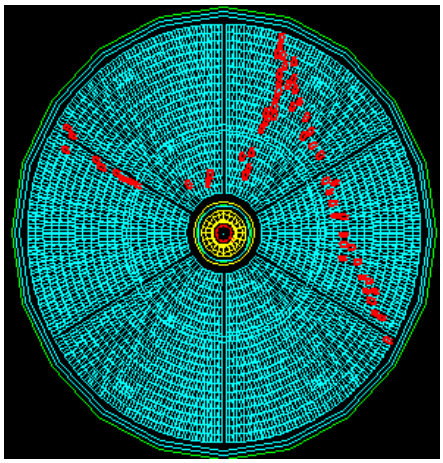

Figure 12.8: $X - Y$ view of a cosmic ray interacting in the outer field cage.

of "bad" events that are not filtered out and will affect the results of the analysis. Two examples are shown in the figure 12.9: the left one clearly contains two tracks not belonging to the same particle, while the right one is badly reconstructed.

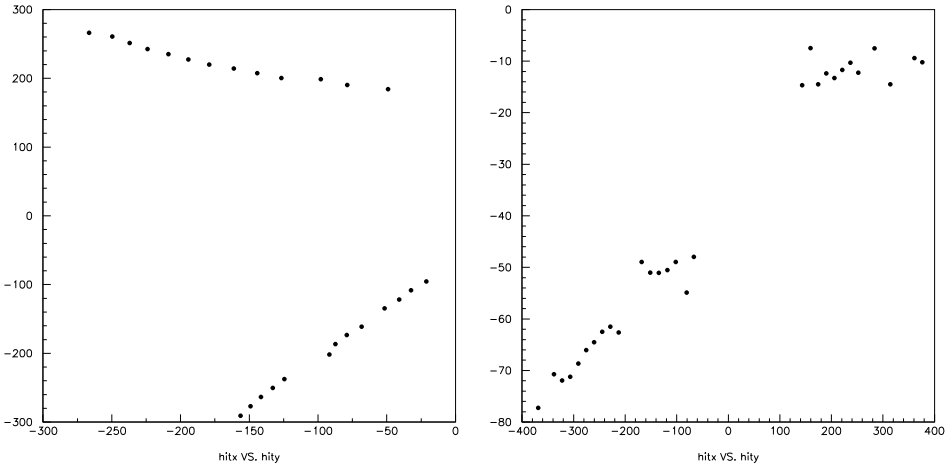

Figure 12.9: $X - Y$ view of a "bad" cosmic ray events not filtered by the applied cuts.

The angular resolution in the $X - Y$ plane is evaluated using the absolute value

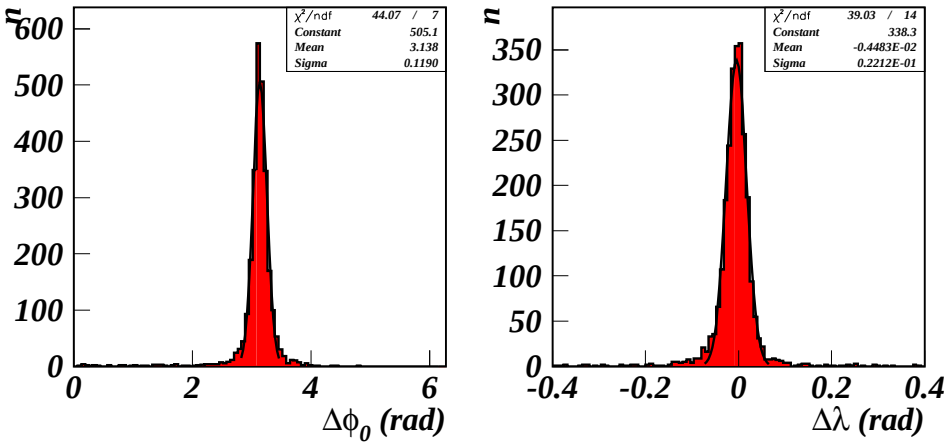

Figure 12.10: $\Delta\Phi$ and $\Delta\lambda$ distributions for cosmic ray tracks.

of the difference between the ϕ_0 angles of the two branches of the track. The central value of this variable is 3.138, as expected for back-to-back particles, and the width is 0.12 radians. The difference between the λ angles formed by the tracks with the Z axis, have also been evaluated: the central value is compatible with zero and the width of the distribution is 0.02 radians. The two angular distributions are presented in the figure 12.10.

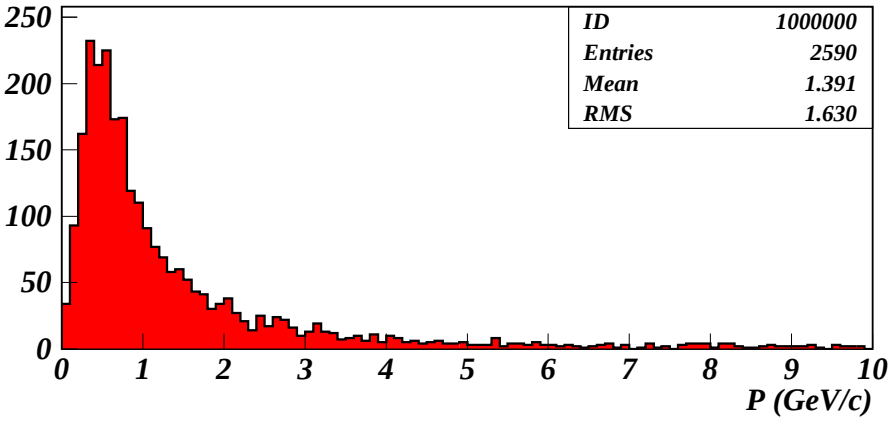

Figure 12.11: Momentum distribution of cosmic rays.

The total momentum spectrum of the cosmic rays is shown in figure 12.11 and has a mean value of 1.4 GeV/c.

An estimate of the momentum resolution can be obtained by comparing the reconstructed momenta of the two branches of the tracks. Their correlation plots, obtained with a binning of 10 MeV/c and of 66 MeV/c, are shown in figure 12.12. In the left

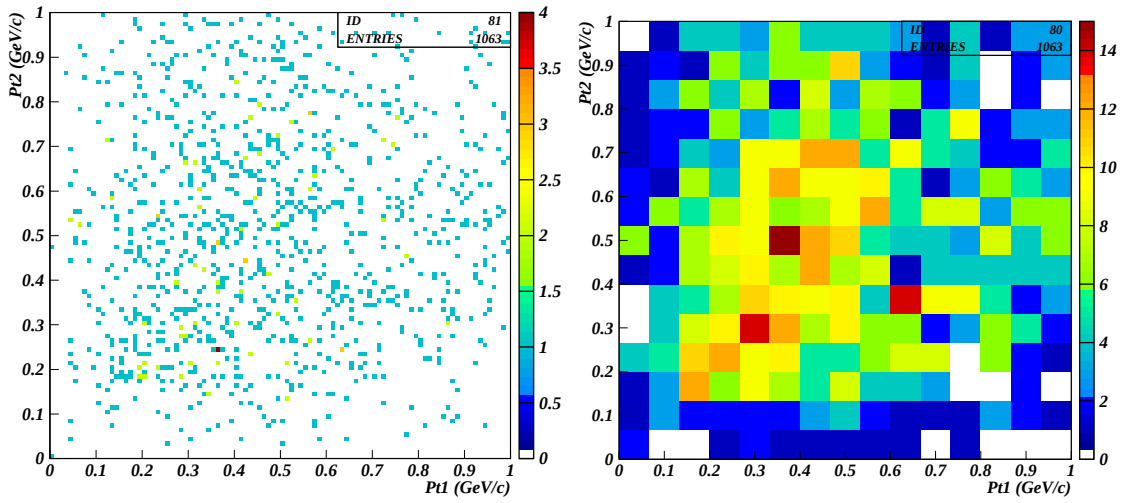

Figure 12.12: Correlation between the transverse momenta of the two branches of the cosmic rays tracks. In the left plot the bin width is 10 MeV/c while in the right plot it is 66 MeV/c.

plot, which has a binning of 10 MeV/c, the correlation is washed out by the experimental resolution. Such a correlation is roughly visible when the binning width approaches the real resolution (right plot).

A profile histogram providing a more quantitative estimate of the momentum resolution for cosmic ray data is presented in figure 12.13, together with the already shown results obtained from Monte Carlo data. The transverse momentum resolution estimate from cosmic is around 47% at 500 MeV/c while for simulated data was of 20%. The bad resolution for the real data is due to detector inefficiency and will surely improve by solving the cross-talk problem of the TPC.

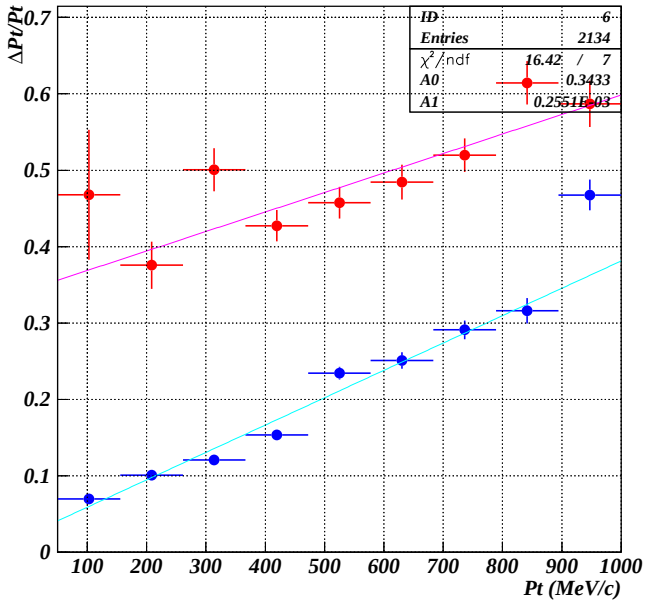

Figure 12.13: Transverse momentum resolution for cosmic ray data (red dots) and Monte Carlo data (blue dots).

Chapter 13

The “large angle” analysis

The so called “large angle” region of the HARP detector is the zone covered just by the TPC and the barrel RPCs. In this region, the angular range for particles emerging from the origin is from 0.38 to 2.47 radians as sketched in figure 13.1. This angular range is however slightly modified for runs with 100% interaction length targets.

An analysis is performed, discussed below, which uses information coming from the

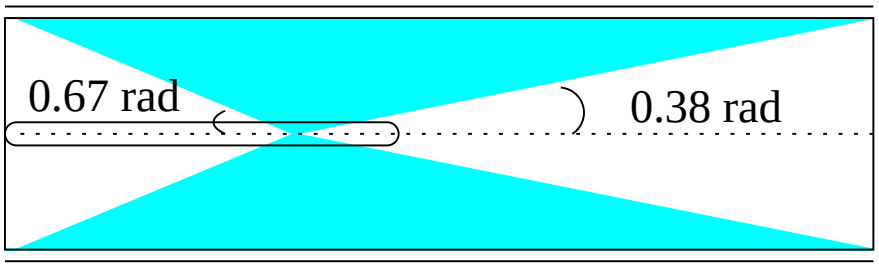

Figure 13.1: The “large angle” region.

beam instrumentation, the TPC, the barrel RPCs and the Inner Trigger Cylinder.

13.1 Tantalum target at 3 GeV/c beam momentum

The first target material analysed is the ^{73}Ta for a beam momentum of 3 GeV/c. Data obtained in the 2001 run with 2% and 100% interaction length target were collected. They were reconstructed using a preliminary version of the software, available in May 2002. Since then, several improvements to the various algorithms were implemented but, unfortunately, no production with the new reconstruction code was possible at the time of writing and and there is not yet possibility to identify particles.
The analysis is focused on interactions caused by protons. The first step is hence their selection, which is particularly important because, at low momentum, the T9 beam is highly contaminated by electrons and other particles, as shown in figure 9.2. At 3 GeV/c, the beam protons are identified by their time-of-flight while electrons are vetoed by the beam Cherenkov counter "A".

13.1.1 Over lay interactions

At low momentum, *out-of-time* interactions are often observed. They are produced by the interaction of a beam particle which arrives inside the 30μs time window of the beam particle that triggered the data acquisition.
These tracks are reconstructed with an incorrect z position because of their time offset and are cut in the analysis requiring an RPC signal matching the track extrapolated from the TPC.

13.1.2 Preliminary cuts

A set of preliminary cuts is applied to select tracks:

- there must be an ITC hit for the event, what defines a large angle interaction
- no numerical error nor error flag should be associated with the track

- the tracks must have at least 10 hits to ensure an accurate fit
- the particles have $P_t > 10\,\mathrm{MeV/c}$, in order to reject passing through particles and noise
- there is a TPC-RPC match to cut out-of-time tracks and to ensure a greater accuracy
- the transverse momentum should not exceed $1\,\mathrm{GeV/c}$ and the longitudinal momentum should be in the range -1-2 $\mathrm{GeV/c}$ because of kinematical constraints

The last cut is derived from the hypothesis of an incoming proton interacting with a proton at rest and yielding a final state with a proton at rest and a proton and a pion sharing the remaining energy.

13.2 Impact point reconstruction

The impact point of the selected tracks is reconstructed. The plots in figure 13.2 show the absolute value of the impact parameter d_0 and the z coordinate of the impact point for the thin and thick target.(The dimensions of the thin target are 30 mm diameter in $x-y$ and 2.2 mm in z. It is located downstream of the origin of the axis. The thick target has the same diameter of the thin one and a length of 170.1 mm in z. It is centred on z=0.)
The left plots in the figure show that the impact parameter distribution has the same width for the thin and thick target, as expected. There is an excess in the region of $d_0 \approx$30 mm, discussed below.
The z distributions reproduce the target dimensions. The small peak visible at around 300 mm in the thin target data is due to interactions in the end-cup of the Stesalit field cage. It is not visible for the thick target data since is masked by a greater background.

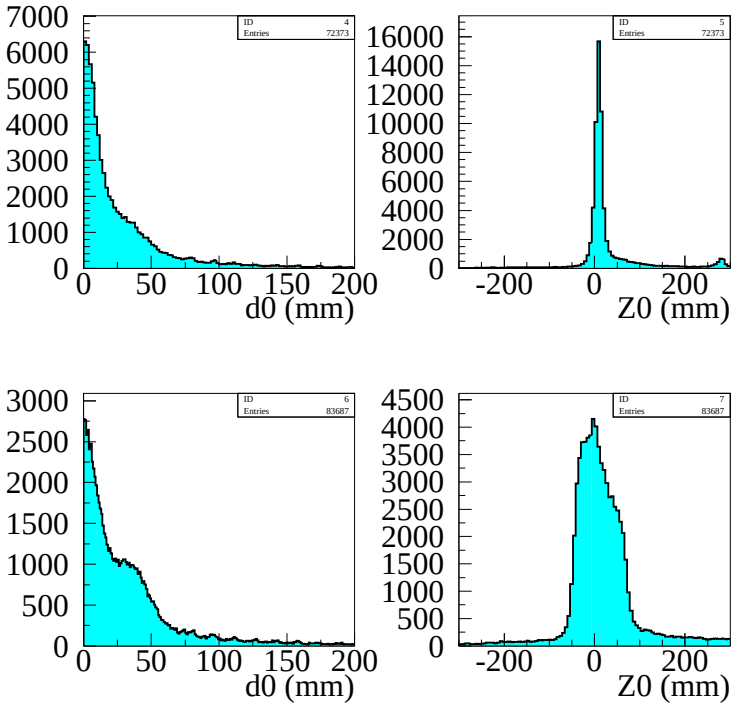

Figure 13.2: Absolute value of the radial coordinate and longitudinal coordinate of the impact point for proton collisions on thin (upper) and thick (lower) Ta target for a 3 GeV/c beam momentum.

13.2.1 Investigation on the impact point shape

A closer look at the d_0 distribution with its sign, shows that the anomalous excess of events appears for negative d_0 only (figure 13.3).

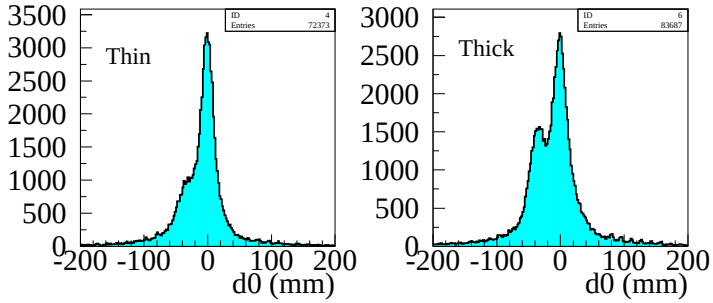

Figure 13.3: Impact parameter for thin and thick Ta target data at 3 GeV/c.

Additional information can be obtained by looking at the correlation between d_0 and the transverse momentum presented in figure 13.4.

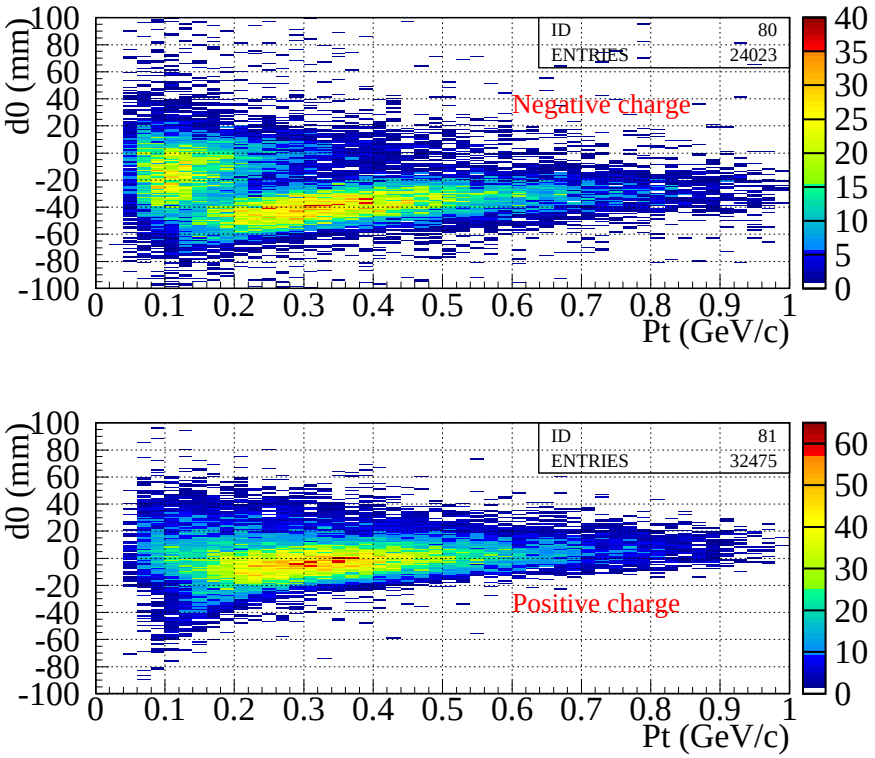

Figure 13.4: Correlation between the impact parameter and the transverse momentum for negative (upper) and positive (lower) particles.

For negative particles, two distinct zones are visible, one symmetric around $d_0 = 0$ with relatively low p_t and the other asymmetric towards negative d_0 values and at larger p_t.

For positive particles, a single zone is observed.

The effect may be interpreted as follows. The majority of the events occurs around $d_0 = 0$, both for positive and negative charges. However, for large transverse momenta the track curvature is small and the experimental resolution can lead to charge confusion, *i.e.* the negative charges might be identified as positive and vice-versa.

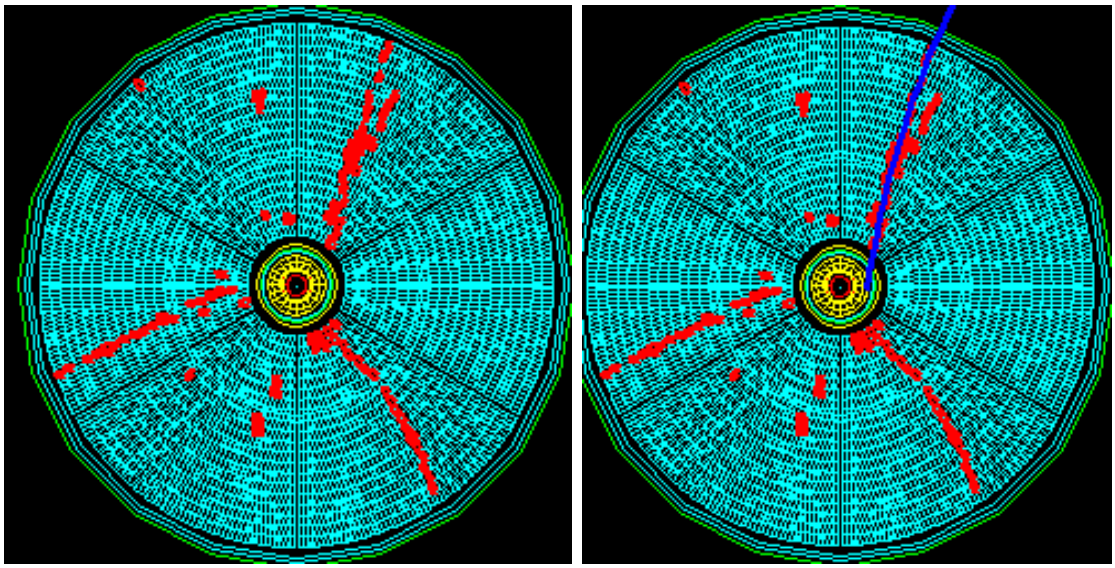

Figure 13.5: Example of events showing the charge assignment problem.

At the same time, the wrong curvature shifts the events from small values of d_0, irrespectively of its sign, to large and negative values. An example of event showing this charge assignment problem is shown in figure 13.5. This happens symmetrically in the two charge cases, however, given the unbalance between the two distributions, the contamination from positive charges on the negative charge distribution is visible, while the opposite is not true. The excess of events in fact is visible only in the negative charge case, while , to a first approximation, the one for the positive charge can be considered as the real one.

Figure 13.6 shows the d_0 distributions separately for positive and negative particles and for different transverse momentum slices. At low momentum, an excess on the negative d_0 side is visible both for positive and negative particles. It can be due to e^+e^- pairs generated by photon conversions on the target surface. The tracks corresponding to these pairs have in fact negative impact parameter. Going at higher momenta, where the track reconstruction is more difficult due to the little sagitta

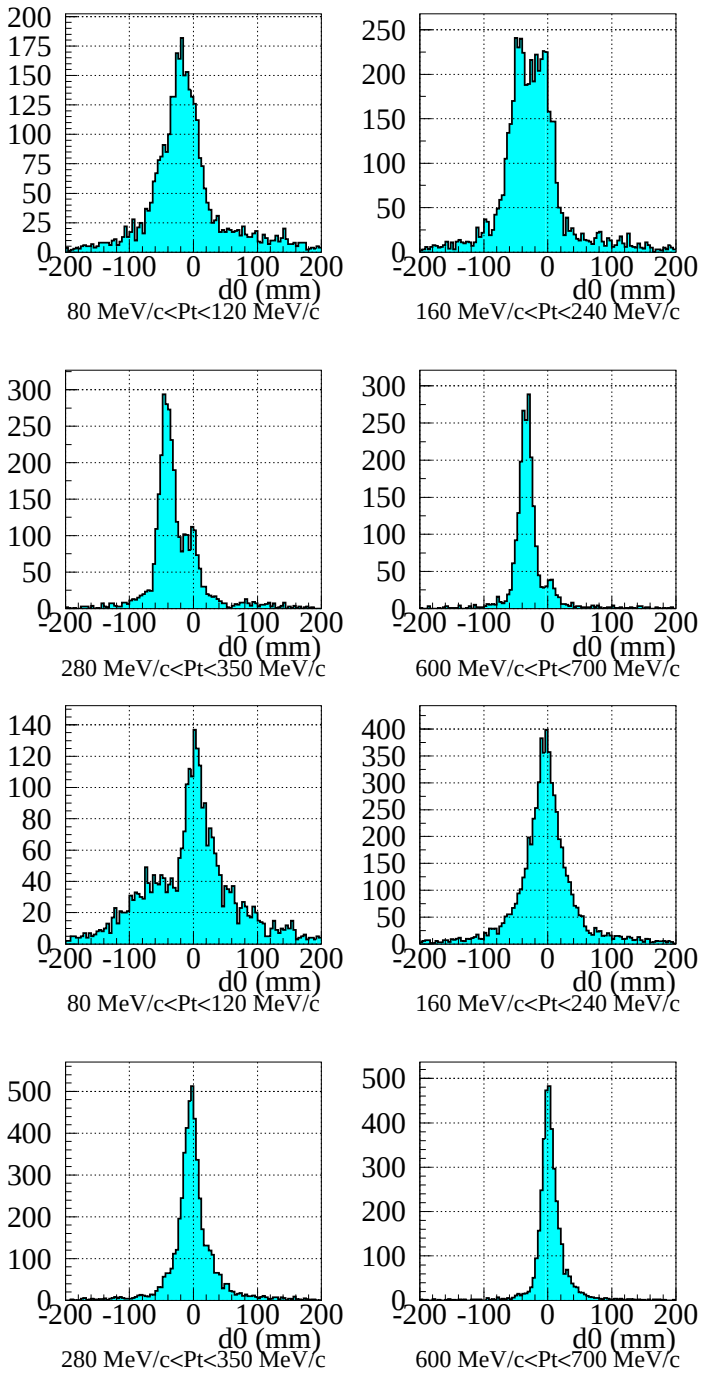

Figure 13.6: Impact parameter at different P_t values for negative (upper 4 plots) and positive (lower 4 plots) particles.

value, for the negative particles the peak of the tracks with wrong charge assignment and negative impact parameter becomes more and more high. The effect is not clearly visible for the positive particles given the already mentioned unbalance of the relative abundances.

To remove this systematic effect, only tracks with low absolute values of the impact parameter are considered in the following, and, in particular, particles with $0\,\text{mm} < d_0 < 2\,\text{mm}$ are retained. In this way, tracks with wrong charge assignment are rejected without yielding any bias in the momentum distributions.

Applying this cut, the distribution of z reported in the plots 13.7 are obtained. There is no substantial difference with the result obtained before the cut on d_0, what proves that there is no correlation between the z coordinate of the impact point and possible charge assignment confusion.

For further analysis, an additional selection on the z coordinate of the impact point

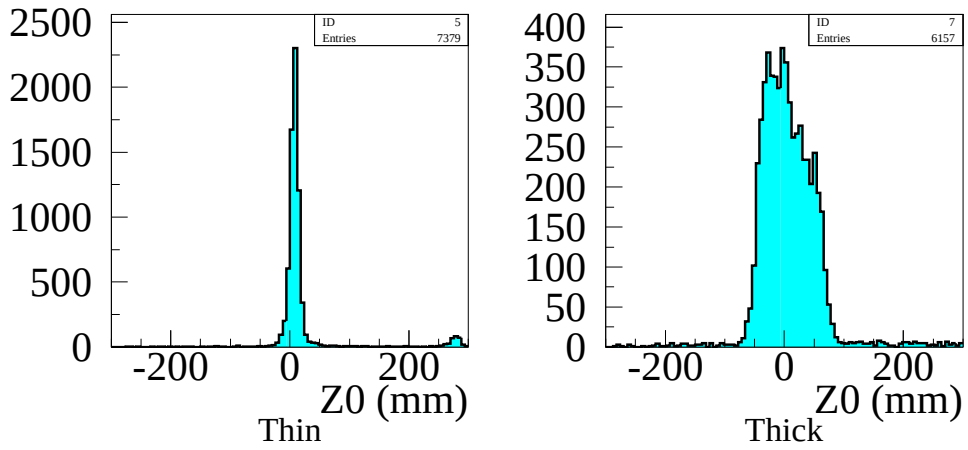

Figure 13.7: z coordinate of the impact point after the cut on d_0.

is applied, to cut tracks not originating from the target region and to eliminate the background.

13.3 Momentum distributions

The transverse momentum distributions for the thin and thick targets are displayed in figure 13.8. The mean p_t is around 365 MeV/c for both target length.

The maximum kinematically allowed p_t is of about 0.7 GeV/c but a small fraction of the events is beyond this value, compatible with the error in the momentum reconstruction of about 200 MeV/c.

The transverse momentum region below 100 MeV/c is more populated by negative particles than positive. Particles with valence antiquarks must originate from gluon

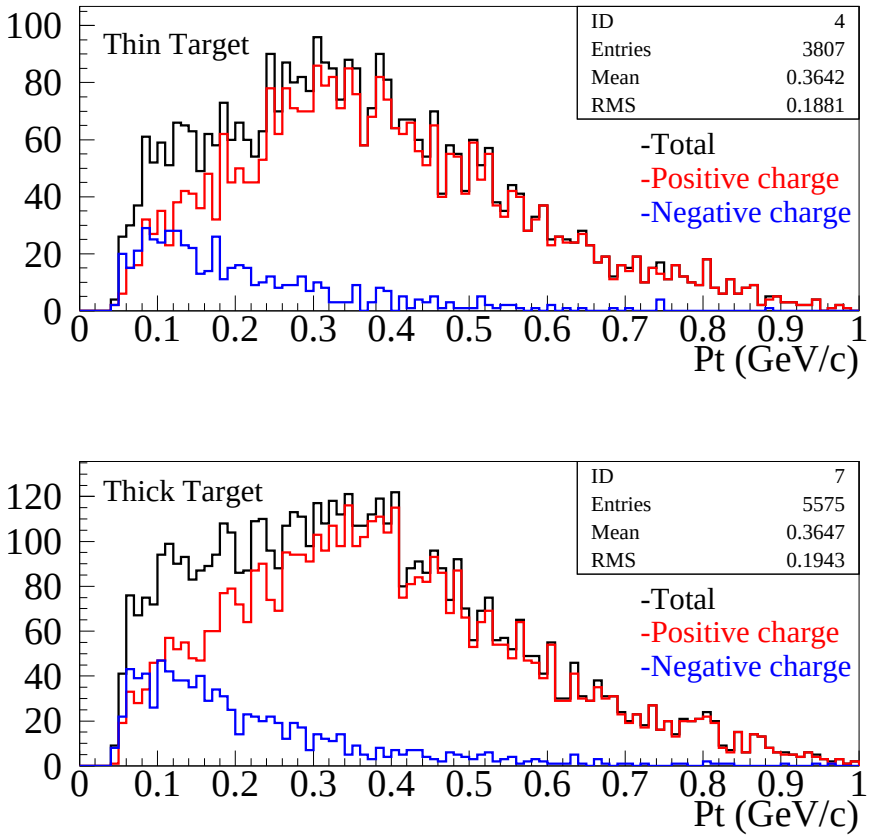

Figure 13.8: Transverse momentum distributions with the Tantalum targets and beam momentum of 3 GeV/c.

radiation whose emission probability is peaked at low energy. Gluons, in turn, convert into $q\bar{q}$ pairs that give rise to soft, charge symmetric particles. In addition, π_0 decaying into two photons may create electron-positron pairs that contribute to restore a charge symmetry. The two cases will be distinguished when it will be possible the use of the RPCs to identify the particles by time-of-flight. In addition, in the momentum region below 100 MeV/c, the TPC should permit electron/pion separation via dE/dx measurements.

Longitudinal momentum distributions are shown in figure 13.9. The maximum visible

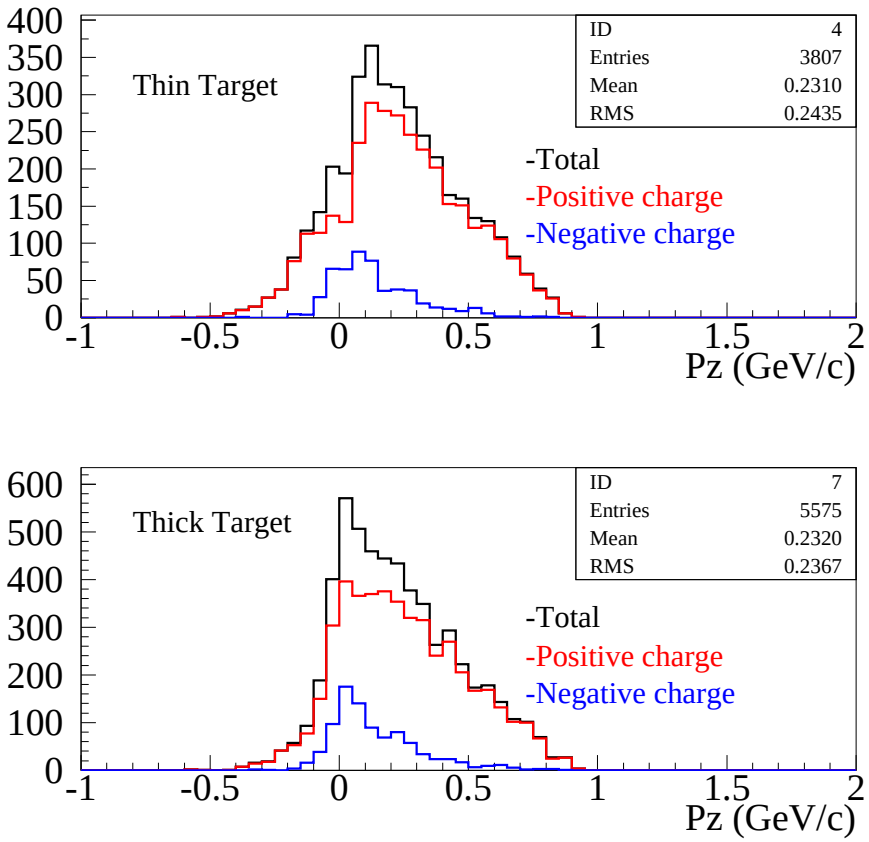

Figure 13.9: Longitudinal momentum distributions with Tantalum target and a proton beam momentum of 3 GeV/c.

p_z is restricted by the request of large angle interaction that forbids particles in the

forward direction within a cone of ± 0.38 radians around the beam line. Therefore, the kinematic limit of the order of 1.7 GeV/c can not be reached. Indeed, the kinematic limit compatible with the angular cut turns out to be around 1.1 GeV/c. In the backward direction, the limit for negative longitudinal momentum is ≈ 250 MeV. The observed distributions are in good agreement with these kinematic limits.

The charge asymmetry increases with the longitudinal momentum because of the onset of the leading particle effect that gives more momentum to particles with the same charge of the projectile. This effect would be clearly visible including the forward region in the acceptance.

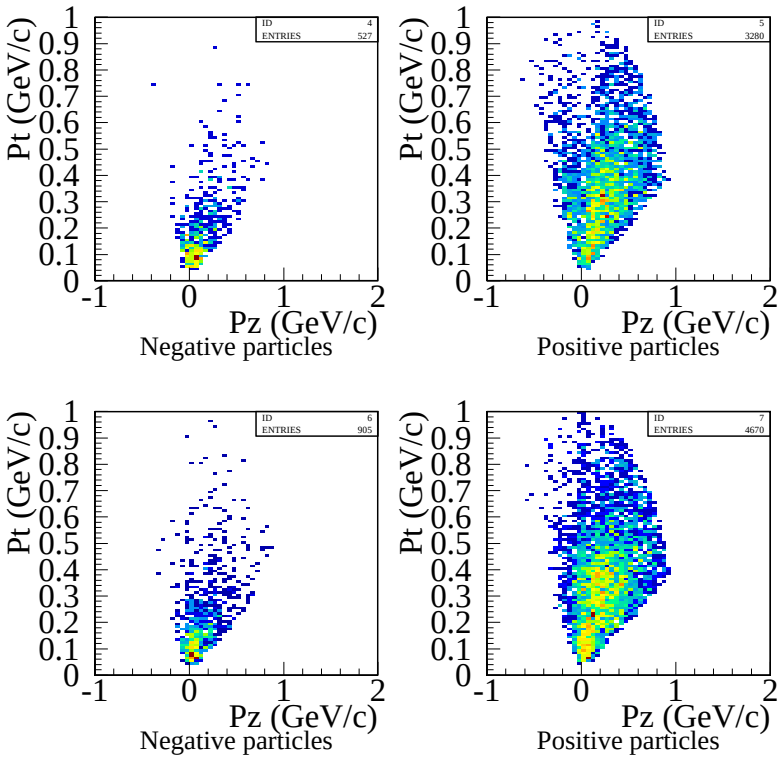

Figure 13.10: Correlation between transverse and longitudinal momentum obtained with the thin (upper plots) and the thick (lower plots) Tantalum target and a proton beam momentum of 3 GeV/c. Positive and negative particles are separated.

The histograms in figure 13.10 show the $p_t - p_z$ correlation for positive and negative particles and are bounded by the large angle cuts that are of the form $p_t/p_z < C$, where C is a different constant for the forward and backward zone. The plots indicate for the forward region $C \approx 0.4$ and for the backward region $C \approx 1.0$, in agreement with expected values. The plots indicate a mild correlation.

13.4 Positive to negative particle ratio

The positive to negative particle ratio summed over all momenta is 6.2 for the thin target and 5.2 for the thick one. The detailed momentum distributions show that it is a function of the particles momenta that tends to 1 for soft particles. The thickness dependence can be attributed to the re-interaction that tends, for thicker targets, to equalise negative and positive charges in the final state.

13.5 K2K target

K2K [89] is a long baseline experiment which aims to confirm the growing evidence of neutrino oscillations. A proton beam of 12 GeV energy is shone on an Al target. The pions produced in the collision decay into muons and ν_μ, which are detected in a near detector, located approximately 250 m downstream the target station. The ν_μ beam travels 250 km to the SuperKamiokande detector, where the disappearance of ν_μ is investigated (figure 13.11). In K2K the pion yield in the energy region below 1 GeV/c is estimated at present using a Monte Carlo. Clearly the experiment would benefit of a direct measurement of the pion production cross section. For that reason, aluminium targets similar to that used in K2K and of other various thicknesses were investigated in the HARP experiment, at a beam momentum of 12.9 GeV/c.

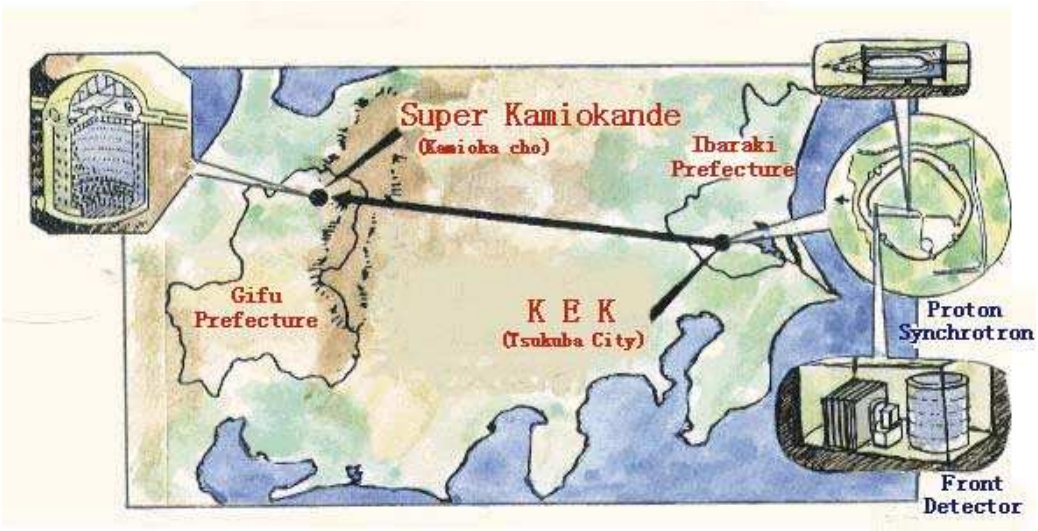

Figure 13.11: Outline of the K2K experiment.

13.6 The analysis of the K2K data

An analysis is reported on "K2K data" collected during August 2002 and based on an improved version of the reconstruction software with respect to the Tantalum case, albeit still incomplete and without particle identification.

Two targets are considered, a thin one, of 2% interaction length, and a thick one, of 100% interaction length. As in the Tantalum case, the thin target position in the HARP experiment is downstream of the origin while the thick one is centred in the origin. The target length are 7.9 mm and 394.4 mm, respectively, while their diameter is 30 mm.

Beam protons are selected vetoing signals in both beam Cherenkov counters.

The same set of preliminary cuts used for the Tantalum is applied, with the exception of those on the transverse and longitudinal momenta. To take into account the beam momentum of 12.9 GeV/c, the kinematical constraints read:

- transverse momentum below 2.5 GeV/c

- longitudinal momentum in the range $-1 \div 6\,\mathrm{GeV/c}$

The cut on the longitudinal momentum is not very strict and considers the forbidden forward and backward angles.

13.6.1 Impact point reconstruction

Figure 13.12 shows the absolute value of the radial and the longitudinal coordinates of the impact point for the two different target thiknesses. The impact parameter

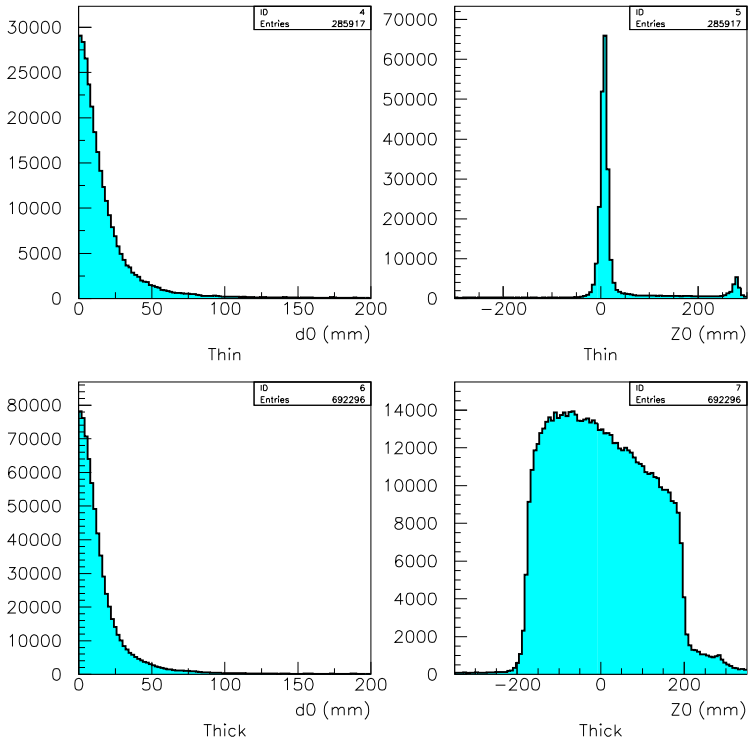

Figure 13.12: Absolute value of the radial coordinate and longitudinal coordinate of the impact point for proton collisions on Al thin (upper plots) and thick (lower plots) target at 12.9 GeV/c beam momentum.

distributions have a Gaussian shape, and seem not to show the pathologic excess observed in the Tantalum data. This is both due to the software improvement, and

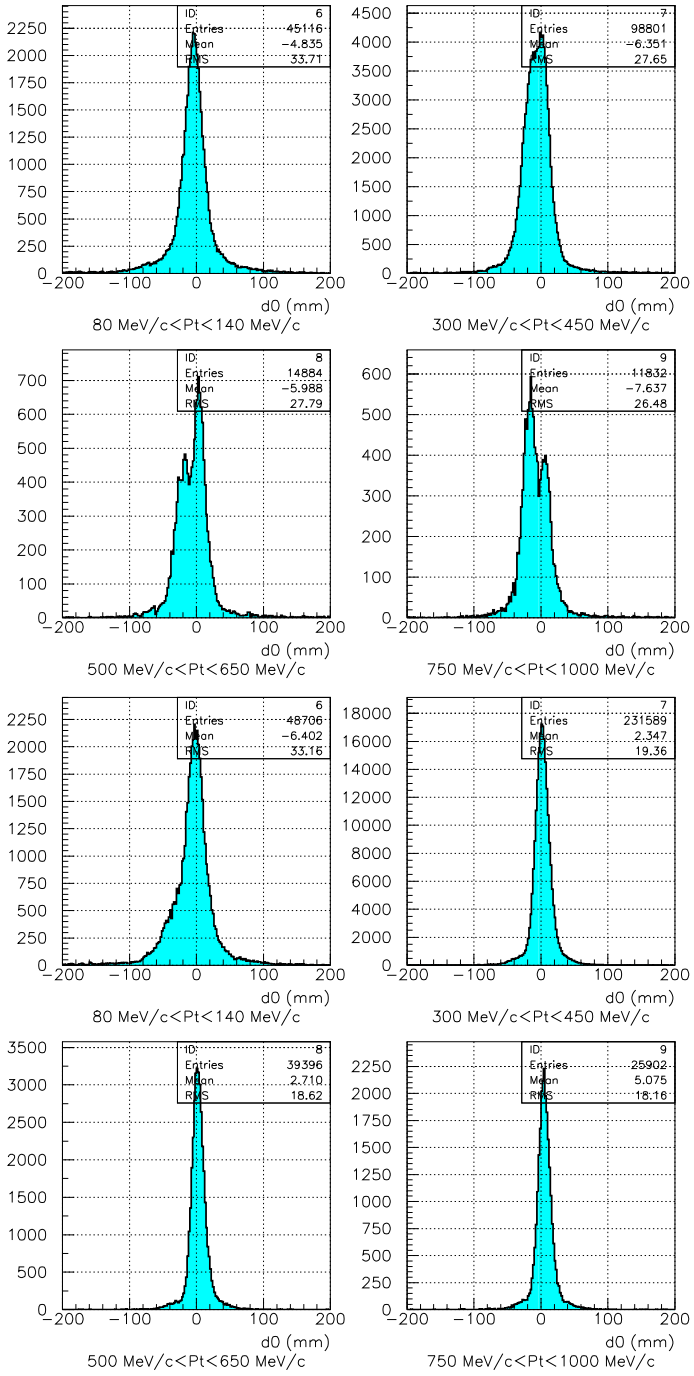

Figure 13.13: Impact parameter at different P_t values for negative (upper 4 plots) and positive (lower 4 plots) particles.

to the fact that the data sample is of the 2002 run, when the number of "dead" pads substantially decreased. The z distributions reproduces well the target dimensions. The shape for the thick target reflects the beam attenuation in z due to the interactions. At $z \approx$300 mm, the peak due to interactions in the Stesalite is observed: in the following analysis, a cut on z filters out those events.

A more accurate analysis of the d_0 distributions shows that, at high transverse momentum, when the measurement of the sagitta becomes more critical, the charge assignment problem is still present, especially for negative particles, as shown in figure 13.13. The impact parameter histograms show the superposition of two distributions: a first one, peaked at zero, and relative to events correctly reconstructed, and a second one, shifted towards negative d_0 values. This second component becomes more and more evident with the increasing of the transverse momentum. The problem affects only a small fraction of events with respect to the Tantalum case, as can be also observed comparing figure 13.14, in which d_0 is presented as a function

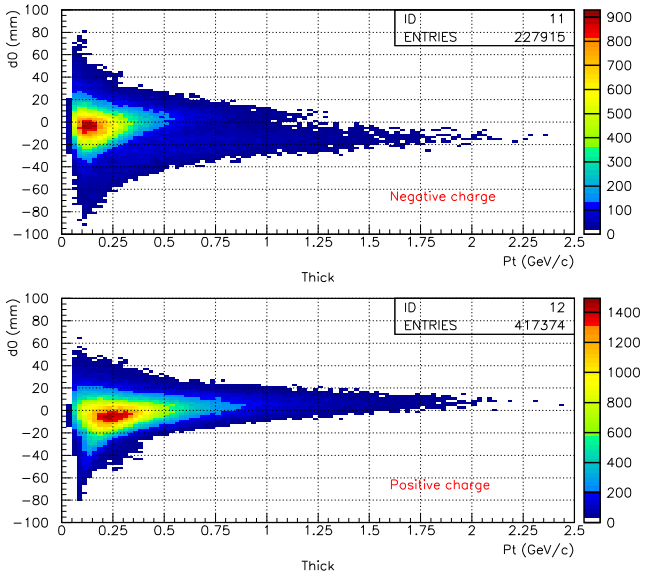

Figure 13.14: Impact parameter as a function of the transverse momentum.

of the transverse momentum, with figure 13.4.

13.6.2 Momentum distributions

In order to compare the momentum distribution with those obtained in the Tantalum case, the same cut on d_0 has been applied. The mean transverse momentum is around 410 MeV/c while the longitudinal one is around 400 MeV/c. Transverse and longitudinal distributions, shown in figure 13.15 and 13.16, are within the expected

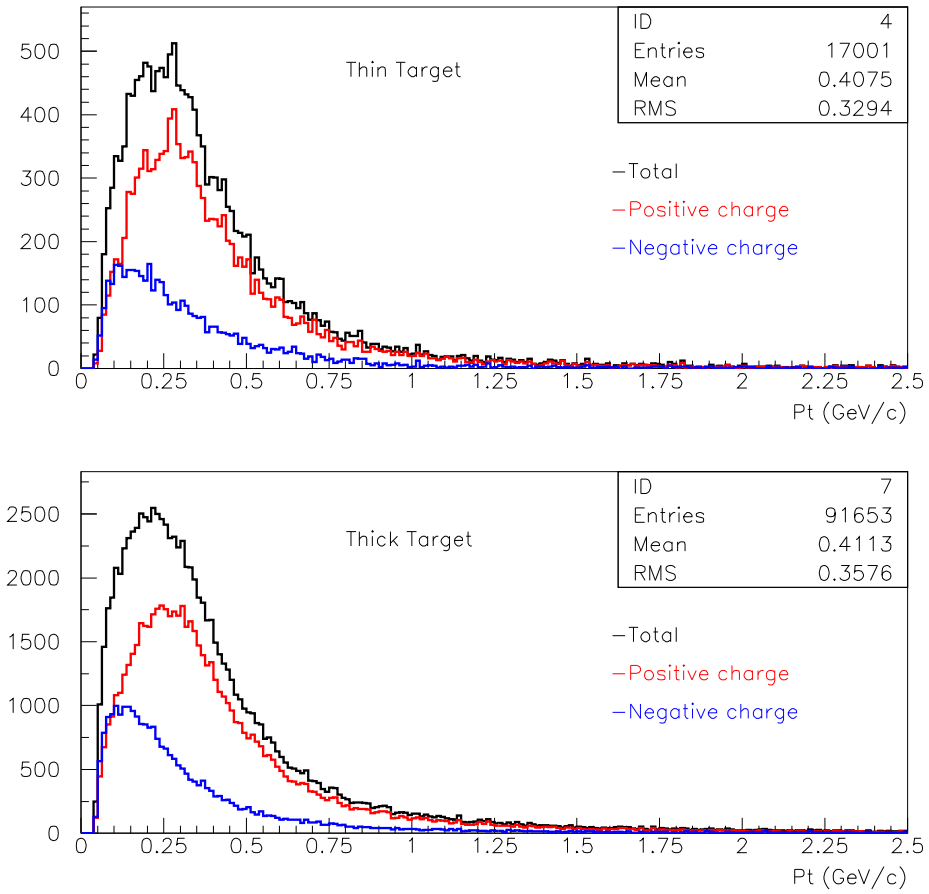

Figure 13.15: Transverse momentum distributions for the Al targets and beam momentum of 12.9 GeV/c.

kinematics bounds and both present a change with momentum of the fractions

of positive and negative particles. As in the previous cases, they suggest that low momentum particles stem mainly out of pair production. The positive to negative particles ratio, integrated over all momenta, is found to be 2.7 for the thin target and 2.5 for the thick one.

The transverse-longitudinal momentum correlation in figure 13.17 is confined by the

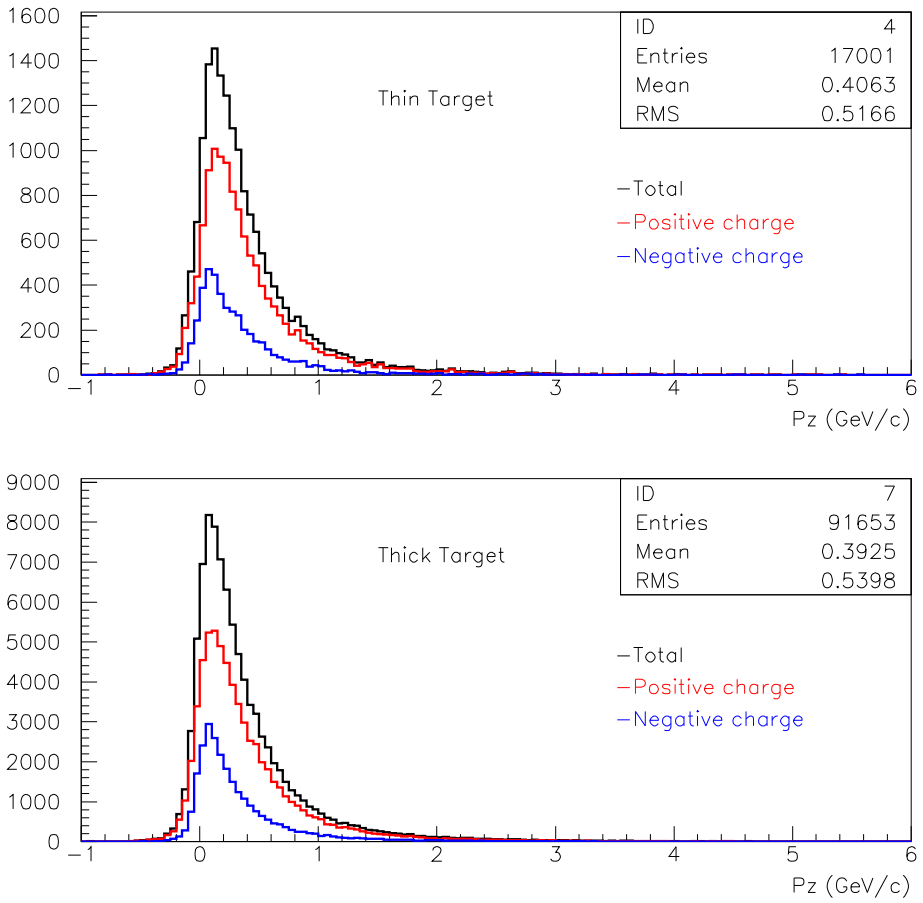

Figure 13.16: Longitudinal momentum distributions for the Al targets and beam momentum of 12.9 GeV/c.

curves dictated by the angular cuts: large values of p_t/p_z are only visible with the statistics of the thick run.

At first sight, there are no major problems in the 12.9 GeV/c run and there is an

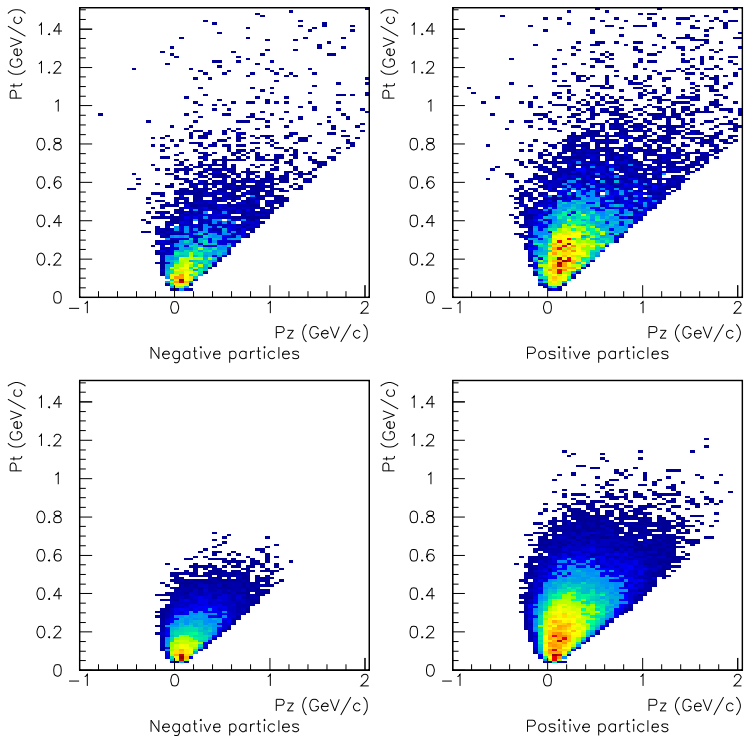

Figure 13.17: Transverse momentum as a function of the longitudinal momentum for thin (upper plots) and thick (lower plots) Al target and proton beam momentum of 12.9 GeV/c.

overall better quality of the data when compared to the tantalum case.

Unfortunately, no further and deeper investigation of these data is possible as long as all the needed software algorithms are implemented and the final calibrations of several relevant part of the detector are completed.

Merci!

Je tiens à remercier très particulièrement le Prof. Allan Clark qui m'a donné la possibilité de travailler à l'Université de Genève et de commencer mon travail de thèse dans une expérience qui représente un vrai défi pour le futur, comme ATLAS. Il a toujours été un énorme soutien pour moi et un guide efficace.

Je remercie le Prof. Alain Blondel, avec qui j'ai pu travailler dans la deuxième partie de ma thèse. Son enthousiasme pour la rechèrche a toujours représenté un exemple pour moi.

Je remercie le Dr. Jaap Panman et le Prof. Martin Pohl pour avoir accepté avec gentillesse de participer à mon Jury.

Merci à Didier qui a guidé avec patience mes premiers pas dans la salle blanche...

Merci à Catherine et à Peggy, qui, en souriant, m'ont constamment aidé avec mes problèmes "bourocratiques".

Merci à tous les collègues qui ont été gentils avec moi et qui m'ont soutenue avec leur chaleur.

Merci à Gersande pour la belle amitié commencée à Londres, et pour avoir corrigé avec patience mon Français.

Merci à Federica, qui a partagé avec moi le bureau, mes joies et mes angoisses. Je me souviendrai de nos "pauses tisane", et pas seulement...

Merci à Christine, pour son amitié profonde, pour ses conseils et pour son encouragement quotidien...

Merci à Salvatore, qui a toujours répondu avec patience à toutes mes questions, posées

à n'importe quel moment...

Merci à Roberto pour sa présence constante, même depuis Rome, et pour son soutien sans faille et son encouragement. C'est grâce à lui que j'ai pu surmonter les moments difficiles des derniers temps.

Merci à mes parents, pour leur amour.

Bibliography

[1] ATLAS Collaboration *ATLAS Technical Proposal* **CERN/LHCC/94-43** (1994)

[2] ATLAS Inner Detector Collaboration *ATLAS Inner Detector Technical Design Report* **ATLAS TDR 4, CERN LHCC 97-16** (1997)

[3] K.G. McKay *Phys.Rev.* **84** (1951) 829.

[4] J. Kemmer *Nuc. Inst. Meth.* **169** (1980) 499.

[5] S.M. Sze *Physics of Semiconductor Devices.* 2^{nd}edition J.Wiley and Sons (1981).

[6] J. Millman *Circuiti e sistemi microelettronici.* Boringhieri (1985).

[7] W.R. Leo *Techniques for Nuclear and Particle Physics Experiments* Springer-Verlag (1987).

[8] C. Posch *Analog readout fot the ATLAS Semiconductor Tracker* (1998).

[9] J. Kemmer *Nuc. Inst. Meth.* **226** (1984) 89.

[10] S. Roe, P. Weilhammer *ATLAS internal note* **ATLAS-INDET 41** (1994).

[11] A. Bar-Lev *Semiconductors and electronic devices* 2^{nd}edition Prentice Hall International (1984).

[12] G. Lutz *Semiconductors Radiation Detectors* Springer (1999).

[13] L. Evensen et al. *Nuc. Inst. Meth.* **A 337** (1993) 44.

[14] G.A. Beck et al. *Nuc. Inst. Meth.* **A 396** (1997) 214.

[15] C.J.S. Damerell, *Vertex Detectors* **RAL 86-77** (1986).

[16] E. Gatti and P.F. Manfredi *La rivista del nuovo cimento* **Vol.9, Serie 3, n^{o}1** (1986).

[17] V. Radeka *Ann. Rev. Nucl. Part. Sci.* **38** (1988) 217.

[18] R. Hofmann et al. *Nuc. Inst. Meth.* **225** (1984) 601.

[19] E. Nygard et al. *Nuc. Inst. Meth.* **A301** (1991) 506.

[20] E. Borchi and M. Bruzzi *La rivista del nuovo cimento* **Vol.17, Serie 3,n^{o}11** (1994).

[21] J. Koutsky and J. Kocik*Radiation damage of structural materials* Elsevier (1994).

[22] J.W. Corbett et al.*Phys. Rev. A* **138** (1965) 555.

[23] T.P. Ma et al. *Ionizing Radiation effects in MOS Devices and Circuits* J.Wiley and Sons (1989).

[24] T. Shulman **HU-SEFT 1991-07** (1991).

[25] E. Barberis et al. *Nuc. Inst. Meth.* **A326** (1993) 373.

[26] F. Lemeilleur et al. *Nuc. Inst. Meth.* **A360** (1995) 438.

[27] The ROSE collaboration *RD 48 Status Report* **CERN/LHCC 39** (1997).

[28] D. Pitzl et al. *Nuc. Inst. Meth.* **A311** (1992) 98.

[29] H.J. Ziock et al. *IEEE Trans. Nucl. Sci.* **40** (1993) 344.

[30] H.J. Ziock et al. *Nuc. Inst. Meth.* **A342** (1994) 96.

[31] SCT Detector Collaboration *ATLAS internal note* **SCT/Detector FDR** (1999).

[32] A. Peisert *Delphi internal note* **92-143 MVX 2** (1992).

[33] P. Horowitz and W. Hill *The Art of Electronics* Cambridge University Press (1989)

[34] G. Lindstrom *SITP internal note* **SITP-002** (1991).

[35] V. Cindro et al. *Nuc. Inst. Meth.* **A439** (2000) 337.

[36] E. Belau et al. *Nuc. Inst. Meth.* **214** (1983).

[37] E. Chesi et al.*IEEE Trans. Nucl. Sci.* **47** (2000) 1434.

[38] J. Kaplon et al.*Fifth Workshop on Electronics for LHC Experiments, Snowmass September 20-24,1999* **CERN/LHCC/99-33** (1999).

[39] ATLAS Inner Detector Collaboration *Extract from contractual documents* **ATLAS SCT/Detector PRR/00-1** (2000)

[40] Z. Li and H.W. Kraner *IEEE Trans. Nucl. Sci.* **38** (1991) 244.

[41] D. Ferrere and M.C. Morone *Measurements of CSEM detectors for qualification in the ATLAS experiment* **ATLAS SCT/Detector Note** (1999)

[42] ATLAS Inner Detector Collaboration *ATLAS Detector measurements* **ATLAS SCT/Detector FDR/99-8** (1999)

[43] The HARP Collaboration *Proposal to study hadron production for the ν factory and for the atmosferic ν flux* **CERN-SPSC/99-35** (1999)

[44] J. Collot et al. *Nuc. Inst. Meth.* **A 451** (2000) 327.

[45] T. Abbott et al. *Phys. Rev.* **D 45** (1992) 3906.

[46] N. Cabibbo *Phys. Rev. Lett.* **10** (1963) 531.

[47] M. Kobayashi and T. Maskawa *Prog. Theor. Phys.* **49** (1973) 652.

[48] B. Kayser *Phys. Rev.* **D66** (2002) 392.

[49] V.M. Lobashev et al. *Phys. Lett.* **B460** (1999) 227.

[50] S. Pascoli et al. **hep-ph/0212113 v2** (2002).

[51] The SNO Collaboration **nucl-ex0204009** (2002).

[52] The KamLAND Collaboration **hep-ex/0212021 v1** (2002).

[53] M. Apollonio et al. *Phys. Lett.* **B466** (2002) 415.

[54] F. Boehm et al. *Phys. Rev.* **D64** (2001) 112001.

[55] G.L. Fogli et al. *Phys. Rev.* **D66** (2002) 010001-406.

[56] E. Kearns *Proc of the 30th Int. Conf. on HEP* (2001) 172.

[57] T. Kajita *Talk at 18th Int. Workshop on Weak Interactions and Neutrinos* (2002).

[58] K. Nishikawa *Talk at XXth Int. Conf. on Neutrino Physics and Astrophysics* (2002).

[59] The LEP Collaborations **hep-ex/0212036** (2002)

[60] The LSND Collaboration *Phys. Rev.* **D 64** (2001) 112007.

[61] M. Apollonio et al. *Oscillation physics with a neutrino factory* **CERN-TH/2002-208** (2002).

[62] The HARP Collaboration *Status Report of the HARP experiment* **CERN-SPSC/2002-13** (2002).

[63] The NOMAD Collaboration *Nuc. Inst. Meth.* **A404** (2002) 96.

[64] J. Dumarchez *Talk at the HARP General Meeting 10/6/02* (2002).

[65] The CHORUS Collaboration *Nuc. Inst. Meth.* **A349** (1994) 70.

[66] The CHORUS Collaboration *Nuc. Inst. Meth.* **A378** (1996) 221.

[67] C. Valli *Tesi di laurea* (2001).

[68] The HARP Collaboration *Status Report of the HARP experiment* **CERN-SPSC/2001-031** (2001).

[69] F. Bobisut et al. *HARP Note* **02-007** (2002).

[70] F. Bonesini et al. *HARP Note* **02-004** (2002).

[71] C. Booth *HARP Note* **02-006** (2002).

[72] A. Grossheim *Private Communication* (2002).

[73] The HARP Collaboration *Status Report of the HARP experiment* **CERN-SPSC/2002-19** (2002).

[74] The ALICE DAQ Group *ALICE Note* **ALICE99/46** (1999).

[75] W. Blum and L. Rolandi *Particle detection with Drift Chambers* **Springer** (1994).

[76] C. Grupen *Particles detectors* (1996).

[77] E. Gatti et al. *Nuc. Inst. Meth.* **163** (1979) 83.

[78] R. Veenhof *http://r.home.cern.ch/r/rjd/www/HARP/gas.html#fitnmp* (2000).

[79] F. Dydak and G. Vidal-Sitjes *HARP Note* (2002).

[80] S. Borghi *Talk at the HARP General Meeting 10/06/02* (2002).

[81] G. Prior *Talk at the HARP General Meeting 10/12/01* (2001).

[82] A. Lundborg *Master thesis* (2002).

[83] S. Borghi, R. Veenhof *Talk at the HARP General Meeting 18/03/02* (2002).

[84] S. Robbins *Talk at the HARP General Meeting 18/03/02* (2002)

[85] Gaudi developers *http://lhcb-comp.web.cern.ch/lhcb-comp/Frameworks/Gaudi/*

[86] M. Poppe *ALEPH Note* **87-102** (1987).

[87] N.I. Chernov and G.A. Ososkov *Computer Phys. Comm.* **33** (1985) 329.

[88] A. Blondel *http://proj-bdl-nice.web.cern.ch/proj-bdl-nice/HARP/conventions.ppt* (2002).

[89] The K2K Collaboration *Phys. Lett.* **B511** (2001).